Post-processing of Antiresonant Hollow-core Fibers and its Applications

Daiqi Xiong

School of Electrical & Electronic Engineering

A thesis submitted to the Nanyang Technological University
in partial fulfillment of the requirements for the degree of
Doctor of Philosophy

2022

Statement of Originality

I hereby certify that the work embodied in this thesis is the result of original research, is free of plagiarised materials, and has not been submitted for a higher degree to any other University or Institution.

17th July 2022

Date

Daiqi Xiong

Supervisor Declaration Statement

I have reviewed the content and presentation style of this thesis and declare it is free of plagiarism and of sufficient grammatical clarity to be examined. To the best of my knowledge, the research and writing are those of the candidate except as acknowledged in the Author Attribution Statement. I confirm that the investigations were conducted in accord with the ethics policies and integrity standards of Nanyang Technological University and that the research data are presented honestly and without prejudice.

26 July 2022
. . . .
Date

. . . .
Asst. Prof. Wonkeun Chang

Authorship Attribution Statement

This thesis contains materials from 2 papers published in the peer-reviewed journals and 2 papers in conferences in which I am listed as the first author.

Chapter 3 contains results published in:

Daiqi Xiong, Xu Wu, Muhammad Rosdi Abu Hassan, Trivikramarao Gavara, and Wonkeun Chang, ”In-line hollow-core fiber-optic bandpass filter,” Opt. Lett. 46, 5918-5921 (2021)

Daiqi Xiong, Xu Wu, Muhammad Rosdi Abu Hassan, and Wonkeun Chang, ”An Antiresonant Hollow-Core Fiber In-Line Bandpass Optical Filter,” 2021 IEEE Photonics Conference (IPC), 2021, pp. 1-2,

The contributions of the co-authors are as follows:

- I proposed the idea, performed the experiments, and prepared the manuscript.
- Ms. Xu Wu and Dr. Trivikramarao Gavara participated in the characterization experiments.
- Dr. Muhammad Rosdi Abu Hassanassisted fabricated the antiresonant hollow-core fiber utilized in the paper.
- Prof. Chang provided the experimental apparatus, discussed the results and revised the manuscript.

Chapter 4 contains results published in:

Daiqi Xiong, Jiaqi Luo, Muhammad Rosdi Abu Hassan, Xu Wu, and Wonkeun Chang, ”Low-energy-threshold deep-ultraviolet generation in a small-mode-area hollow-core fiber,” Photon. Res. 9, 590-595 (2021)

Daiqi Xiong, Jiaqi Luo, Muhammad Rosdi Abu Hassan, and Wonkeun Chang, ”Low-Energy-Threshold Deep-Ultraviolet Generation in a Gas-Filled Single-Ring Hollow-Core Fiber,” Nonlinear Photonics, Optical Society of America, 2020, paper NpM2D.1.

The contributions of the co-authors are as follows:

- I performed the simulation and experiments, and prepared the manuscript.
- Dr. Jiaqi Luo participated in the experiment, and discussion of the simulation and experimental results.

- Dr. Muhammad Rosdi Abu Hassanassisted fabricated the antiresonant hollow-core fiber utilized in the paper.
- Prof. Chang provided the initial direction, experimental apparatus, discussed the results and revised the manuscript.

17th July 2022

. . . .

Date

. . . .

Daiqi Xiong

Acknowledgements

First and foremost, I would like to thank my supervisor, Prof. Wonkeun Chang, for his continuous support and guidance during my research. When I was a new student in this hollow-core fiber field, he has always been able to impart theoretical knowledge to me in simple ways. Then when I came into this field and started doing research work, he has always provided solutions to the problems I encountered. It was always a pleasure to have conversations with him, and I learned not only scientific knowledge but also soft skills in working life from him. I also want to thank him for his kindness in guiding me how to present my research, for supporting me to attend conferences. This work would never be possible without his knowledge, support and encouragement.

I also would like to acknowledge Dr. Jiaqi Luo and her support and guidance when I was new to an optics lab. Her knowledge and enthusiasm in implementing experiments often inspire me especially when my experiment is in trouble. I am also deeply indebted to Dr. Trivikramarao Gavara, Dr. Muhammad Rosdi Abu Hassan, and all my lab fellow students at the LUCI lab. Discussions among us always gave me a new understanding of knowledge.

Finally, my sincere thanks to my family, for helping and supporting me in every posssible way, and especially to Zhenyu, my partner, for making every day in Singapore enjoyable, even in the harsh environment of COVID. I would like to thank him for coming home with me when I finished my experiment in the early morning, for comforting me when my experiment was not going well, and for being the first listener and reader of my presentation and paper.

Abstract

Hollow-core fiber (HCF) is one of the most important inventions in the field of fiber optics over the past few decades. One side, as a bendable hollow optical fiber, the propagation property of light in HCF is similar to that in free space, which breaks the absorption limit of solid medium and creates an ideal waveguide with tunable dispersion and nonlinearity, low latency. On the other hand, as a platform for the interaction between light and matter, the laser pulses can be guided over long distance within the hollow fiber core of micrometer magnitude, breaking the limitation of diffraction limit in free-space transmission and greatly enhancing the interaction between light and matter. As an optical platform with dual advantages of fiber optics and free-space optics, HCF can play its unique advantages in optical applications.

This work is based on a particular type of HCF - antiresonant hollow-core fiber (AR-HCF). It offers a broadband guidance, low confinement loss, high damage threshold, and a tunable dispersion landscape by filling different gas species and pressure. The post-processing methods, tapering and wet-etching of AR-HCF, further facilitate the convenient tailoring of optical parameters.

Firstly, a new method of fiber-based in-line bandpass filter is realized is demonstrated by tapering a piece of AR-HCF to half of its original size. This exploits the periodical loss property of the AR-HCF - shorter wavelength is suppressed by the continuously varying tube-wall thickness of the tapered AR-HCF while the long cutoff wavelength is induced by its high confinement loss in a limited core size. The proposed bandpass filter can preserve all the benefits of the HCF and integrate into a fiber system seamlessly.

Following is the waist part of the tapered AR-HCF as a small-mode-area HCF (SMA-HCF). By tightly focusing the light into a small core with a diameter of only 10 μm, the highly nonlinear region in the gas medium is accessible. This allows us to explore gas-based ultrafast nonlinear optics with much lower single-pulse energy required by traditional methods. The onset of the deep UV in the gas-filled SMA-HCF with only hundred-nanojoule-level pump is realized.

At last, the UV generation in gas-filled AR-HCF is enhanced through theoretical and experimental studies of two factors - reducing the resonant bands and increase the self-steepening effect. The wet-etching technique achieves 250 nm reduction of the core-wall thickness of the AR-HCF which enhances the conversion efficiency from 2% to 6%. Besides, compressing the pump pulses and/or pumping with longer wavelength can increase the self-steepening effect to further enhance the bluish spectral broadening, resulting an enhanced UV generation.

Contents

List of Figures

Symbols and Acronyms

Acronyms

HCF	Hollow-Core Fiber
AR-HCF	Antiresonant Hollow-Core Fiber
PBG	Photonic Bandgap Guidance
HC-PBGF	Hollow-Core Photonic Bandgap Fiber
NC-HCF	Negative Curvature Hollow-Core Fiber
SR-HCF	Single Ring Hollow-Core Fiber
SEM	Scanning Electronic Micrograph
NLSE	Nonlinear Schrödinger Equation
GNLSE	Generalized Nonlinear Schrödinger Equation
GVD	Group-Velocity Dispersion
SPM	Self-Phase Modulation
TOD	Third-Order Dispersion
FWHM	Full-Width at Half-Maximum
SMA-HCF	Small-Mode-Area Hollow-Core Fiber
FROG	Frequency-Resolved Optical Gating
HHG	High Harmonic Generation

Chapter 1

Introduction

1.1 Hollow-Core Fibers

The pioneering work [9] reported in 1966 by Charles K. Kao and George A. Hockham ushered in an era of optical fiber. The fiber technology has great success in optical telecommunication [10, 11], fiber sensing [12, 13], and industrial applications [14], and has changed the way of people's life. In developments over the past few decades, solid-core silica fiber has been dominant because its high purity material with low cost allows extremely low loss [15]. However, it also has its limitations, such as high nonlinearity which limits the telecommunication capacity, its low damage threshold which limits the power handling capability of fiber laser, and the restriction of ultraviolet (UV) and mid-infrared (MIR) transmission. Nevertheless, these limitations can be filled in by a new kind of fiber, hollow-core fiber (HCF), which was proposed and implemented experimentally in 1990s [1, 16].

Hollow-core fiber has a groundbreaking light guiding mechanism to confine the light in its hollow core. Transmitting the light in the air achieves the MIR [4, 5, 17] and UV [18, 19] guidance. Besides, very little overlap with cladding glass when light is guided in hollow core enables the high-power beam delivery [20, 21]. Moreover, it triggers the low-latency optical communication [22, 23]. The hollow region inside the fiber also gives us the unique opportunity to discover the light-matter interactions, which is introduced in next section.

Based on the light-guiding mechanism, the hollow-core fiber can be classified into three categories, capillaries, hollow-core photonics bandgap fiber (HC-PBG) and antiresonant hollow-core fiber (AR-HCF). From 2000s to 2010s, the light guidancce bandwidth of HC-PBG was expanded from nanometers [24] to more than 100 nanometers [25], whereas the loss was still maintained at several dB/km. With the invention of Kagome structure [2], the loss of hollow-core fiber is reduced year by year, and many novel structures are erupted. Among which, the simplified structure, nodeless single-ring antiresonant HCF [26, 27], laid the design idea of ultra-low loss fiber. By far the lowest confinement loss is achieved in the double nested antiresonant nodeless fiber [7], 0.174 dB/km in C band.

1.2 Gas-Filled Hollow-Core Fiber System

Nonlinear optical phenomena grow vigorously with optical intensity and interaction length. In free-space optics, the intense light can be focused into a solid, gaseous or liquid medium, whereas the nonlinear interaction only happens just over few micrometers, as shown in Fig. 1.1 (a). By adopting solid-core fibers, the light in fundamental mode can be guided over few meters even kilometers, but the power of it is restricted by low damage threshold of solid-core fiber. Yet, the bandwidth is also limited by absorption of solid dielectric materials. On this basis, utilizing antiresonant hollow-core fiber gives us the unique opportunity to combine the advantages of both free-space and fiber-optics technology, e.g., high-power handling capability, broader transmission bandwidth and light-matter interactions over long interaction length, as shown in Fig. 1.1 (b).

Femtosecond lasers has flourished in recent decades, making it a good match for hollow-core fiber optics. Pumping with femtosecond pulses into the gas-filled hollow-core fiber promises us an excellent platform for staging light-matter interactions, and embracing the photonionization nonlinearity [28–30]. Generally speaking, the nonlinearity of gases is several orders of magnitude lower than that of silica, which can be perfectly compensated by sufficient interaction length, accumulating a weak nonlinear whisper to a significant response. More than that, filling gaseous medium into the hollow-core fiber offering us a precise control of its dispersion landscape, enabling the observations of different nonlinear phenomena.

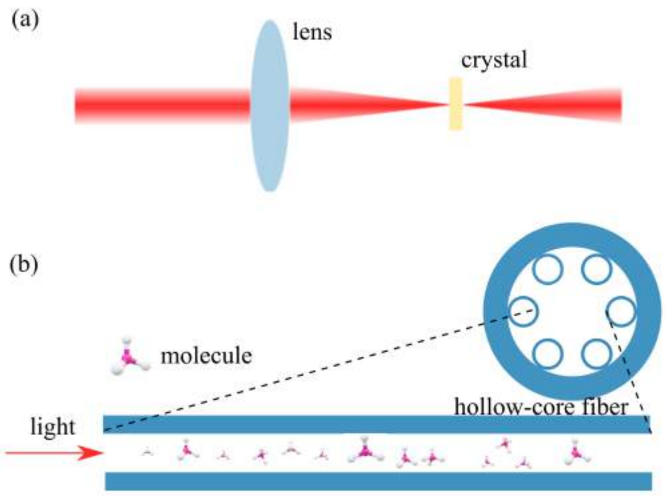

FIGURE 1.1: (a) Schematic diagram of focusing light into a crystal in the free-space optics. (b) Schematic diagram of interaction between light and filling molecular in the hollow-core fiber over long distance.

Filling with H_2 [31–33] causes Raman frequency conversion to occur, while filling with noble gases, we can investigate only the third-order Kerr nonlinearity, UV generation [34–36], supercontinuum generation [37–39], third harmonics generation [32] and so on.

In the nonlinear phenomena described above, the UV emission in the gas-filled hollow-core fiber by phase-matched frequency conversion process has incomparable advantages over other methods. The main issue of the available solid materials is they are highly susceptible to permanent photo-induced damage in UV. High-harmonic generation (HHG) is also widely used in generating UV [40]. However it requires very intense energy focused into a gas, which can be mitigated by sufficient interaction length within hollow-core fibers. In addition, the wavelength of UV generated by HHG is fixed while it can be easily tuned in gas-filled hollow-core fiber system by adjusting the gas species and pressure.

1.3 Thesis Overview

This thesis is concerned with the study of post-processing of antiresonant hollow-core fibers, tapering and wet-etching, to facilitate the convenient tailoring of optical parameters. These post-processing methods allow us better utilize its linear periodical loss characteristic to achieve bandpass filtering effect, lowering the pump requirement for nonlinear UV generation, and enhancing its performance of frequency conversion into UV. The thesis is organized in the following way.

Chapter 2 provides the background introduction for hollow-core fibers and nonlinear pulse propagation in the gas-filled hollow-core fiber system. The first part of Chapter 2 summarized the different kinds of hollow-core fiber based on their light guidance mechanism. Specifically, the low-loss antiresonant hollow-core fiber is introduced. The second part discusses the governing equations of nonlinear pulse propagation, the key aspects of linear and nonlinear response in the soliton dynamics and the onset of UV emission through dispersive wave generation in gas-filled HCF.

Chapter 3 introduces the post processing technique of tapering to allow us utilize its linear loss characteristic to achieve an in-fiber bandpass filter. With tapering, the fiber size can be precisely controlled along the length while its microstructure is well maintained. Following a proposed application about mid-infrared femtosecond pulse source, the in-fiber bandpass filter can be seamless integrated into a gas-filled HCF system to filter out all the undesired spectral components after its onset of mid-infrared pulses through frequency conversion.

Chapter 4 focuses on the nonlinear performance in the tapered antiresonant HCF. A small-mode-area hollow-core fiber can be fabricated by the tapering method, which is difficult to be achieved by the direct stack-and-draw method. As the fiber core size decreases, the energy of overall soliton dynamics can be scaled down, which can substantially decrease the pump energy requirement for UV pulse emission down to hundred-nanojoules level. However, the conversion efficiency from pump to UV pulse is not that desirable, which is left to be dealt with in the next chapter.

Chapter 5 is devoted to enhance the UV generation performance in the gas-filled hollow-core fiber system, including the generated UV quality and conversion efficiency. The first part investigates the influence of self-steepening effect on the UV generation. We first figure out the self-steepening effect can have either positive or negative effect based on normalized nonlinear Schrödinger equation. To achieve the optimal self-steepening effect in enhancing UV emission in the practical gas-filled HCF experiment, the compressed pump pulse is required. The second part presents the influence of the resonance bands on UV generation in the antiresonant HCF. Th experimental results of UV generation in the vicinity of resonance bands shows us the how the band-edge induced dispersive wave (DW) beats with other DWs and drags the energy away from pump to the desirable dispersive wave. Following a numerically comparison with the system without the resonance bands, both the UV conversion efficiency and quality can be improved. To remove the resonance bands, the post-processing, wet-etching method, is implemented. The experimental result of UV generation in the gas-filled etched AR-HCF shows a significant improve in the UV conversion efficiency.

Chapter 6 draws the conclusions and proposes the future research directions from this thesis.

Chapter 2

Nonlinear Pulse Propagation in Gas-Filled Hollow-Core Fiber

The greatest merit of a fiber is it can trap light inside the core and keep its mode-field area steady over meters even kilometers. Once the light is captured and guided, it can continuously interact with dielectric material over its long propagation length, where a faint perturbation can be accumulated to a dramatic response. In the 21st century, as the information transmission capacity continues to explode, and the power and pulsewidth of ultrafast lasers approach the limit on and on, the intrinsic defects of solid-core fiber (limited nonlinearity and dispersion, low optical damage threshold, UV and IR light blocking, etc.) are increasingly obvious. To break through the intrinsic bottleneck of solid fibers, the pioneers in the field of hollow fiber started to explore and study the new optical guiding mechanism - establishing a light guiding path in the hollow fiber core can perfectly solve the intrinsic material defects encountered in solid-core fiber technology. At the same time, combining HCFs with ultrafast lasers that are in their prime gives us the unique opportunity to observe the fascinating light-matter interactions. Hence, a brief description on the HCFs will be first given, followed by the linear and nonlinear response when ultrafast pulse propagates in a dielectric waveguide.

2.1 Introduction to Hollow-Core Fibers

The first research of hollow-core waveguide operating at the optical frequencies can be traced back to 1960's [41], which is a theoretical paper studied the attenuation level of dielectric hollow-core tubes by Marcatili and Schmeltzer. After that, the hollow-core fiber technology has not been developed at a high speed until the first invention of hollow-core bandgap fiber in 1999 [1]. This creative practice of introducing micro-structure into fiber designs boosted subsequent inventions of novel HCFs. In this section, the classification of HCFs, especially the low-loss antiresonant hollow-core fibers will be reviewed.

2.1.1 Classification of Hollow-Core Fibers

Unlike the solid core fibers with solid core of higher refractive index than cladding guiding light in its solid core by total internal reflection, the hollow core fibers confines light in its hollow core of lower refractive index than cladding. That means the traditional guiding mechanism, total internal refraction is not working in hollow core fibers. According to the different guidance mechanisms that hollow-core fibers can work on, there are three main types of HCFs, the glass capillary, hollow-core photonic bandgap fiber (HC-PBGs), antiresonant hollow-core fiber (AR-HCF).

The silica capillary fiber has a simple structure with a central hollow region in the core, as shown in Fig. 2.1, which can provide a solution for the research on nonlinear phenomena required millijoule-level femtosecond-duration pulses. The light in glass capillaries guided by external reflection, while a fraction of it transmits through the core-cladding interface at every reflection, leading to the inescapable loss which is the inverse cube of the core diameter [41]. To mitigate the confinement loss dramatically, the use of capillaries with much larger core radii, greater than 100 μm is necessary. At the same time, the large core size brings the excellent high power handling ability and weak waveguide dispersion so that the gas dispersion dominates, the capillaries have been utilized in nonlinear Raman optics since 1970 [42, 43]. Recently, many of the available literature on nonlinear optics in capillary fibers deals with the question of how to increase waveguide dispersion and nonlinearity to obtain soliton effects, pumping in higher-order modes [44, 45], moving to longer pump wavelength [46–48], pre-compressing pump pulses [49, 50]. Such capillary fibers with large core-size have been used with great success in the energy up-scaling of pulse compression and UV generation through frequency conversion process.

As the glass capillary shows, hollow-core fibers are intrinsically lossy, but depending on the guiding mechanism the confinement losses can be made very small. One way to substantially decrease the confinement loss is to set up a 2D photonics bandgap structure in hollow-core fiber, namely, hollow-core photonic bandgap fiber (HC-PBGF). This idea was first proposed by Philip Russell in 1991 [16] and theoretically demonstrated by Birks in 1995 [51], following by the experimentally successful HC-PBGF by Cregan in 1999 [1]. The cladding of HC-PBGF consists of a periodic structure with an optical bandgap, as shown in Fig. 2.1. This periodic structure can trap the light at certain frequencies. The guidance mechanism of it is similar to the one-dimensional multi-layer Bragg reflection, which can reflect a range of frequencies around a certain frequency for a range of angles [52]. Whereas, the HC-PBGF is two dimensional, meaning no leakage in practice for sufficiently many layers of structure in any directions. The motivation of developing HC-PBGF is to avoid the Rayleigh scattering in UV range and phonon absorption in mid-IR range, since only small amount of material is overlapped with light during its propagation. However, the further investigation found that the ultra-low loss in HC-PBGF is limited by surface roughness from surface capillary waves [53]. In that paper, the lowest transmission attenuation of the HC-PBGFs, 1.2 dB/km at 1620 nm, is achieved and it implies that the loss can be as low as 0.13 dB/km at 1900 nm, which is less than the best conventional fibers [53]. The microstructure of air holes in the cladding of HC-PBGF has already gone beyond the scope of the traditional solid optical fiber technology, while it also brings advantages over it to overcome some technical obstacles in the applications of the conventional optical fiber - anomalous dispersion in the visible light frequency [55], highly birefringence [56], etc.

However, these HC-PBGFs have a limited transmission window (dozens of a hundred nanometers) as well as a deep-slope group velocity dispersion (GVD) shape, which limits the experiments based on extreme ultrafast laser pulses [57]. Those problems are overcome by a new type of HCF which is the third one we review here, antiresonant hollow-core fiber (AR-HCF). It shows broad guidance band and simple structure, gaining explosive development in last ten years. In 2002, F.

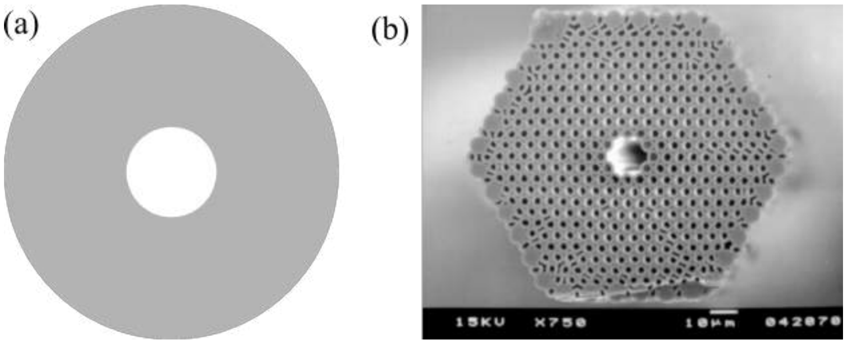

Figure 2.1: (a) Schematic diagram of glass capillary and (b) scanning electron micrograph (SEM) of HC-PBGF [1].

Benabid proposed a hollow-core fiber with a periodic hexagonal-lattice cladding, named Kagome fiber [2]. This Kagome fiber can guide light but no PBG found in neither simulation nor experiment, which means that behind this guidance lies a different light conduction mechanism from the PBG. In 2007, the antiresonant reflecting optical waveguide (ARROW) modal, which was proposed in 1986 [58], was utilized to explain the light guidance in Kagome fiber [59] - core modes at resonance frequencies will be coupled into cladding to be attenuated, while those at antiresonant wavelength can transmit stably in the fiber core. Since the explanation of light conduction mechanism comes from ARROW model, this kind of hollow core fiber was named HC-ARF (hollow-core antiresonant fiber), and HC-ARF officially entered the historical stage. On account of no PGB exists in Kagome fiber, it suffers higher loss than HC-PBGF, 1000 dB/km. Inspired by Kagome fiber, more and more antiresonant structures have been proposed and iterated in recent year as shown in Fig. 2.2, leading to comparable losses to HC-PBGFs. Its low loss, together with its broadband transmission, high optical damage threshold and unique dispersion landscape, make it suitable in the investigations of light-matter interactions [2, 38, 49, 60].

2.1.2 Low-Loss Antiresonant Hollow-Core Fibers

A major concern about AR-HCF when it was first demonstrated is its high loss. After that, the development of AR-HCF focuses on loss reduction. In 2011, Y. Wang et al. found that compared with positive curvature, the core structure with negative curvature, showing in Fig. 2.2 (b), could reduce the loss to 180 dB/km by increasing the core wall curvature [3], which boosted the appearance of negative

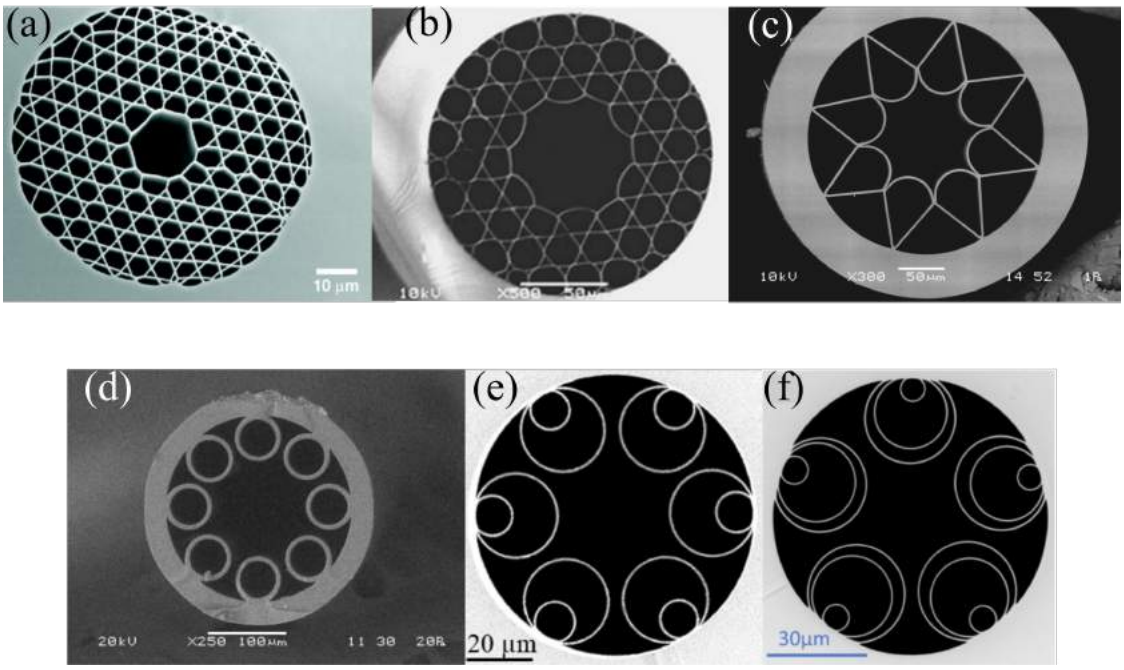

Figure 2.2: Selective scanning electron micrographs (SEMs) of some AR-HCFs: (a) Kagome fiber [2]; (b) Negative curvature Kagome fiber [3]; (c) Simplified negative curvature antiresonant hollow-core fiber [4]; (d) Nodeless single ring hollow-core fiber [5]; (e) Nested antiresonant nodeless hollow core fiber [6]. (f) Double nested antiresonant nodeless hollow core fiber [7].

curvature hollow-core fibers (NC-HCF). In 2012, F. Yu et al. indicated that complicated multi-layer cladding structure is not necessary in AR-HCF and further simplified the Kagome structure to a single-layer negative curvature structure with the loss as low as 34 dB/km [4], as shown in Fig. 2.2 (c). Then, it was reported by A. Kolyadin et al. in 2013 that the contact node between cladding tubes is the main reason for the increasing loss in AR-HCF, and thus proposed the nodeless single layer AR-HCF [5]. It is exhibited in Fig. 2.2 (d). So far, AR-HCF gradually simplified from Kagome structure to the simplest one - single layer tubular-type, which is the one used in this doctoral thesis, also referring to single ring hollow-core fiber (SR-HCF). The demonstration of the transmission loss as low as 0.28 dB/km in a AR-HCF that utilized the nested antiresonant nodeless structure (Fig. 2.2 (d)), which was first proposed by F. Poletti in 2014 [6], is a milestone achievement revealing its huge potential in practical applications [61]. This number has been further decreased down to 0.174 dB/km in telecommunication C band [7] by utilizing a double nested structure, as shown in Fig. 2.2 (f).

The light of certain wavelengths is confined in the hollow core due to inhibition of coupling between the optical modes in the hollow core and those in the cladding

[27]. In this regard, the thickness of cladding-core wall, t, turns out to be one of the most influential geometrical parameters in dictating the transmission properties. This is because the dielectric modes in the cladding wall can interact strongly with the core modes leading to high loss at resonant wavelengths, λ_m, which is given by [62]:

$$\lambda_m = \frac{2t\sqrt{(n^2-1)}}{m} \tag{2.1}$$

where n is the refractive index of the dielectric material and $m = 1, 2, 3, \ldots$ is the resonance order denoting the number of half-wavelengths that fits in t. Between the resonances, i.e., under the antiresonant condition, a good confinement of light generally can be achieved. The leaking and trapping of light in the core at resonant and antiresonant conditions are illustrated in Fig. 2.3 (b). This leads to the antiresonant hollow-core fiber featuring a series of transmission bands that are separated by resonant bands, with the first t-induced resonant band appearing

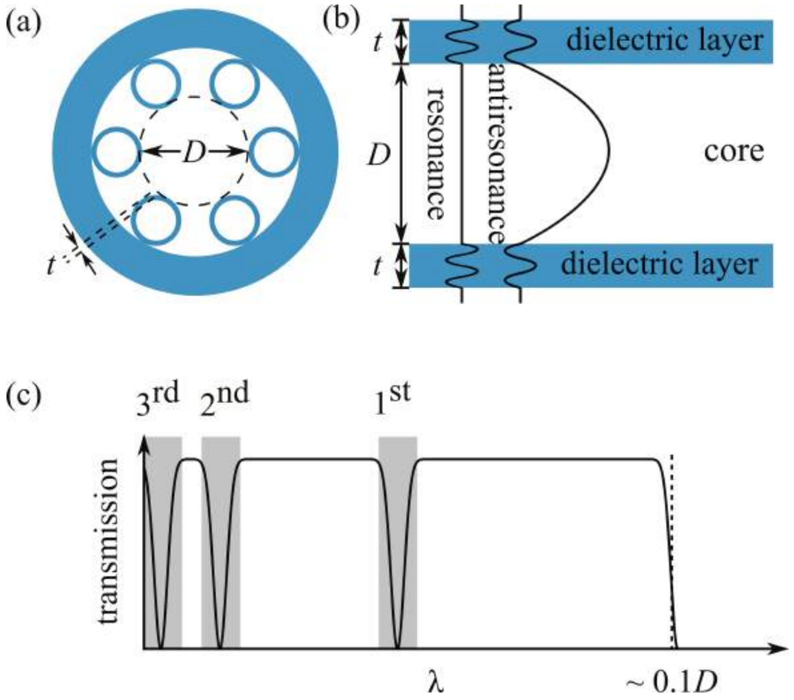

Figure 2.3: Adopted from [8]. (a) An idealized cross-section of a SR-HCF. D is the core diameter and t is the thickness of the dielectric layer. (b) Illustration of leaking and trapping of light in the core at resonant and antiresonant conditions determined through Eq. 2.1. (c) Schematic transmission spectrum of an AR-HCF. The gray shades are the t-induced resonant bands. In the long-wavelength limit, the fiber loses its guidance above $\lambda \approx 0.1D$.

at $2t\sqrt{n^2-1}$. This is shown schematically in Fig. 2.3 (c). The long-wavelength limit of the hollow-core fiber transmission is governed by one of the below two factors. First is the ratio between wavelength and core diameter, l/D. A recent numerical study reports that the loss of the fundamental core mode of a typical SR-HCF scales approximately as $\lambda^{4.5}/D^{5.5}$ and the mode is no-longer supported when $\lambda \gtrsim 0.1D$ [63] and the strength of the different resonant bands are illustrated in [64, 65].

2.2 Nonlinear Schrödinger Equation

The majority of nonlinear effects happen when the pulsewidth of involved laser pulses is about 10 ns ~ 10 fs. When such a laser pulse propagates in a fiber, dispersion and nonlinear phenomena will modify its pulse shape in time domain and frequency components in spectral domain. To describe this pulse evolution, nonlinear Schrödinger equation (NLSE), which is derived from the famous Maxwell's equations, is used. The NLSE containing two parts, dispersion $\widehat{D}$ and nonlinearity $\widehat{N}$, is written as below [66]:

$$i\frac{\partial A}{\partial z} = \overbrace{\underbrace{-\frac{i\alpha}{2}A}_{\text{loss}} + \underbrace{\frac{\beta_2}{2}\frac{\partial^2 A}{\partial T^2}}_{GVD}}^{\widehat{D}} - \overbrace{\underbrace{\gamma|A|^2 A}_{SPM}}^{\widehat{N}} \tag{2.2}$$

where A is the slowly varying envelope of pulse, z is the propagation variable along a well defined direction given by the fiber axis, T is the time frame ($T = t - \beta_1 z$) co-moving with the group-velocity of the pulse. $\widehat{D}$ represents the group-velocity dispersion β_2, and attenuation coefficient α in the medium, while $\widehat{N}$ is the nonlinear operator that governs the nonlinearity, self-phase modulating (SPM), where γ is the nonlinear parameter.

2.2.1 Group-Velocity Dispersion

Group-velocity dispersion (GVD) refers to that the light velocity depends on its frequency, indicating the dependence of refractive index $n(w)$ on frequency [67].

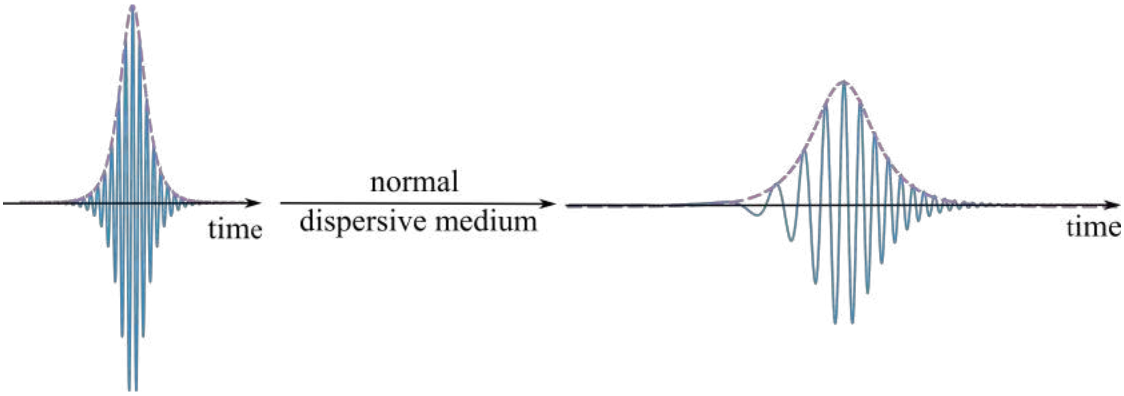

Figure 2.4: Schematic diagram of GVD-broadened pulse in a normal dispersive medium.

This linear GVD effect solely rearranges the sequence of frequency components in time domain but doesn't introduce new ones. In a mathematics sense, this effect is explained by expanding the propagation constant β into a Taylor series near the pulse central frequency w_0 [67]:

$$\beta(w) = n(w)\frac{w}{c} = \beta_0 + \beta_1(w - w_0) + \frac{1}{2}\beta_2(w - w_0)^2 + ... \tag{2.3}$$

where

$$\beta_m = \left(\frac{d^m\beta}{dw^m}\right)_{w=w_0}, \qquad m = 0, 1, 2, ... \tag{2.4}$$

In a physical sense, the pulse envelope is moving at group velocity $v_g = 1/\beta_1$ and the variable β_2 refers to the dispersion of group velocity, which causes the pulse broadening. Depending on the sign of β_2 is +1 or -1, the dispersion can be normal and anomalous. In a waveguide with normal dispersion, the higher frequencies travel slower than lower ones, otherwise the opposite. In time domain, not only the frequencies are rearranged, the pulse width would be broadened, together with the decreasing peak power, as shown in Fig. 2.4.

2.2.2 Self-Phase Modulation

Self-phase modulation (SPM) is the most basic nonlinear phenomenon, originating from the optical Kerr effect, which refers to that the refractive index not only depends on optical frequency, also on the local pulse intensity [68]. An optical pulse would experience phase shift under the SPM effect, leading to new instantaneous frequencies generation. We neglect the linear terms, both loss and dispersion, in Eq. 2.2, and rewrite it in time domain,

$$\frac{\partial A(z,T)}{\partial z} = i\gamma \left|A(z,T)\right|^2 A(z,T) \tag{2.5}$$

which can be directly performed the analytical integral and get the general solution as below:

$$A(z,T) = A(0,T)\ \exp(i\gamma \left|A(0,T)\right|^2 z) \tag{2.6}$$

Equation 2.6 clearly indicates that the nonlinear effect will change the pulse phase but not the pulse shape. From the phase shift $\phi(z,T) = \gamma|A(0,T)|^2 z$, we can get instantaneous frequency $w(T)$ as follows,

$$w(T) = w_0 + \delta w(T) = w_0 - \frac{\partial \phi}{\partial T} = w_0 - \gamma \frac{\partial}{\partial T} |A(0,T)|^2 z \tag{2.7}$$

where it introduces low (high) frequencies in the leading (trailing) edge, while the central and both ends parts of pulse remain in same frequency, as shown in Fig. 2.5. In this way, pulse would be broadened in spectral domain but keep unchanged in temporal domain.

2.2.3 Solitons in Nonlinear Schrödinger Equation

We already knew that the interplay between dispersion and nonlinear effects forms the pulse evolution in the fiber. Depending on the different combination of GVD and SPM, the pulse behaves differently. If pulse is propagating in normal dispersion regime, the pulse would be broadened rapidly, since the SPM would generate lower frequencies in the leading edge which are in higher velocity. The combined effect of these two causes the light pulse to broaden faster than GVD alone. Meanwhile, the peak power dies quickly and weakens the nonlinearity. On the other hand, under the anomalous dispersion regime, an optical soliton which can remain constant or change periodically in temporal and spectral domain can be formed [69]. To

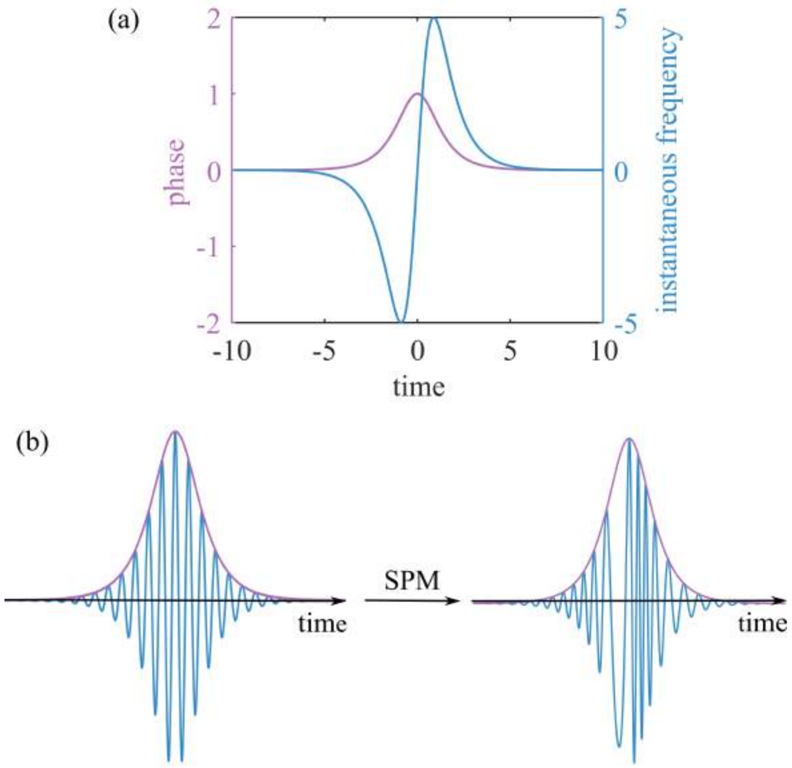

Figure 2.5: (a) Temporal phase $\phi(z,T)$ (left) and instantaneous frequency $\delta w(T)$ (right) for an optical pulse under SPM effect. (b) SPM causes the leading (trailing) edge of the pulse to redshift (blueshift), but the pulse shape remains unaffected.

determine which one plays the main role during the pulse evolution, two parameter, dispersion length L_D and nonlinear length L_{NL} are introduced as below:

$$L_D = \frac{{T_0}^2}{|\beta_2|},\ L_{NL} = \frac{1}{\gamma P_0} \tag{2.8}$$

where T_0 is $1/e^2$ pulse width and P_0 is the peak power of the input pulse. These two variables represent the length scales over which effect become more important when pulse is transmitting in the medium. The beating between these two effects can be governed by soliton order N, as below:

$$N^2 = \frac{L_D}{L_{NL}} \tag{2.9}$$

In the anomalous dispersion regime, GVD introduces negative chirp while SPM introduces positive one. When $N = 1$, these two effects reach a balance stage and

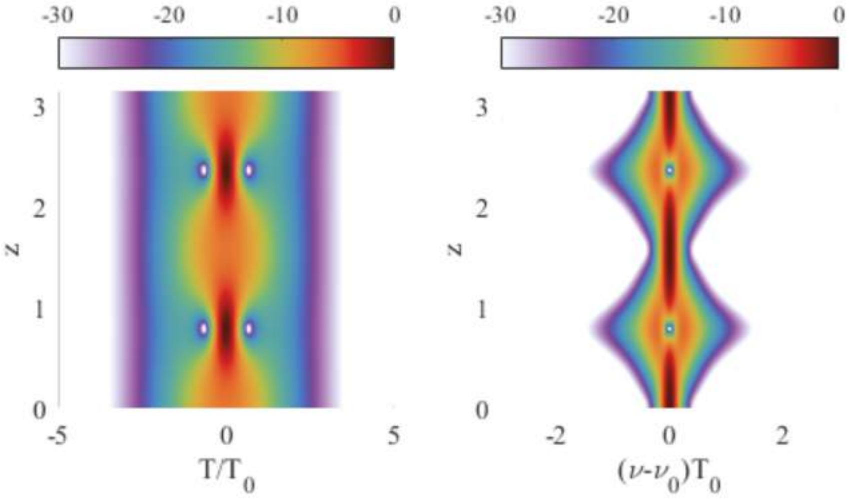

FIGURE 2.6: Periodically evolution in both temporal (left) and spectral (right) domains of a second-order soliton.

a fundamental soliton is supported, that do not change its shape during propagation. If $N > 1$, higher-order solitons are formed, where SPM dominates first, then anomalous GVD catches up and compensates the positive chirp introduced by SPM. Those higher-order solitons experience periodically evolution pattern in both temporal and spectrum domain. As shown in Fig. 2.6 (a), a second-order soliton experiences SPM-induced spectral broadening initially, introducing the high (low) frequencies at trailing (leading) edge. Meanwhile, anomalous dispersion compresses the pulse. Since the chirp is linear in central, only central part of pulse is compressed, along with two side bands left. Then, the pulse recovers to its injection state and repeats this process.

2.2.4 Higher-order Perturbations

The Eq. 2.2 can explain many nonlinear effects, but it still needs to be amendment if the peak power of pump pulse is higher than the threshold of stimulated Raman scattering or the pump pulsewidth is in femtosecond-scale. In these cases, a generalized nonlinear Schrödinger equation is used [67],

$$\frac{\partial A}{\partial z} = \overbrace{\underbrace{i\sum_{n=2} \frac{i^n\beta_n}{n!}\frac{\partial^n}{\partial T^n}A}_{\text{dispersion}} - \underbrace{\frac{\alpha}{2}A}_{\text{loss}}}^{\widehat{D}} + \overbrace{i\gamma\left(\underbrace{|A|^2A}_{\text{SPM}} + \underbrace{\frac{i}{w_0}\frac{\partial}{\partial T}(|A|^2A)}_{\text{self-steepening}} - \underbrace{T_RA\frac{\partial|A|^2}{\partial T}}_{\text{Raman response}}\right)}^{\widehat{N}} \tag{2.10}$$

where high-order dispersion β_n, the n^{th} order of dispersion, is conseidered in $\widehat{D}$. In nonlinear operator, self-steepening and Raman response are included, T_R originating from the delayed Raman response which is responsible for the Raman-induced frequency shift. Those higher-order dispersion and nonlinear effects can be considered as perturbations, which can cause soliton fission and introduce dramatic change in pulse evolution. To better understand how these perturbations would influence the soliton evolution according to GNLSE, we introduce the normalized GNLSE as below,

$$i\frac{\partial u}{\partial \xi} + \frac{1}{2}\frac{\partial^2 u}{\partial \tau^2} + |u|^2u = i\delta_3\frac{\partial^3 u}{\partial \tau^3} - is\frac{\partial}{\partial \tau}(|u|^2u) + \tau_R u\frac{\partial |u|^2}{\partial \tau} \tag{2.11}$$

where ξ and τ are two dimensionless variables

$$\xi = \frac{z}{L_D},\ \tau = \frac{T}{T_0} \tag{2.12}$$

and the normalized variables δ_3, s, τ_R represent TOD, self-steepening, stimulated Raman effect, are expressed as,

$$\delta_3 = \frac{\beta_3}{6|\beta_2|T_0},\ s = \frac{1}{\omega_0 T_0},\ \tau_R = \frac{T_R}{T_0}. \tag{2.13}$$

However, Raman is absent in the nonlinear interaction of monatomic gases with ultrafast laser pulses, giving the opportunity to study the nonlinear dynamics in the absence of Raman-induced nonlinear effect, e.g., soliton self-frequency shift. In this thesis, the Raman nonlinear contributions will be omitted since only noble gas, argon, has been used in both simulation and experiments.

2.2.4.1 Third-Order Dispersion

When pump pulse is near zero-dispersion wavelength (ZDW), or spectrum width is not narrow enough (T_0 <1 ps), the third-order dispersion (TOD) β_3 can have a dramatic effect. From Eq. 2.3, β_2 is a quadratic function with respect to $(\omega-\omega_0)$ while β_3 is a cubic one. That means adding TOD can make pulse become asymmetric. In the soliton evolution where $\beta_2<0$, the effect of TOD is more fascinating, leading to an additional radiation [70–75], so-called Cherenkov radiation, or dispersive wave (DW) [76].

To study the effect of TOD solely, we can simply make other non-related terms, s, τ_R, to be zero in Eq. 2.11 to get rid of self-steepening and Raman effect. The former would be discussed later while the latter is absent in the atomic environment. The simulated evolution in both temporal and spectral domain of a second-order soliton including TOD ($\delta_3 = 0.2$) according to Eq. 2.11 is shown in Fig. 2.7. Comparing with Fig. 2.6, it clearly indicates that with the TOD perturbation, the periodical evolution pattern of the higher-order soliton does not longer exist. After the second-order soliton gets compressed in temporal domain and broadened in spectral domain around $z = 1$, there is an additional radiation, dispersive wave, happening at higher frequency side. Since the dispersive wave is in the normal dispersion regime, it would get broadening in temporal domain quickly and loss its peak power. It leaves the fringes in trailing edge of pulse indicating its emission, which is from the interference between DW (dispersive wave) and main spectrum in spectral domain. Besides, the soliton fission is observed in temporal domain, traveling at different group velocity due to the frequency components are different. This DW generation can be explained by phase-matching process, as shown in Fig. 2.8. The phase of soliton and linear waves at different frequencies are as below,

$$\phi(\omega_s) = \beta(\omega_s)z - \omega_s\beta_1 z + \frac{1}{2}\gamma P_0 z \tag{2.14}$$

$$\phi(\omega) = \beta(\omega)z - \omega\beta_1 z \tag{2.15}$$

and the phase mismatch is the phase difference between these two. Figure 2.8 shows that when $\beta_3 = 0$, the phase mismatch never across zero. At the pump frequency, the difference between its phase mismatch value and zero is caused by the nonlinear

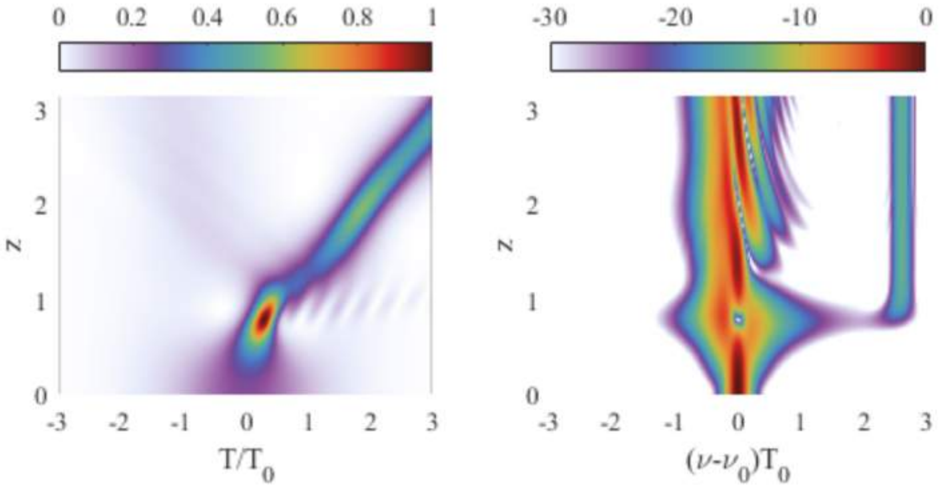

FIGURE 2.7: (a) The pulse evolution of a second-order soliton when $\delta_3 = 0.2$ in temporal (left) and spectral (right) domain.

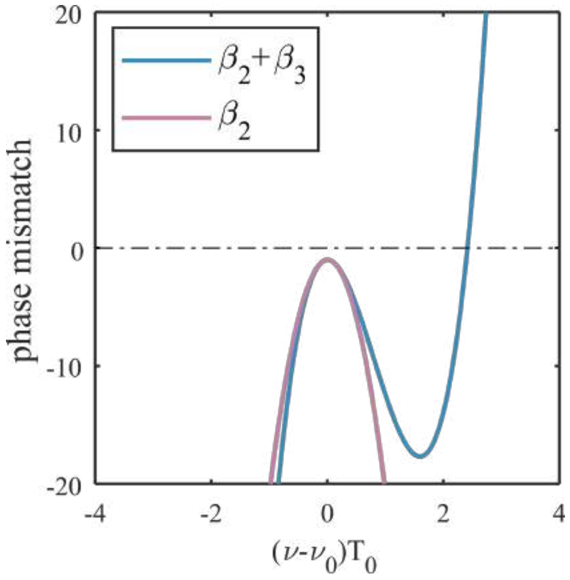

FIGURE 2.8: Phase mismatch $\Delta\phi = \phi(\omega_s) - \phi(\omega)$ at different frequencies in the case with and without third-order dispersion (TOD).

correction term $\frac{1}{2}\gamma P_0 z$ in Eq. 2.14. When β_3 is not neglected, $\delta_3 = 0.2$ in this case, the phase mismatch curve is distorted and created another phase matching point at higher frequency side. This matching of phase makes it is possible to transfer energy from pump to this matched frequency.

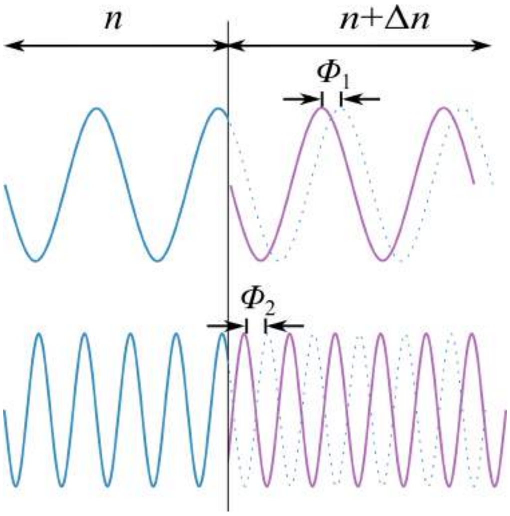

FIGURE 2.9: Schematic diagram shows that phase shift is dependent on frequency.

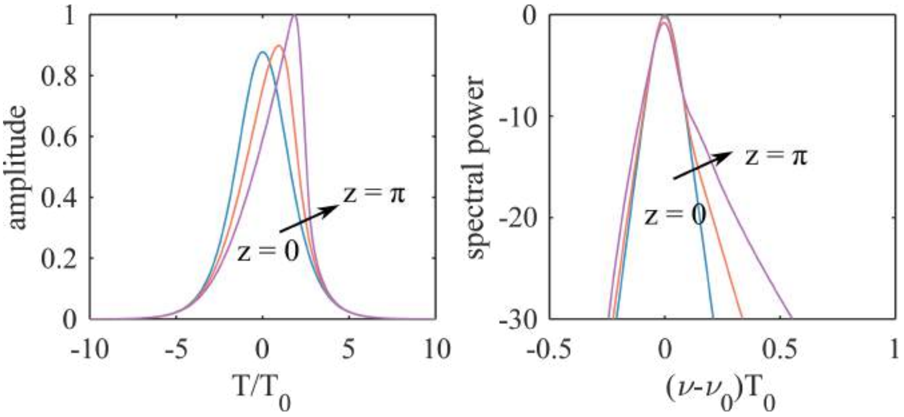

FIGURE 2.10: Temporal (left) and spectral (right) domain of a second-order soliton propagates under self-steepening effect according Eq. 2.11.

2.2.4.2 Self-Steepening

For ultrashort broadband pulses, a correction term to nonlinear operator needs to be included, which is the self-steepening term in Eq. 2.10. This self-steepening effect will alter both pulse shape and spectral components. As shown in Fig. 2.10, along the propagation, the self-steepening effect makes the trailing edge of the pulse steeper than before, which causes higher instantaneous frequency according to Eq. 2.7. This can be explained by the intensity dependent refractive index. The high intensity in the central pulse increases the refractive index, leading to a slower group velocity than both ends of the pulse [67]. It also can be explained by the frequency dependent phase shift, as shown in Fig 2.9. For a same amount of refractive index change, Δn, the phase shift is lower for lower frequency ($\Phi_1 < \Phi_2$). Recall Fig. 2.5

(b), the higher frequency part at the trailing edge of pulses experience an extra group delay [77].

2.3 Unidirectional Propagation Equation

In our research conditions, the phase of backward optical waves is too poor to build up any noticeable signal. That is to say, we can omit the backward waves, solving the unidirection field propagation equation, given by [78],

$$\begin{aligned}\frac{\partial \mathbf{E}(z,w)}{\partial z} &= i\left(\beta - \frac{w}{v} + i\frac{\alpha}{2}\right)\mathbf{E}(z,w) + \frac{w^2\mu_0}{2\beta}\mathcal{F}\left\{\epsilon_0\chi^{(3)}\mathbf{E}(z,t)^3\right\} \\ &- \frac{w\mu_0}{2\beta}\mathcal{F}\left\{\frac{\partial n(z,t)}{\partial t}\frac{I_p}{E(z,t)} + \frac{e^2}{m_e}\int_{-\inf}^{t} n(z,t')E(z,t')dt'\right\} \qquad (2.16)\end{aligned}$$

where $\mathbf{E}(z,w)$ is the optical field in the frequency domain with w denoting angular frequency, $\beta(w)$ is the full dispersion including both waveguide and filling gas contribution via a Sellmeier equation [79]. The term containing $\chi^{(3)}$ is responsible for the third-order nonlinearity of the pressurized gas [80]. The last term in this equation represents the photonionization effect, where I_p is the first ionization energy, e and m_e are the election charge and electron mass respectively. $n(z,t)$ is the local free-electron density, calculated by a modal developed by Ammosov, Delone, and Krainov, so called ADK modal [81]. Numerically simulating the nonlinear pulse propagation in gas-filled HCFs by solving this carrier-resolved field propagation equation has shown great success in many cases. The rest of this thesis makes extensive use of this numerical model results to clarify and support the experimental phenomena. The underlying code was written by Wonkeun Chang.

Chapter 3

A Linear Antiresonant Hollow-Core In-Fiber Bandpass Filter

Low-loss hollow-core optical fiber technology is attracting a lot of attention and is undergoing a rapid development in recent years [82]. Its inherent much lower nonlinearity and dispersion than the traditional solid-core communication fibers make it suitable for long-haul telecommunications [83]. Besides, since the signal is confined in the hollow core region, it undergoes shorter latency than the traditional solid-core communication fibers, revealing its potential in low-latency required short-haul scenarios [23]. The late demonstration of the transmission loss as low as 0.174 $\mathrm{dB\dot{k}m^{-1}}$ in telecommunication C bands in a double nested antiresonant nodeless hollow-core fiber is a milestone achievement [7]. One of the main shortcomings that restricts the wide adoption of the hollow-core fiber technology is the lack of hollow-core fiberized optical components. The beam constantly needs to be coupled into and out of the hollow-core fiber using freespace optics for various operations, which is often not practical outside laboratories. This is an important area that requires an immediate attention for realizing all-hollow-core fiber-based optical systems that are compact and robust.

In this chapter, a hollow-core in-fiber bandpass optical filter is demonstrated. The filter can be integrated seamlessly into an all-hollow-core fiber optic network, preserving the benefits of hollow guidance. Its working principle will be first discussed, followed by the fabrication details. The next section illustrates its experimental performance. Finally, a potential practical application is outlined.

3.1 Working Principle

The working principle of the hollow-core in-fiber bandpass filter is based on the antiresonant guidance in tubular-type hollow-core fibers. Figure 2.3 shows an idealized cross-section of one such fiber and its guidance mechanism. Recall Eq. 2.1, t, the wall thickness of the dielectric tubes, turns out to be one of the most influential geometrical parameters in dictating the transmission properties.

The hollow-core in-fiber bandpass filter capitalizes on these guiding properties. It is realized by tapering an AR-HCF, gently stretching the fiber under the heat. The heating temperature is kept as low as possible to cause only minimal disruption to the fiber structure during the down scaling. By sealing the two ends of the original fiber prior to tapering, the cladding tubes can be self-pressurized during the heating and avoid deformation of the inner microstructure. This tapering process produces a down- and an up-transition regions, and between the two, there is a taper waist, as depicted in Fig. 3.1. With a careful control, we can proportionally scale down and up the cross-sectional dimensions, including t, wall thickness, and D, core diameter, in the transitions. Then, the locations of the t-induced resonant bands and D-dependent long wavelength cutoff sweep across the spectrum accordingly along the taper. This is shown schematically in Fig.3.2. The blue-edge of the passband is defined by the tube wall thickness of the original fiber, t_0. The transmission in the region below the first resonance is suppressed by axially varying t along the length of the fiber. Namely, decreasing t down to a half of its original thickness, $0.5t_0$, shifts m-th resonance continuously to $2m$-th resonance of the original fiber, eliminating the entire blue side of the passband. On the other hand, the core diameter at the waist determines the long-wavelength edge. The cross-sectional reduction ratio of 0.5 - required for the total blue-side suppression - places the red edge of the passband at $0.05D_0$, where D_0 is the original core diameter. In principle, the optical filter can operate with just the first half of the taper containing the down-transition. However, having the other half with the up-transition enhances the suppression ratio and also helps to retain the mode profile after the filter.

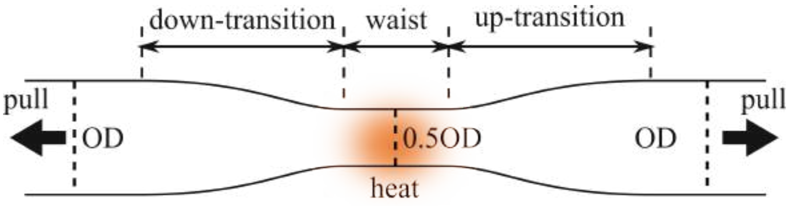

FIGURE 3.1: Illustration of the tapering process. OD: outer diameter.

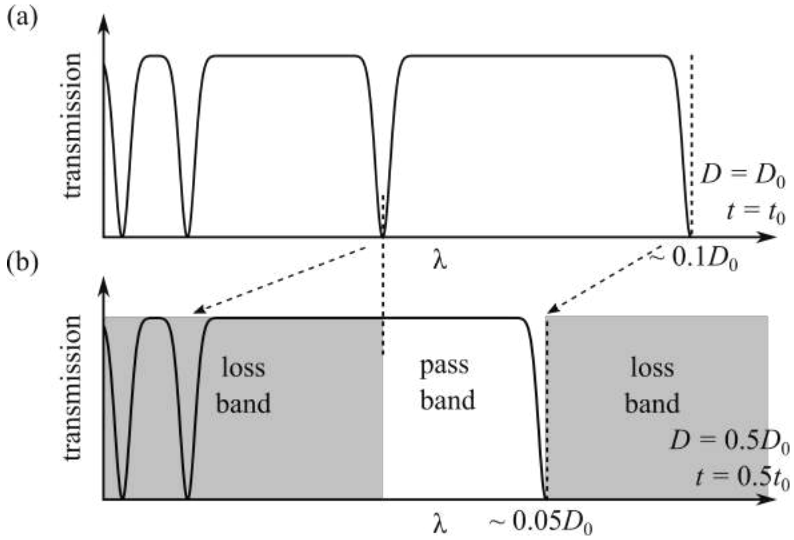

FIGURE 3.2: Transmission spectra of the antiresonant hollow-core fiber when (a) $t = t_0$ and $D = D_0$, and (b) $t = 0.5t_0$ and $D = 0.5D_0$. The resonant bands as well as the long wavelength cutoff sweep across the spectrum in the down- and up-transition sections in the tapered fiber. This filters out the spectrum in the shaded regions.

3.2 Fabrication by Tapering

We taper a seven-tube antiresonant hollow-core fiber that has $D_0 = 28.3$ μm and $t_0 = 430$ nm in a commercial glass processing system, Fujikura LZM-100, which uses a CO_2 laser with the power fluctuation of less than 0.5% as the heat source. This enables highly repeatable processes. The cladding tubes at both ends of the fiber are sealed to induce a small amount of self-pressurization during the tapering. This, together with a low heating temperature, assures the preservation of cross-sectional geometry throughout the taper [84]. The taper transitions in the axial direction must be adiabatic to minimize the loss due to the coupling of light in the fundamental core mode to other higher-order modes. This requires the transition length to be much longer than the beat length between the fundamental and first excited higher-order modes, L_{beat}, given by [85],

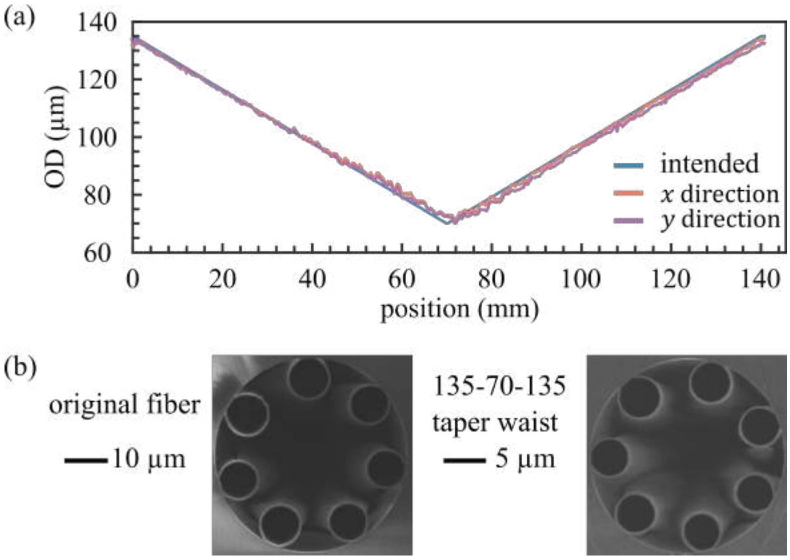

Figure 3.3: (a) OD versus position for the tapered section of the tubular antiresonant hollow-core fiber. OD: outer diameter. The blue line is the intended taper profile while the other two lines are the measured profiles across the two orthogonal axes. The original outer diameter of 135 μm is tapered down over 7 cm to 70 μm at the taper waist, which is followed immediately by the up-transition section of 7 cm returning to 135 μm outer diameter (135-70-135 taper). (b) Scanning electron micrographs of the original fiber (left) and taper waist (right) cross-sections.

$$L_{beat} = \frac{\lambda}{n_{eff1} - n_{eff2}} \tag{3.1}$$

where n_{eff1} and n_{eff2} are the effective indices of the two modes. We consider the coupling between the fundamental mode (LP01-like mode) and the lowest higher-order mode that has the same azimuthal symmetry (LP02-like mode), as shown in Fig. Their effective indices are calculated using the finite-element modeling for the idealized structures with two extreme cross-sectional dimensions in the taper. The resulting L_{beat} values are 0.09 and 0.02 cm at 1 μm wavelength in the untapered and taper waist geometries, respectively. We set the length of the down- and up-transitions to be 7 cm each, satisfying the adiabatic transition condition.

Figure. 3.3 shows the intended and measured outer diameters of the taper across the two orthogonal axes along the length of the fiber. The original antiresonant hollow-core fiber with the outer diameter of 135 μm is tapered down linearly over 7 cm to reach 70 μm outer diameter at the waist. The up-transition follows immediately returning to the original 135 μm at 7 cm after the taper waist (135-70-135 taper). The scanning-electron micrographs of the original fiber and taper waist cross-sections are presented in Fig. 3.3 (b). The core and average cladding tube diameters are scaled down from 28.3 μm to 13.5 μm and from 10.6 μm to 5.2 μm, respectively. Within the simple single-ring tubular geometry, the lowest loss is achieved when the ratio of cladding tube diameter to core diameter is 0.6–0.8 [63]. Considering that this ratio is 0.49 in Fig. 3.3 (b), there is still room for further reduction in loss that can be realized by controlling the cladding tube size. Although the ratio of tube-wall thickness to core diameter also affects the fiber confinement loss, it is not a parameter that can be designed freely since it is related to the passband bandwidth in the proposed fiber-based bandpass filter. For better improvement, we can adopt a fiber design that is optimized for ultra-low-loss transmission, such as the double nested antiresonant hollow core fiber [7]. We use the tapering ratio, T_R, defined by the dimension of a feature in the tapered fiber divided by its value in the untapered fiber, [84] to evaluate whether it is isomorphic tapering. That is to say, T_R should remain the same value for different features in isomorphic tapering. In our case, we achieved the tapering ratio of $\sim$ 0.5 for both core and average cladding diameters. The fiber structure is generally well maintained throughout the taper, and we can assume that D and t vary linearly along the taper in-line with the scaling of the outer diameter.

3.3 Bandpass Filtering Effect Characterization

We characterize the transmission property of the hollow-core in-fiber bandpass filter using the cut-back method. We employ a supercontinuum laser that spans 400-2400 nm and two optical spectrum analyzers each covering 350-1200 nm and 600-1700 nm. The measurements are plotted in Fig. 3.4 (a). Blue dashed-line is the transmission spectrum recorded before the filter, i.e., after cutting out the filter, and blue-solid line is that after the filter, i.e., before cutting out the filter. In the original fiber, we observe two resonant bands within the characterized bandwidth. They are at 815-1060 nm and 440-530 nm. The taper filters out the entire spectrum below the first resonant band, and the suppression ratio in the range between 20 and 40 dB is achieved in the blue-side lossband. The minimum insertion loss of 1.3 dB is measured at $\sim$ 1100 nm. We define the passband as the region where the insertion loss is less than 10 dB above the minimum insertion loss. This places the short- and long-wavelength edges at 1068 and 1416 nm. These are in good

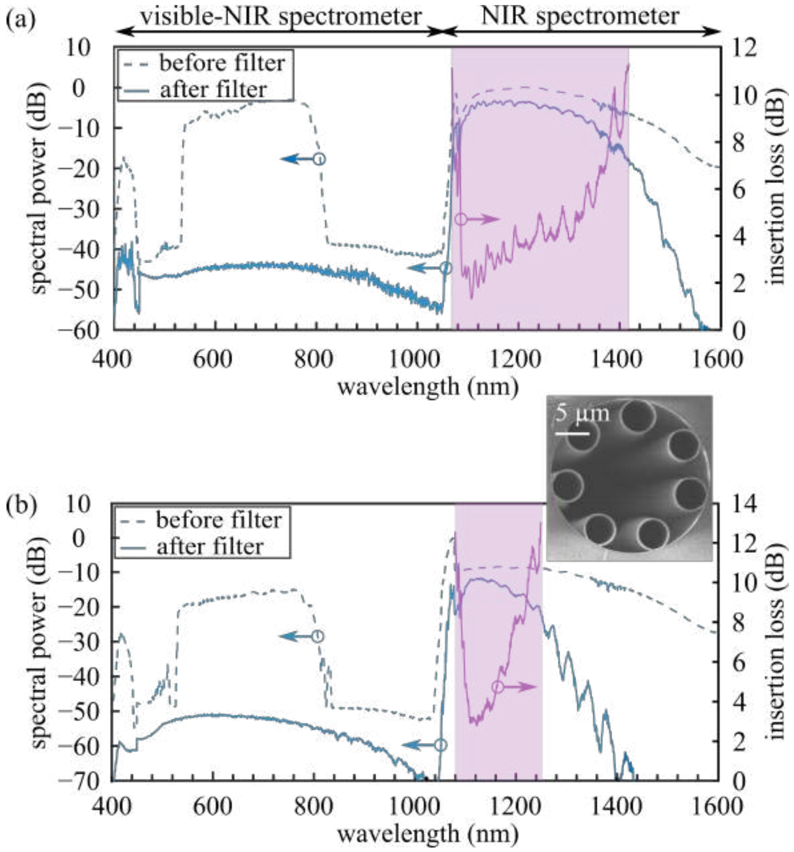

FIGURE 3.4: (a) Transmission spectra of the antiresonant hollow-core fiber (blue-dashed line) and 135-70-135 taper (blue-solid line) measured with a supercontinuum laser input spanning 400–2400 nm. The passband is indicated in purple shaded area, and its insertion loss is shown in purple-solid line. (b) Same measurements for the 135-60-135 taper. The inset shows the scanning electron micrograph of the 135-60-135 taper cross-section at its waist.

agreement with the expected values of $2t_0\sqrt{n^2-1}$ and $0.05D_0$ when the cross-sectional reduction ratio is 0.5 at the taper waist. The passband highlighted in red shade has the bandwidth of $\sim$ 350 nm. The insertion loss within the passband plotted in red-solid line shows the contrasting sharpness in the blue- and red-edges, which reflects the different suppression mechanisms.

We repeat the same measurements for a different taper fabricated from the same antiresonant hollow-core fiber. In order to check the effect of scaling down the cross-section further at the taper waist, we target the outer waist diameter to be 60 μm, while keeping the down- and up-transition sections to be 7 cm each (135-60-135 taper).The core diameter at taper waist, taken from the scanning-electron micrograph, is 12.8 μm, and the average cladding diameter is 4.8 μm, yielding a tapering ratio of 0.45. The transmission spectra before and after the filter with

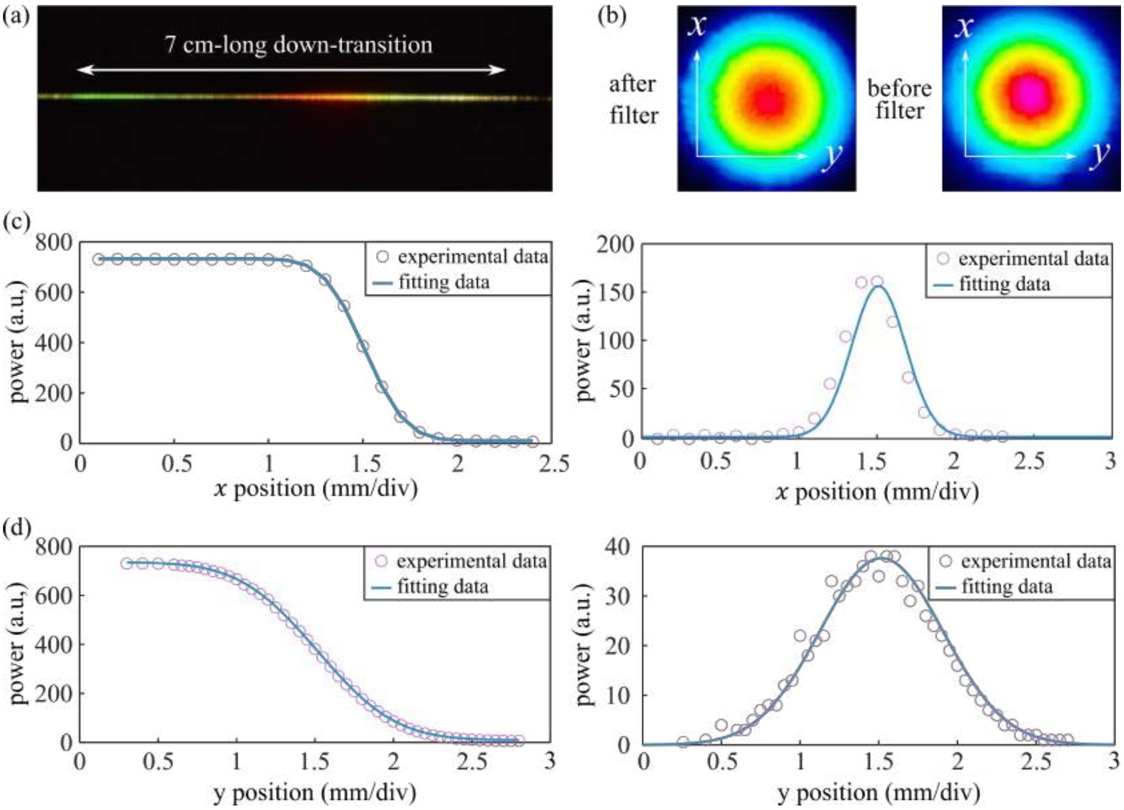

FIGURE 3.5: (a) Photograph of the down-transition part of 135-70-135 taper taken during the characterization. (b) Intensity mode profiles of the output beam taken after (left) and before (right) the 135-70-135 taper. (c) The power collected with respect to x position of the 135-70-135 taper at its waist, using the knife-edge technique (Left), and output beam profile in x direction (right). (d) The same process as (c) in y direction. The markers are the experimental data while the blue solid line is the fitting result.

the same supercontinuum source are presented in Fig. 3.4 (b). The inset shows the scanning electron micrograph of the 135-60-135 taper cross-section at its waist. The long-wavelength edge is brought forward to 1249 nm due to having a smaller core at the taper waist, whereas the blue-edge remains at a similar location at 1070 nm exhibiting a 180 nm-wide passband. These observations are in-line with the suppression mechanisms of the filter; the long-wavelength edge of the passband is determined by the core size at the taper waist, whereas the short-wavelength edge is set by the wall thickness of the cladding tubes in the original fiber. The 135-60-135 taper has the minimum insertion loss also at $\sim$ 1100 nm, but the loss is higher, at 2.8 dB due to the smaller core size at the taper waist. The cross-sectional reduction in the taper inflicts increased confinement loss, and therefore the insertion loss is inherent to the working principle of the device.

Figure 3.5 (a) is a photograph taken during the 135-70-135 taper characterization showing the light leakage along its down-transition. The light propagates from left to right in this picture. As the white light enters the 7 cm-long down-transition, green light first leaks out, followed by red, orange, and yellow light successively until the end. In the down-transition, the first resonant band which is originally at around 1000 nm sweeps across the spectrum down to about 470 nm. The spectrum within this moving resonant band leaks in sequence along the length. The initial leakage from the first resonant band is not in the visible spectrum, but there is also leakage from the second resonant band which is at roughly 500 nm. This is why it first illuminates green light. Further along the down-transition, the first resonant band moves into the visible region, and therefore emits the visible spectrum from red, orange, and yellow in sequence. The output beam profiles taken for the wavelength range of 350-1150 nm before and after the 135-70-135 taper are shown in Fig. 3.5 (b). The filter does not cause any major degradation of the mode profile. Note that this beam profile is captured by a CMOS camera (WinCamD-LCM) with the working wavelength from 355 to 1150 nm. Since the passband of our proposed filter is mainly starting from 1050 nm, at the edge of camera working bands, we also take the knife edge method to measure its mode profile. Left panel in both Fig. 3.5 (c) and (d) are power collected by progressively covering of the beam in both x and y direction, which is a typical knife edge method to measure a transverse profile of a laser beam. The blue solid line in both Fig. 3.5 (c) and (d) are the fitting results to the experimental data. The fitting parameter, R^2, in these two cases are 1 (closer to 1 means better fitting result). The right panels in both Fig. 3.5 (c) and (d) are the Gauassian beam profile according to the knife edge method. During this measurement, a thermal powermeter is used to avoid any wavelength-related problems.

3.4 Application: Near-Infrared Laser Source

While the performance of the in-line hollow-core fiber-optic filter demonstrated in this work leaves more to be desired when compared with commercial filters, it eliminates the need to couple the light beam into and out of the fiber, leading to an all hollow-core fiber-optic system that is simpler, more compact, and more robust. This is a major advantage considering that there are currently no standardized connectors for antiresonant hollow-core fibers, which makes the use of traditional functional components cumbersome. We find many potential applications of this versatile device. They can be used for suppressing noise in low-latency optical communication based on hollow-core fibers [86]. Besides, there is a large interest in utilizing antiresonant hollow-core fibers for guiding non-conventional spectral regions, such as vacuum-ultraviolet [19] and mid-infrared [5]. To generate vacuum-ultraviolet in hollow-core fiber, an extreme pulse compression and dispersive wave generation is utilized. As for generating mid-infrared, a similar process happens but with a phase-matched position at mid-infrared region by the so-called band-edge effect.

Recall Fig. 2.7 (a), the dispersion would be distorted when we include perturbations in solving GNLSE, leading to a phase-matching point in the high-frequency region. Once the pump is broadened enough under the interplay between negative dispersion and nonlinearity to seed the phase-matched position, part of the pump energy would be transferred to phase matching frequency, so-called dispersive wave generation. In AR-HCF, the presence of dielectric walls not only introduces periodical high-loss regions, it also distorts the dispersion landscape nearby dramatically, which is independent of the dispersion governed by Marcatili and Schmeltzer model. Those structural resonances lead to extra phase-matching frequencies, which are utilized in increasing generated supercontinuum bandwidth in gas-filled AR-HCFs [87], a strong narrow-band UV emission [88]. Beside, a notable experiment is the down-frequency conversion, from 800 nm to 1.45 μm achieved by utilizing this dramatically variation near the transmission band-edge [89]. This work has been extended by Deng et al., producing microjoule-level femtosecond pulses at 3.16 μm from 2 μm with the conversion efficiency as high as 9.4 % [90]. By simply tapering the fiber at the end of band-edge induced dispersive wave emission to integrate the in-fiber bandpass filter, we can build an all-fiber-based femtosecond mid-infrared single wavelength source, which can be a promising method for ultrahigh-sensitive molecular spectroscopy.

3.4.1 Perturbation Extension of the Marcatili–Schmeltzer Model

Due to the promising applications of antiresonant hollow-core fibers, there are several analytical models reported recently to describe the transmission properties of the antiresonant hollow-core fibers without the need of detailed finite-element simulations across the desired wavelength range [64, 65, 91]. In the paper [64], a complete analytical description of dispersion and losses in thin capillary fibers is showed by using the reflection of a wave on a single planar film. However, their perturbative approach was not able to capture the losses at the resonance wavelength at which the loss became infinite. For the paper [65], an analytical model for estimating confinement loss in Tube Lattice Fibers based on the single-tube model and the inhibited coupling waveguiding mechanism is proposed. Compared with these two models, the poor-man's model [91] can with a single fitting parameter quite accurately mimic dispersion and loss resonances and anti-resonances from full finite-element simulations. By using this model, a full picture of both dispersion and confinement loss of the antiresonant hollow-core fiber, especially in the resonant bands which are of the importance in the in-fiber bandpass filter, is easy to get captured. In this model, perturbation extension of the MS model is included,

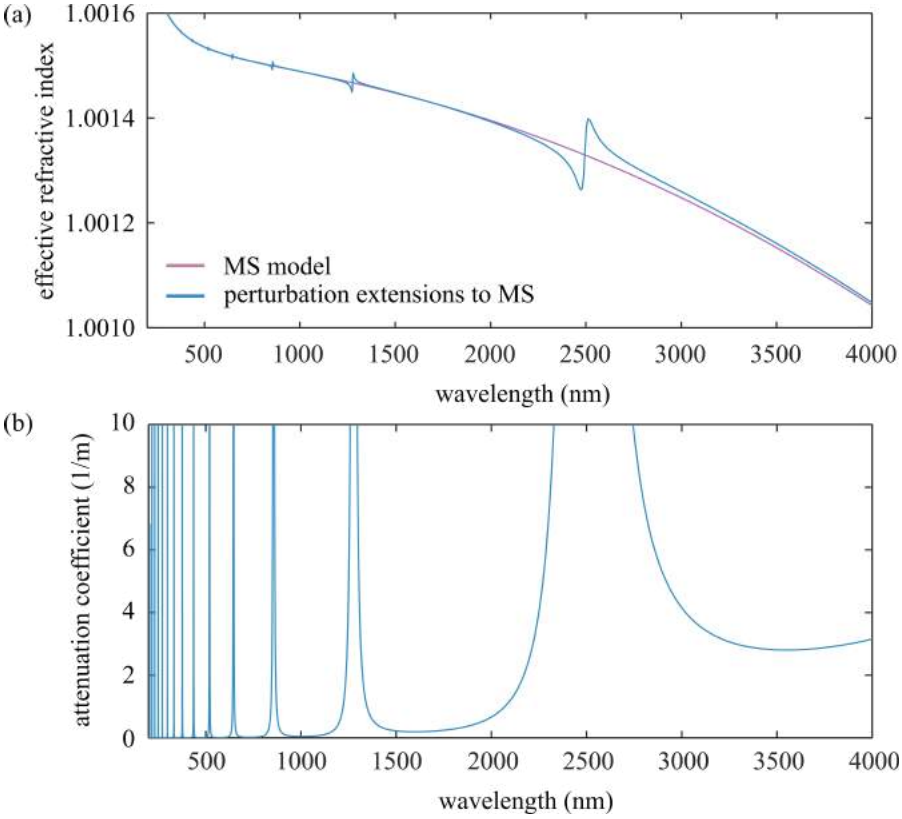

FIGURE 3.6: (a) effective refractive index calculated by the Marcatili–Schmeltzer (MS) model (purple) and the perturbation extensions to the MS model (blue). (b) the attenuation coefficient calculated by the perturbation extensions to the MS model. The AR-HCF calculated in both models is with a core radius of 50 μm and dielectric thickness of 1220 nm.

which is directly calculated the resonances of loss and dispersion by including the next-order contributions to the infinitely thick capillary case.

In the well-known MS model, the effective refractive index is

$$n_{eff,\mathrm{MS}}^2 = 1 - \frac{u_{mn}^2}{a_c^2 k_0^2} \tag{3.2}$$

where a_c is the core radius, k_0 is the vacuum wave number, $u_m n$ is the nth zero if the mth-order Bessel function. For the fundamental hybrid mode, TM and TE, we take the first zero of the zero-th Bessel function. In a gas-filled HCF, with the gas contribution, the transverse wave number is

$$\kappa = k_0 \sqrt{n_{gsa}^2 - n_{eff,\mathrm{MS}}^2}. \tag{3.3}$$

To obtain the perturbation extension of the MS model, we start from extending the transverse wave number κ in the case of infinitely thick capillary (in the vacuum condition for simplicity), as

$$\kappa = \begin{cases} \dfrac{u_{mn}}{a_c}(1 - i\dfrac{Z_d}{k_0 a_c}), & TE \\ \\ \dfrac{u_{mn}}{a_c}(1 - i\dfrac{Y_d}{k_0 a_c}), & TM \end{cases} \tag{3.4}$$

where Z_d and Y_d are introduced to be the impedance and admittance of the dielectric surface, as

$$Z_d = \frac{1}{\sqrt{{n_d}^2 - 1}} \approx \frac{k_0}{\sigma} \tag{3.5}$$

$$Y_d = \frac{{n_d}^2}{\sqrt{{n_d}^2 - 1}} \approx \frac{k_0 {n_d}^2 - 1}{\sigma} \tag{3.6}$$

n_d is the dielectric refractive index, and σ is the transverse wave number of dielectric, $\sigma = k_0\sqrt{n_d^2 - n_{eff,\mathrm{MS}}^2}$. From an infinitely to a finitely thick condition (thickness is Δ), we can replace the dielectric impedance Z_d and admittance Y_d by the TE and TM results, $Z_{\mathrm{TE}}, Y_{\mathrm{TM}}$:

$$Z_{\mathrm{TE}} = \frac{k_0(1 - i\dfrac{\kappa}{\sigma}\tan(\sigma\Delta))}{\kappa(1 - i\dfrac{\sigma}{\kappa}\tan(\sigma\Delta))} \tag{3.7}$$

$$Y_{\mathrm{TM}} = \frac{n_0^2 k_0(1 - i\dfrac{n_d^2\kappa}{\sigma}\tan(\sigma\Delta))}{\kappa(1 - i\dfrac{\sigma}{n_d^2\kappa}\tan(\sigma\Delta))} \tag{3.8}$$

Then we can arrive at the perturbation extension of the effective index n_{eff} and attenuate coefficient α for a hybrid mode,

$$n_{eff} = n_{eff,\mathrm{MS}} - \frac{u_{mn}^2}{a_c^3 k_0^3}\mathrm{Im}\left[\frac{\mathrm{Z}_{\mathrm{TE}} + \mathrm{Y}_{\mathrm{TM,}}}{2}\right] \tag{3.9}$$

$$\alpha = \frac{2u_{mn}^2}{a_c^3 k_0^2}\mathrm{Re}\left[\frac{\mathrm{Z}_{\mathrm{TE}} + \mathrm{Y}_{\mathrm{TM,}}}{2}\right] \tag{3.10}$$

The detailed derivative process can be found in [91]. The results, n_{eff}, α of a HCF with a 50 μm-radius core and 1220 nm-thick dielectric tubes, obtained by the MS model and the perturbation extensions to the MS model are shown in Fig. 3.6. Figure. 3.6 (a) clear shows that utilization of perturbation extensions introduces the resonances induced by finite thick tubes into the MS model, which is in line with Eq. 2.1. At the same positions of resonances, the high loss is observed in Fig. 3.6 (b). Meanwhile, the loss in each transmission band increases as the wavelength increases, since the core area is limited compared to the longer wavelength.

3.4.2 Simulation Results

The simulated system comprises two stage - first one is the near-infrared pulses generation in the original AR-HCF and another one is the in-fiber bandpass filter produced by the tapered AR-HCF. The sketch of the longitudinal sections of the AR-HCF in the simulation is presented in Fig. 3.7 (a). The fiber diameter of the first 25 cm is kept constant, 100 μm, ensuring the band-edge induced DW is emitted. In the second length of this AR-HCF, 15 cm long, a down-transition with a taper ratio of 0.45 is applied, serving as the bandpass filter. Figure 3.7 (b) shows the loss of the original fiber (up panel) and at the end of tapered fiber (bottom panel) respectively. The first resonance band is moved from around 2.5

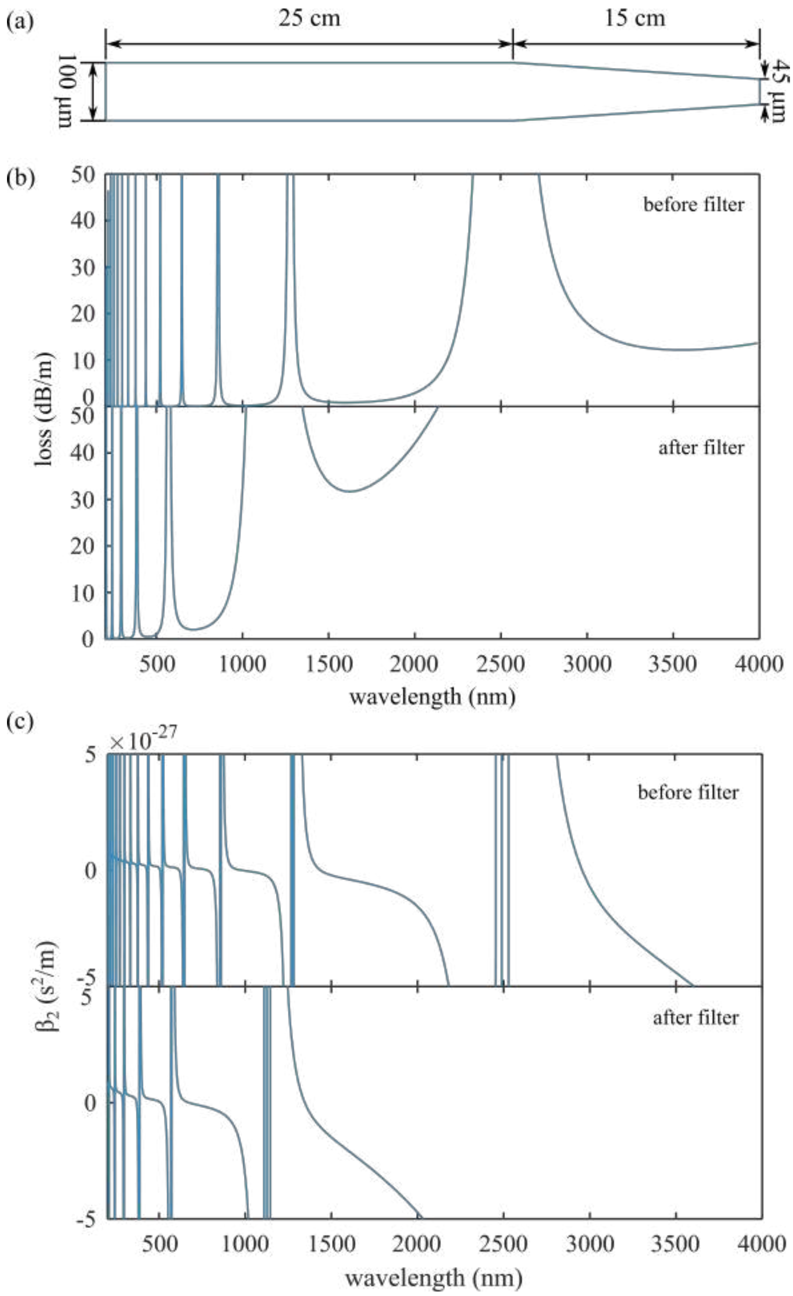

FIGURE 3.7: (a) Sketch of the longitudinal sections of the AR-HCF in the simulation. The first part is the 25 cm-long original AR-HCF with a core of 100 μm in diameter, while the second part is a 15 cm-long down-transition part in the tapered fiber with a taper ratio of 0.45. (b) The loss behavior before (upper panel) and after (bottom panel) the filter. (c) The dispersion behavior before (upper panel) and after (bottom panel) the filter.

μm to 1.2 μm since the cladding tube wall thickness has decreased by 0.45, and so are other high-order resonance bands. It is worth noting that the loss in the first transmission band has been increased enormously (larger than 50 dB/m) at the end of down-transition as the core size is decreased simultaneously, limiting the propagation of the longer wavelengths. Figure 3.7 (c) indicates the dispersion behavior before and after the filter. At the position of the resonance bands in Fig. 3.7 (b), there is a dramatic oscillation in the dispersion, causing the phase matching happens. In the simulation, the pump is at 2 μm, which is at anomalous

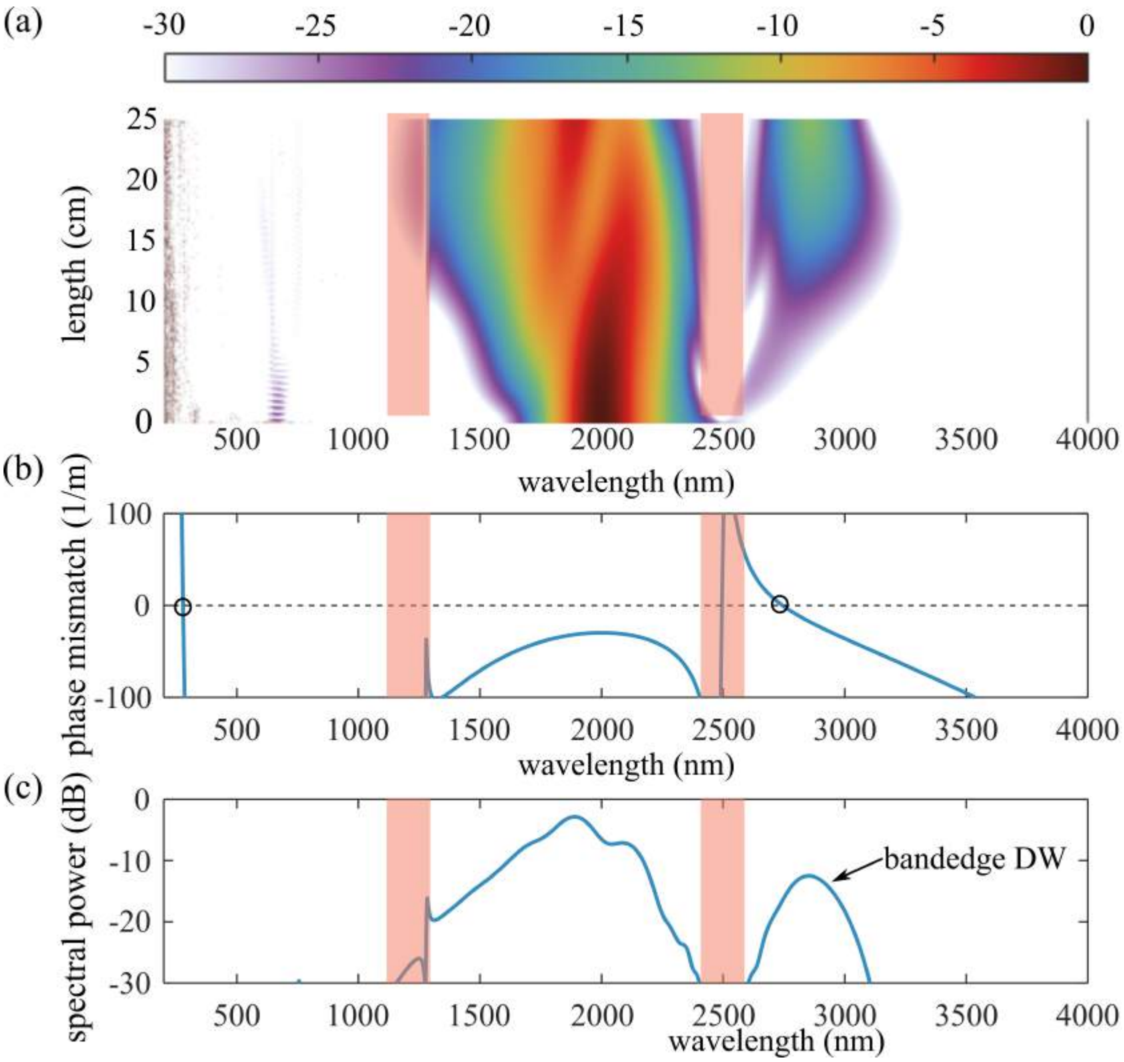

FIGURE 3.8: (a) Simulated spectral evolution along the 25 cm-long original AR-HCF for 20 fs, 16 μJ pump at 2 μm. The fiber is filled at 6 bar argon. The shaded areas represent the first and second resonance band. (b) Phase-mismatching diagram for 2 μm pump. The phase-matching points are indicated by the hollow circle mark, one is at 2.8 μm while another one is at 278 nm. (c) The simulated spectral profile at the end of 25 cm-long original AR-HCF. The bandedge DW at 2.8 μm is observed.

dispersion region at the first stage, ensuring the temporal compression and spectral broadening for the emission of bandedge induced DW.

Figure 3.8 (a) shows the simulated evolution along the first stage, the 25 cm-long original AR-HCF filled with 6 bar argon and pumped with 20 fs, 16 μJ at 2 μm, which amounts to a higher-order soliton of order 2.7. The pump is broadening in spectral domain through self-phase modulation and the mid-IR is observed in the form of DW at 2.8 μm from 15 cm. This 2.8 μm mid-IR is at the blue-edge of the first transmission band while the 2 μm pump is at the second transmission band. As shown in Fig. 3.8 (b), this bandedge DW generation is attributed to the phase-matching process, written as,

$$\Delta\beta = \beta - \beta_0 - \beta_1(w - w_0) - \frac{3w^2\epsilon_0\mu_0}{8\beta}\chi^{(3)}|E_0|^2 \tag{3.11}$$

where β_0 and β_1 are the first and second order coefficients of the Taylor series expansion of β at the pump, w_0. The last term in Eq. 3.11 is the nonlinear correction term, where E_0 is the peak electric filed strength of the input pulse. In the Fig. 3.8 (b) of phase-matching, we observe two phase-matching points, one is at 2.8 μm, originating from the rapid variation in the dispersion near resonance band, another one is at 278 nm, from the phase-matching in the dispersion controlled by gas pressure and fiber core dimension. For simplicity, we call the emitted DW from the two different phase-matching mechanism to be bandedge DW and Marcatili DW, respectively. As shown in 3.8 (a), the Marcatili DW emission is not observed in the pulse evolution, since the pulse broadening is not sufficient to UV range. In the output spectral profile at the end of the first stage, as shown in Fig. 3.8 (c), another weaker peak observed at 1.3 μm, which is at the blue-edge of the second transmission band, is related to another bandedge phase-matching point. However, the discrepancy in Fig. 3.8 (b) at 1.3 μm, as we shall explain, is associated to not enough grid points in simulation.

After the emission of this mid-IR bandedge DW centered at 2.8 μm is completed, we add the second stage, the down-transition part of the tapered fiber to serve as a in-fiber bandpass filter, as shown in Fig. 3.9 (a). Figure 3.9 (b) is the simulation result with the same length as (a) but without the tapered part. As expected, the down-transition part with the taper ratio of 0.45 filters out all the spectrum except the first transmission band of the original AR-HCF. The marked area in Fig. 3.9

(a) shows the blue-shifted DW, as the phase matching point induced by resonance band is blue shifting - an evidence that the perturbation extension of the MS model is reliable. With the decrement of thickness, the core diameter is decreased, causing the loss of the generated 2.8 μm is increased. At the end of the second AR-HCF stage, only the mid-IR pulses remains, albeit with a loss compared to the end of the first stage of the AR-HCF. Red dash line in Fig. 3.9 is the pump pulse 2μm, while the blue and purple lines are the output spectral profiles of (a) and (b) respectively. Comparing the output spectrum of (a) and (b), we can conclude that the suppressing ratio of this in-fiber bandpass filter can be about 30 dB while the insertion loss at 2.8 μm is 3.7 dB. The inset of Fig. 3.9 (c) shows the temporal domain profile at the end of the in-fiber bandpass filter, with 104 fs duration at the full-width at half-maximum (FWHM). We define the conversion ratio as the energy of generated mid-IR pulse divided by the pump energy. In the simulated result presented here, the overall conversion efficiency is 2%.

3.5 Summary

The antiresonant hollow-core fiber offers transmission of high-power beam over ultrawide spectral range. Their development in its confinement loss reduction recently has demonstrated its huge potential for use in the next generation optical communication systems. To truly realize wide adoption of antiresonant hollow-core fibers outside the laboratory environment, we must address the current lack of hollow-core fiber-based functional devices that can easily be incorporated into hollow-core fiber optical networks.

In this Chapter, we utilized the guidance property of the AR-HCF to realize a fiber-based bandpass optical filter. This is achieved by tapering a piece of AR-HCF to reduce the cross-sectional dimension to one half of its original size at the taper waist. The blue side is filtered by exploiting the dielectric wall thickness-induced loss bands that sweep across the entire short wavelength region as the thickness varies along the length, while the long-wavelength cut-off is determined by the change in the core diameter to wavelength ratio. The device carries the benefits of hollow-core guidance and integrate seamlessly into a hollow-core fiber-based system with a relatively low insertion loss by placing it in-line in a fiber link.

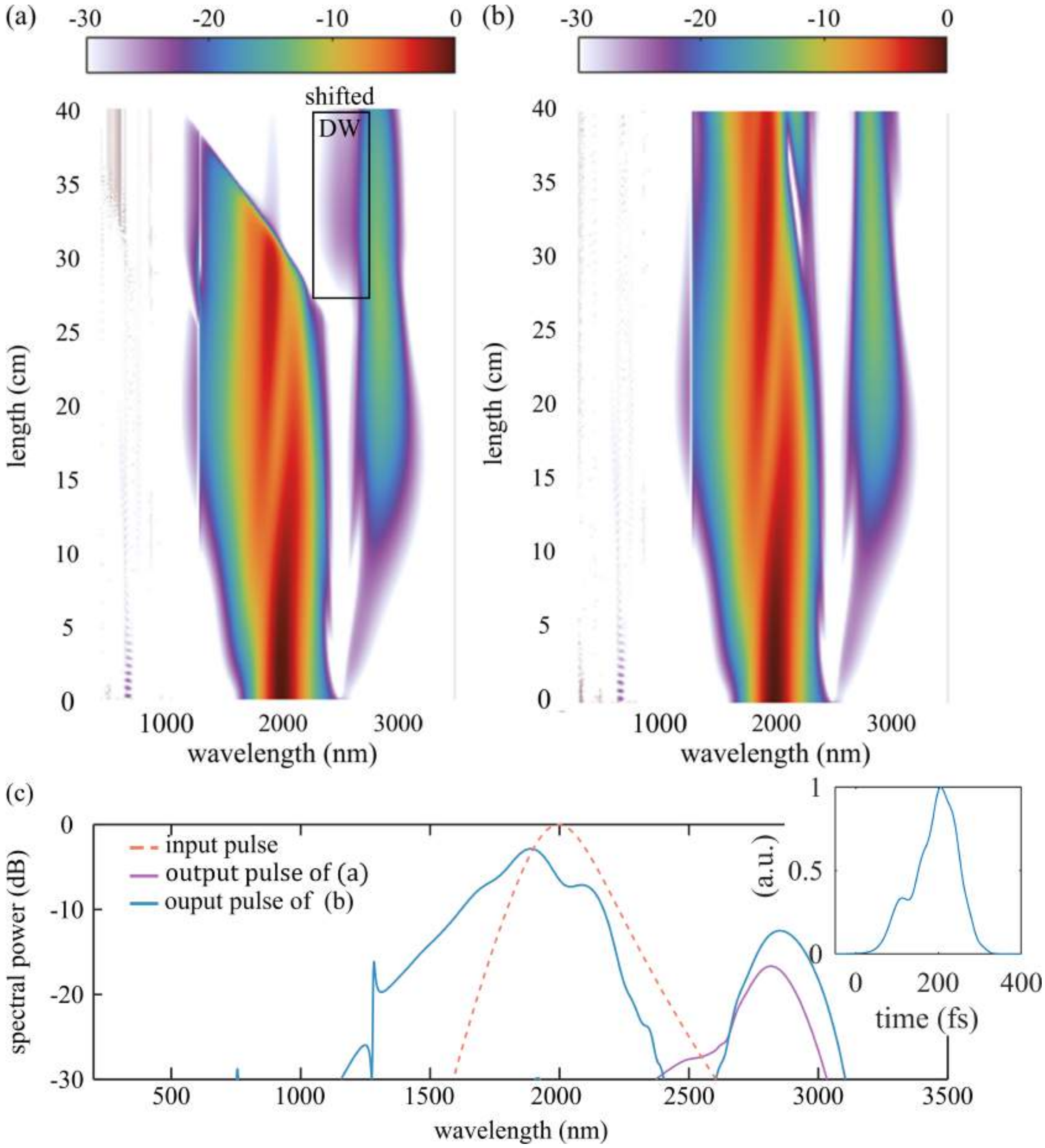

FIGURE 3.9: Simulated spectral evolution along the 40 cm-long AR-HCF for 20 fs, 16 μJ pump at 2 μm. The fiber is filled at 6 bar argon with (a) and without (b) a 15 cm-long down-transition part. (c) The simulated spectral profile at the end of input pulse, output pulse of (a) and (b). The bandedge DW at 2.8 μm is clearly observed.

Moreover, a practical application is proposed - by seamless tapering a piece of AR-HCF after the bandedge DW emission in that fiber, we can achieve a micro-joule level femtosecond pure mid-infrared laser source.

Chapter 4

Low-Energy-Threshold Nonlinear Generation of Ultraviolet

The ultrafast laser in the UV range is of great importance in many applications, such as the time-resolved spectroscopy, microscopy, material processing [92–94]. Nonlinear wavelength conversion is a common method to generate ultrafast laser pulses in the ultraviolet range from very early days of lasers to the present. However, the efficient frequency up-conversion is limited in nonlinear crystals since the limited transmission bandwidth, damage threshold, the large group velocity mismatch, and the complex crystal growth processes [95–97]. An alternative method is the nonlinear frequency conversion in gases, such as high-harmonic generation (HHG). Although it alleviates all the limitations raised from the solid nonlinear medium, it requires very intense light pulses to be focused into a gas to compensate the low nonlinearity of the gases. Besides,However, this level of energy is hard to be achieved directly in a high-repetition rate modelocked laser source, which requires a carefully designed enhancement cavity, causing the whole setup become sensitive and complex. Moreover, HHG only works at wavelength set by the harmonics of the pump with a very low conversion efficiency, $\leq 0.1\%$.

Since its first experimental demonstration [35], the generation of deep- and vacuum-ultraviolet in the gas-filled hollow-core fiber has attracted vast interest from the researchers in the field. It exploits (i) the hollow-core fiber's ability to guide the light in the ultraviolet spectral region without causing permanent damages to the guiding medium, and (ii) the unique dispersion landscape that permits phase-matched transfer of energy from the pump to the ultraviolet through a nonlinear frequency conversion process [98]. In addition to the dispersive wave generation in the gas-filled HCF system, another commonly used method to generate UV and vacuum UV is the high-harmonic generation (HHG), which requires very intense light pulses to be focused into a gas. However, this level of energy is hard to be achieved directly in a high-repetition rate modelocked laser source, which requires a carefully designed enhancement cavity, causing the whole setup become sensitive and complex. Moreover, HHG only works at wavelength set by the harmonics of the pump with a very low conversion efficiency, $\leq 0.1\%$.

In this chapter, we propose that by confining the light into the AR-HCF with a very small core size, the pump energy threshold for emitting deep UV can be substantially decreased, which illustrates its potential for building a compact all-fiber-based UV frequency comb source.

4.1 Energy Scaling of Soliton Dynamics

For the onset of UV in the gas-filled hollow-core fiber through extreme soliton compressing and dispersive wave generation, pump must accumulate sufficient nonlinear phase shifts along the propagation. One common drawback of the gas-based system in this respect is its relatively small nonlinear index. For instance, the third-order susceptibility of argon at its standard pressure and temperature is about four orders of magnitude lower than that of fused silica [80]. While this shortfall can be compensated to some degree by increasing the gas pressure or choosing heavier gas, doing so also largely affects the dispersion, shifting the phase-matching point towards longer wavelength which may not be desirable in many applications. Alternatively, one can use longer propagation distance or higher pump peak power to produce enough nonlinear phase shifts. However, the former is subject to transmission and bending losses in the hollow-core fiber, and the latter raises the bar on the pump source requirement. One simple approach to mitigate the issue is to come up with a hollow-core fiber that tightly confines light into very small mode area. In the small-mode-area hollow-core fiber (SMA-HCF), much higher intensity is achieved for a given peak power, allowing large nonlinear effects to be induced from relatively small pulse energy.

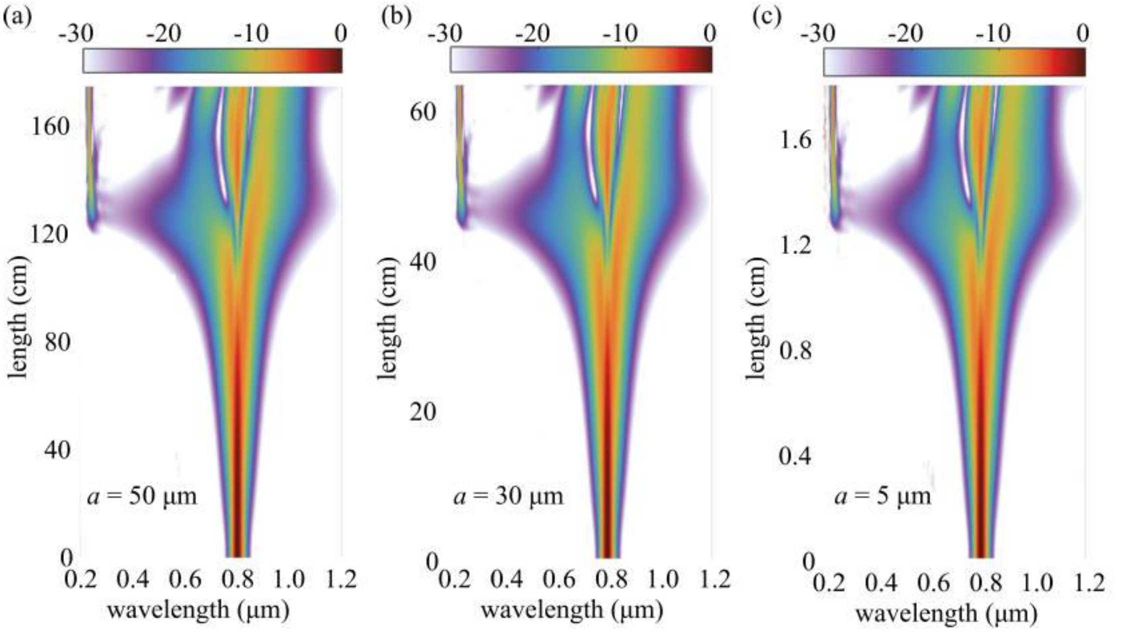

FIGURE 4.1: Simulated examples of the same soliton dynamics with the choice of $\lambda_0 =$ 520 nm and $N = 4.5$ in different gas-filled HCF systems. (a) The HCF with 50 μm core radius a pumped with 12 μJ 30 fs pump and 0.5 bar argon; (b) The HCF with 30 μm core radius pumped with 4.3 μJ 30 fs pump and 1.4 bar argon; (c) The HCF with 5 μm core radius pumped with 121 nJ 30 fs pump and 49.5 bar argon.

It exploits the universal energy scaling in gas-based nonlinear optics [99], which is a striking feature of this theory. This energy scaling ability in gas-filled HCF system is dependent on its dispersion landscape [57] - we can observe the same soliton dynamics for a given choice of zero-dispersion wavelength (ZDW) λ_0 and soliton order N in drastic systems. Despite the different fiber parameters (core size), one can always find the correct filling gas species, pressure and pump energy to fix the λ_0 and N. The examples of the energy scalability are illustrated in Fig. 4.1. It shows that for a given choice of λ_0 and N, we can have a wide range combination of fiber size, pump requirement and gas conditions. In the three numerical examples, the combination of λ_0 and N is fixed to be 520 nm and 4.5, while the other parameters are very different. The requirement for pump energy is decreased a thousand times from 12 μJ in Fig. 4.1 (a) to 0.12 μJ in Fig. 4.1 (c) while the core radius is shrunk from 50 μm to 5 μm.

Up-scaling of the process demonstrated in a large-core capillary led to generating microjoule-level UV pulses [49]. The down-scaling has also been tested in a kagomé-type hollow-core photonic-crystal fiber with flat-to-flat core diameter of 22 μm, achieving the UV radiation from 500 nJ pump [100]. We note, by confining the beam further into $< 50\,\mu\text{m}^2$, the pulse energy requirement for the UV emission can be reduced to sub-hundred nanojoules - to a level that is accessible by modern compact femtosecond oscillators operating at multi-megahertz repetition rates [101]. This opens a potential pathway to develop a compact and robust UV frequency comb source.

4.2 Deep UV Generation in Gas-Filled Small-Mode-Area HCF

4.2.1 Fabrication and Characterization of Small-Mode-Area HCF

Fabricating a small-scale low-loss hollow-core fiber directly from the drawing tower is challenging. This is because, without a careful control, the cladding elements tend to stick to each other due to surface tension, forming dielectric nodes that substantially degrade light guidance [102]. Among the tubular-type hollow-core fibers, the smallest core diameter achieved straight from the thermal drawing so far is 15 μm intended to guide light at 355nm [18]. One attractive approach to overcome this difficulty is to post-process the fiber in a tapering rig to gently stretch it under heat in a well-controlled manner. We have demonstrated using the transition parts of a tapered AR-HCF produced by this technique to serve as the in-fiber bandpass filter in Chapter 3. In this Chapter, the waist part illustrated in Fig. 3.1 can serve as a SMA-HCF. The smallest report of the core diameter of a tubular HCF achieved by this technique is 5.8 μm [84].

For the fabrication of SMA-HCF, a tubular hollow-core fiber with the original core diameter of 25.6 μm is used. In our setup, we can produce the taper waist of up to 15 cm in length which is sufficiently long for the experiment to follow. Figure 4.2 (a) and (b) shows scanning electron micrographs of the original fiber and SMA-HCF cross sections respectively. The core diameter is scaled down from 25.6 to 10.6 μm, and the cladding tubes are also reduced, on average from 11.2 to 4.45 μm in diameter, achieving the tapering ratio of approximately 0.4. The overall structure is well maintained without the formation of any dielectric nodes between the cladding elements. The transmission spectra of the original fiber and SMA-HCF obtained using a high-power xenon lamp are plotted in Figs.4.2 (c). Shaded regions are the high-loss bands that appear due to the cladding element wall thickness. A reduction in the wall thickness from 415 nm in the original fiber to 186 nm in SMA-HCF blue-shifts these loss bands correspondingly. That is, the first high-loss band is moved from 800 - 960 to 380 - 420 nm, and the second one is pushed from 440 - 490 nm to, supposedly, 200 – 220 nm which is outside the coverage of our xenon lamp. In the transmission of SMA-HCF, light guidance in the core is not supported beyond 970 nm. This cut-off shifts to shorter wavelength with further reduction in the cross-sectional structure, placing an ultimate limit on the applicable scaling-down factor for given pump wavelength. The oscillations seen in the transmission spectra in Fig. 4.2 (c) are attributed to the outer jacket thickness-induced resonances. Here, the outer jacket acts as an additional antiresonant reflection layer, resulting in the high-loss regions that are uniformly separated at a frequency governed by its thickness. This effect is comprehensively studied in thin-wall dielectric capillaries of different wall thicknesses [103]. In our experiment, the jacket thicknesses are 7 and 2.9 μm, amounting to the separations of 14.8 and 35.7 THz for the original fiber and SMA-HCF, respectively. These values are in good agreement with the fringe patterns in Fig. 4.2 (c).

The loss spectrum of SMA-HCF calculated using finite-element modeling is presented in Fig. 4.3 as reference. Here, a uniform tubular hollow-core fiber that has a 10.6 μm-diameter core surrounded by six cladding tubes of diameter 4.45 μm and wall thickness 186 nm is assumed. Figure 4.3 also shows the expected normalized transmission of the 5 cm-long SMA-HCF, which is obtained from the calculated loss and source spectrum. The cut-off wavelength and locations of the high-loss bands in the calculation are in excellent agreement with the measured values. From the modeling, the loss is 11 dBm^{-1} at 800nm which is close to the measured value via cut-back method, 16 dBm^{-1}. The effective mode area of SMA-HCF is calculated to be 51.3 μm^2 at 800 nm. The small mode area presents an ideal platform for hosting nonlinear experiments at low pulse energies.

Within the simple six tube geometry, the lowest loss is achieved when the ratio of cladding tube diameter to core diameter is 0.6–0.8 [104]. Considering that this ratio is 0.42 in SMA-HCF, there still is room for further reduction in loss that can be realized by controlling the cladding tube size during the fabrication. For better

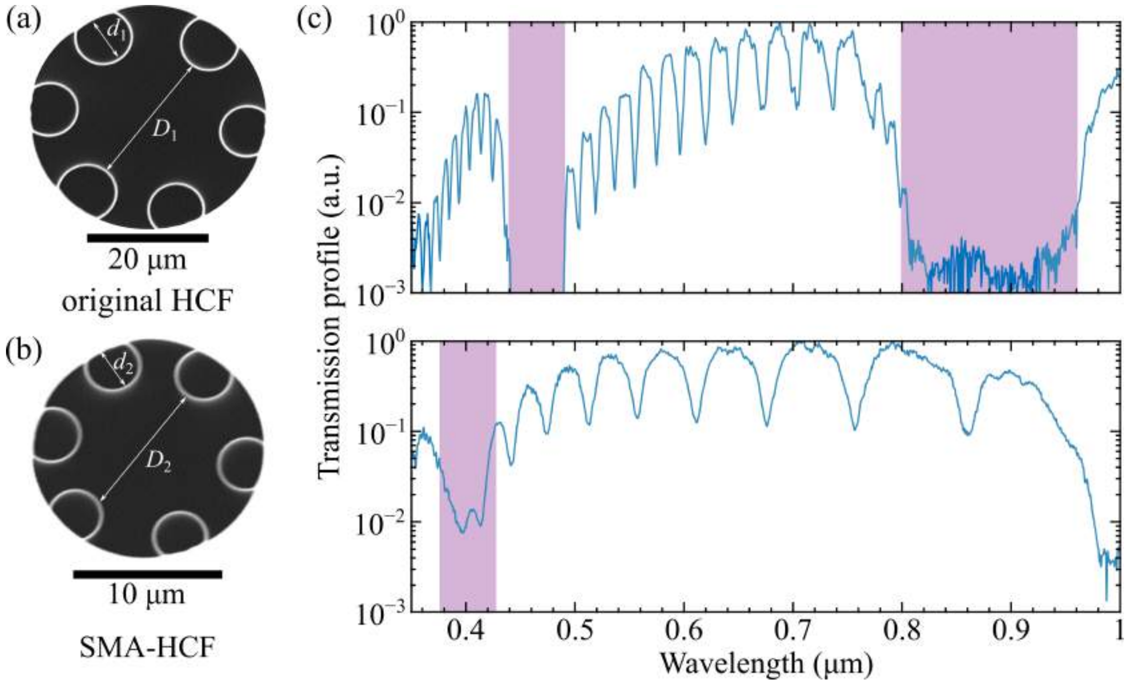

FIGURE 4.2: (a) Scanning electron micrographs (SEM) showing cross sections of the original tubular hollow-core fiber with a core diameter D_1 in 25 μm, cladding diameter d_1 in 11.2 μm and (b) that of the SMA-HCF produced via tapering with a core diameter D_1 in 10.6 μm, cladding diameter d_1 in 4.45 μm. (c) Transmission spectrum of the original fiber (upper panel) and SMA-HCF (bottom panel). Shaded regions are the high-loss bands that appear due to cladding element wall thickness.

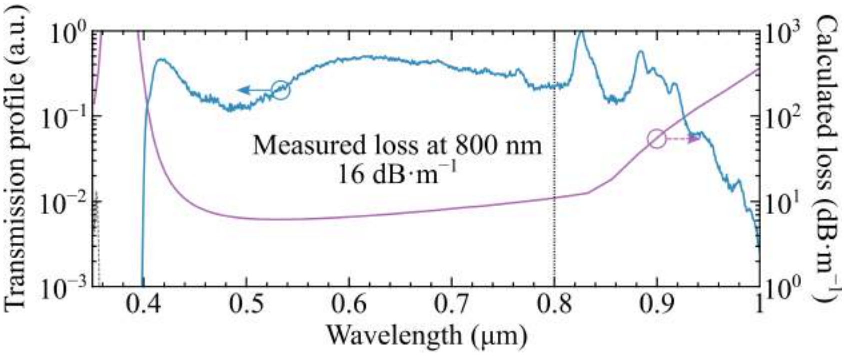

FIGURE 4.3: The loss spectrum of SMA-HCF calculated using finite-element modeling and the expected normalized transmission of the 5 cm-long SMA-HCF, obtained from the calculated loss and source spectrum.

improvement, we can adopt a fiber design that is optimized for ultra-low-loss transmission, such as the nested antiresonant nodeless hollow core fiber. Alternatively, the system can be pumped at shorter wavelength, e.g. at the second harmonic, to increase the core diameter to wavelength ratio, which is the dominant factor influencing loss in hollow-core fibers [105].

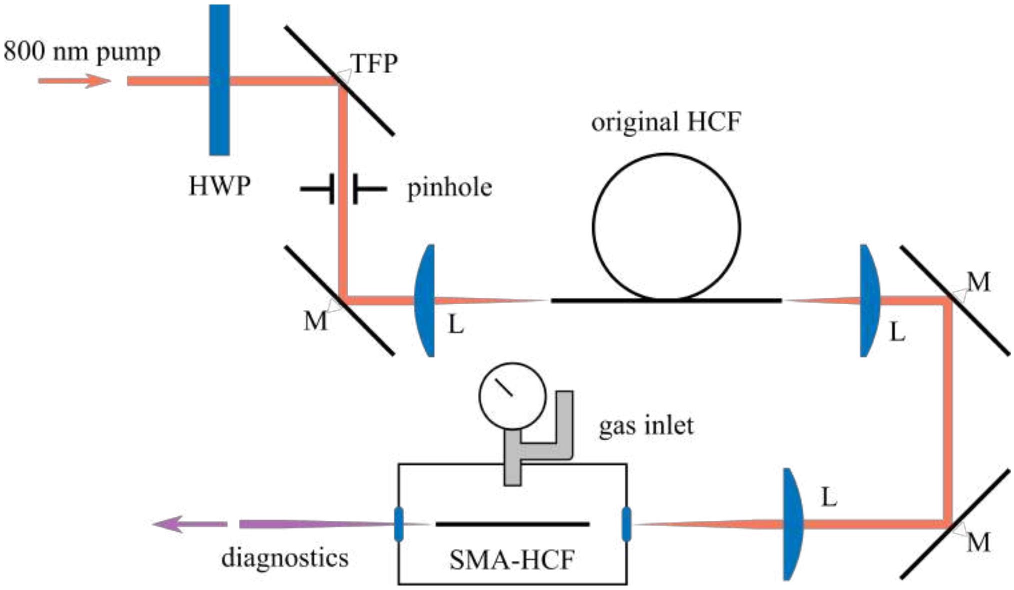

FIGURE 4.4: Schematic of the experiment setup. HWP: half-wave plate; TFP: thin-film polarizer; M: mirror; L: lens.

4.2.2 Deep UV Generation

The experimental setup is illustrated in Fig. 4.4. A 5 cm-long SMA-HCF is placed inside a gas chamber which is pressurized with argon. There are two 3 mm-thick CaF_2 windows attached on the sides of the gas chamber providing optical access to the fiber. The system is pumped by femtosecond pulses at 800 nm from a Ti:sapphire laser operating at 1 kHz repetition rate. The power is adjusted with a half-wave plate and a thin-film polarizer. The beam is filtered beforehand, first through a pinhole, then in a 7 cm-long original hollow-core fiber to improve its spatial quality. This substantially enhances the light coupling into SMA-HCF which otherwise is difficult due to sheer size of the fiber core.

Figure 4.5 (a) and (b) shows temporal intensity and phase profiles of the pump after passing through the input window attached to the gas chamber. They are obtained using home-built second-harmonic generation frequency-resolved optical gating (FROG) [106]. In Fig. 4.5 (a), both temporal intensity and chirp are presented. The corresponding measured and reconstructed spectral profiles are plotted in Fig. 4.5 (b) in dash and solid line respectively. The match between the acquired and retrieved spectrograms presented in Fig. 4.5 (c) is good with only 0.8% root-mean-square difference between them. The full-width at the half-maximum (FWHM) duration of the pump at the input of fiber is 52 fs, broadened

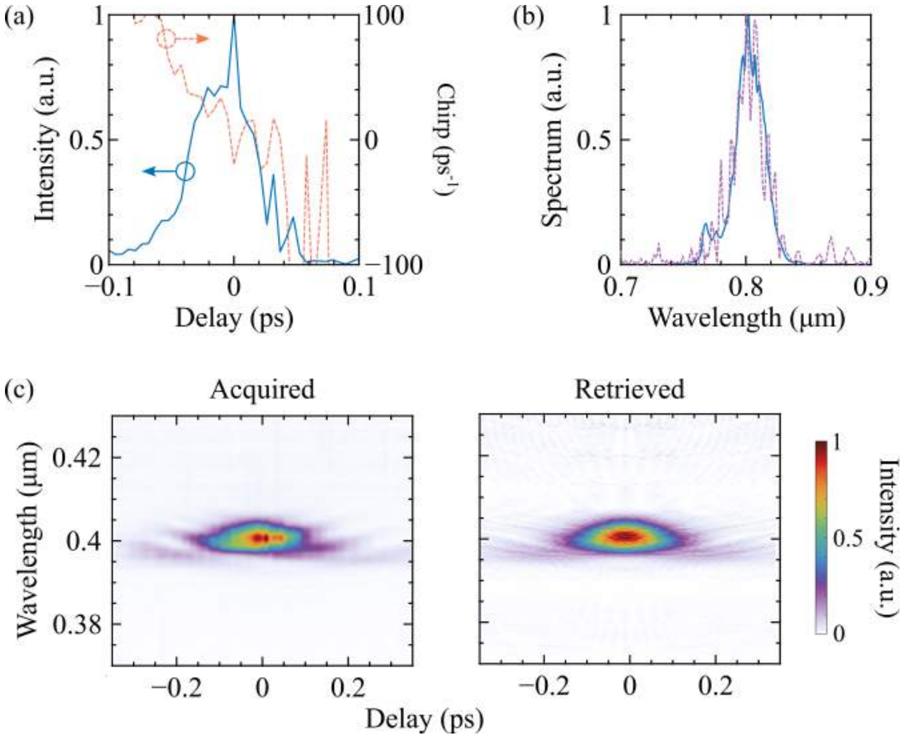

Figure 4.5: (a) Intensity (blue-solid line) and phase (red-dashed line) profiles of the pulse at the input of fiber obtained using second-harmonic generation frequency-resolved optical gating technique. (b) Measured (blue-solid line) and reconstructed (purple-dashed line) spectral profiles at the input of fiber. (c) Acquired (left) and retrieved (right) spectrograms.

from the original duration of 40 fs at the laser output. The spectral bandwidth measured at the same position is 8.4 THz, which is identical to that of the laser indicating that no significant nonlinear effects are introduced to the pump until it reaches SMA-HCF though passing through an extra AR-HCF.

For the measurement of output spectrum, the exiting beam emerging from the output window of the gas chamber is collected directly using a fiber patch cable attached to the spectrometer. This raw measurement is intensity calibrated by applying spectral response functions of the diagnostic instruments. Further to that, rather low average power at the output of SMA-HCF makes it impractical to use an integrating sphere to collect the entire beam into the spectrometer. Hence, when taking measurements, the end-face of the patch cable is placed at the center of the output beam. Since the divergence angle of the beam depends on the wavelength, the recorded spectrum needs to be scaled by the square of the wavelength to obtain true spectral composition of the total output. We affirm that the measured spectra presented in the subsequent sections have this correction factor applied.

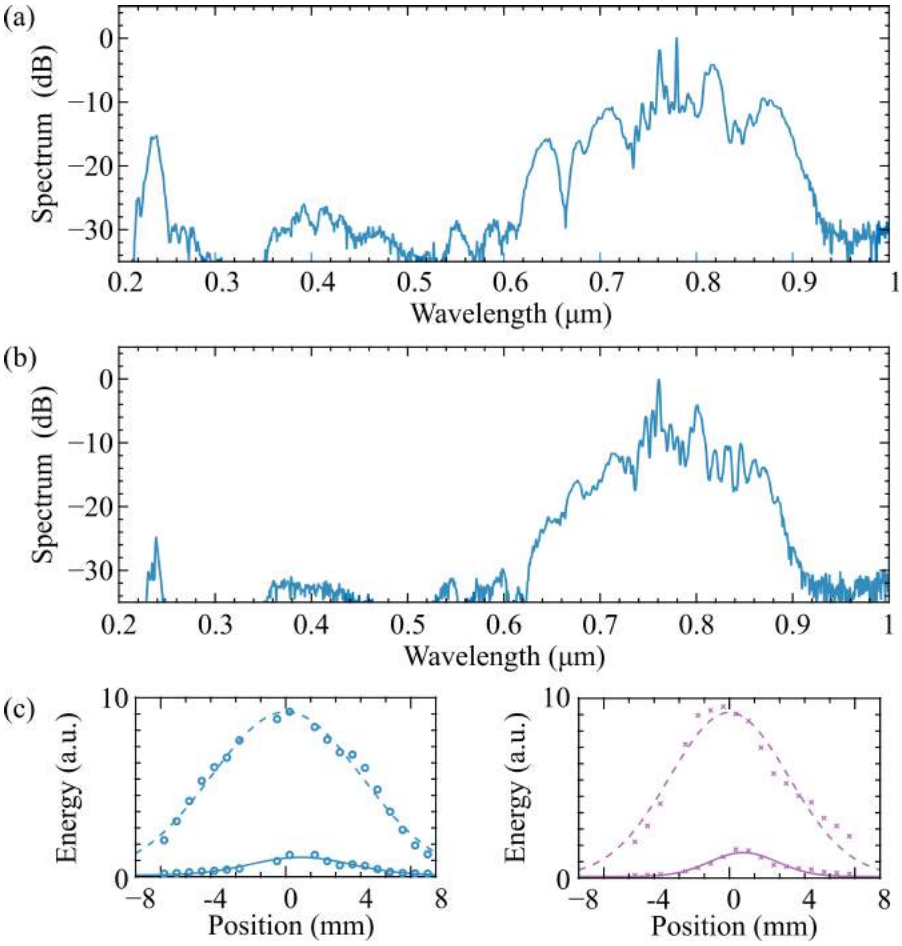

FIGURE 4.6: Spectra of the beam exiting the 5 cm-long SMA-HCF pressurized with 40 bar argon when the observed output pulse energies are (a) 125 nJ and (b) 100 nJ. The corresponding pump energies are 150 and 125 nJ, respectively. (c) Energy contained in the entire spectrum and that in the UV part (¡400nm) of (a) when the end face of the light collecting patch cable is moved across the output beam horizontally (left) and vertically (right) crossing the center. They exhibit excellent Gaussian fits - the solid line is for the entire spectrum while dashed one is for the UV part - indicating that the pump and UV radiations both emerge from the fundamental core mode in SMA-HCF.

Figure 4.6 (a) is the spectrum of the beam leaving SMA-HCF when the measured output pulse energy is 125 nJ. This corresponds to estimated input pulse energy of 150 nJ taking into account attenuation in the 5 cm-long SMA-HCF. The launch efficiency is approximately 24%. Here, the gas chamber is pressurized with argon at 40 bar. We observe broadening of the pump spectrum and presence of the UV radiation band centered at 243 nm with its peak reaching approximately 15 dB down from that of the pump spectrum. The energy contained within the UV range ($\leq$ 400 nm) estimated from the intensity calibrated spectrum is 2.6 nJ, amounting to 2.1% of the total output. Shown in Fig. 4.6 (c) is how the energy contained in the entire spectrum and UV part ($\leq$ 400 nm) vary when the end face of the light collecting patch cable is moved across the output beam horizontall and vertically crossing the center. They exhibit excellent Gaussian fits, indicating that the pump and UV both emerge from the fundamental core mode in SMA-HCF.

The UV radiation weakens as the pump energy is decreased, and it disappears into the noise when the observed output pulse energy is below 100 nJ. This amounts to the pump energy of 125 nJ. At this point, there is only a small peak that is approximately 30 dB down from the pump at 239nm as shown in Fig. 4.6 (b). We highlight that the demonstrated pump energy threshold is the lowest reported so far, and is at the level that can be delivered by modern high-repetition-rate femtosecond laser oscillators. One major limiting factor in this regard is the poor coupling efficiency, which we believe can be improved with further engineering of the gas chamber and fiber coupling optics.

We examine our observations numerically by solving the uni-direction field propagation equation, Eq. 2.16. We assume propagation only in the fundamental mode of SMA-HCF. Its linear dispersion is accounted for in β where pressure dependent contribution from the gas is obtained using a Sellmeier equation [79].The waveguide portion of β and transmission loss a are calculated using finite-element modeling. The last term is accountable for photoionization which has negligible effect for the cases studied in this work, but is nevertheless included for the sake of completeness.

Figure 4.7 (a) shows the simulated spectrum at the output of the 5 cm-long SMA-HCF filled with argon at 40 bar for the 150 nJ pump. The experimentally measured spectrum for the same condition is presented in gray-shade for reference. All importan features, such as the width of the emission band at 240 nm and that of the broadened pump, are well replicated in the simulations confirming relevance of the model. One major discrepancy observed at 400 nm, as we shall explain, is associated with irregularity of the SMA-HCF structure used in the experiment.

The UV is generated in the form of dispersive wave. The spectral evolution along SMA-HCF leading to this output is presented in Fig. 4.7 (b). After the launch, the 150 nJ-pump, which amounts to a higher-order soliton of order 4.7, undergoes temporal compression and spectral broadening due to interplay between the anomalous dispersion and nonlinearity. Eventually, the low-intensity spectral tail of the pump reaches the phase-matching point indicated with a red vertical-dashed line in Fig. 4.7, and conversion from the pump to this wavelength takes place. The phase-matching condition is obtained by Eq. 3.11. Figure 4.7 (c) shows the plot of the phase mismatch featuring a zero mismatch at 238 nm. We observe another peak that appears at 400 nm which originates from rapid variation in the dispersion near the resonant band [88]. Here, the wavelength is determined solely by, and highly sensitive to, the wall thickness of the dielectric cladding elements. Hence, the much broader emission band observed near 400 nm in the experiment can be attributed to variations in the thickness of the cladding element walls in SMA-HCF.

The shot-to-shot coherence of the output is quantified numerically and presented in Fig. 4.7 (d). It is obtained by running 50 simulations with random shot-noise added in the input pulse and calculating the degree of first-order coherence between them, such that 1 denotes complete preservation of the shot-to-shot coherence and 0 otherwise [107]. The entire output maintains high degree of coherence, meaning that the phase relation between the spectral components in the pump and UV band is well maintained.

In the subsequent experiment, we keep the pump energy at 125 nJ and record the spectrum while varying the argon pressure. The results are presented in Fig. 4.8. The UV band appears centered at 227 nm when the pressure is 35 bar. As the pressure is increased, the emission moves towards longer wavelength, arriving at 251 nm when the pressure is 45 bar. The red-shifting of the UV band is due mainly to the increased contribution of the denser argon on the dispersion that pushes the phase-matching point to longer wavelength. The range of wavelength tunability in this work is limited by, the coverage of our spectrometer in the short wavelength side, and the pressure handling capability of our gas chamber in the long-wavelength side. The latter can be extended further by using denser gas such as krypton or xenon. Again, we notice a similar spectral feature at 400 nm as observed in Fig. 4.6, which is caused by the band-edge effect. Its location is not affected by the pulse energy nor gas pressure as apparent in Figs. 4.6 and 4.8.

4.3 Summary

In this chapter, we demonstrate low-energy-threshold onset of the wavelength tunable deep-UV emission in SMA-HCF through dispersive wave generation. The SMA-HCF is fabricated by post-processing a nodeless tubular hollow-core fiber on a tapering rig. It confines light tightly into a small mode area allowing accumulation of nonlinear phase shift that is sufficient for the frequency conversion process with small pump pulse energy. The energy scaling down is achieved alongside the reduction in the fiber length requirement. This not only mitigates the issue of having high attenuation per unit length in SMA-HCF, but it is also advantageous for building a compact system. It opens a promising avenue for a compact wavelength-tunable UV frequency comb source driven directly by a femtosecond oscillator operating at a multi-megahertz repetition rate.

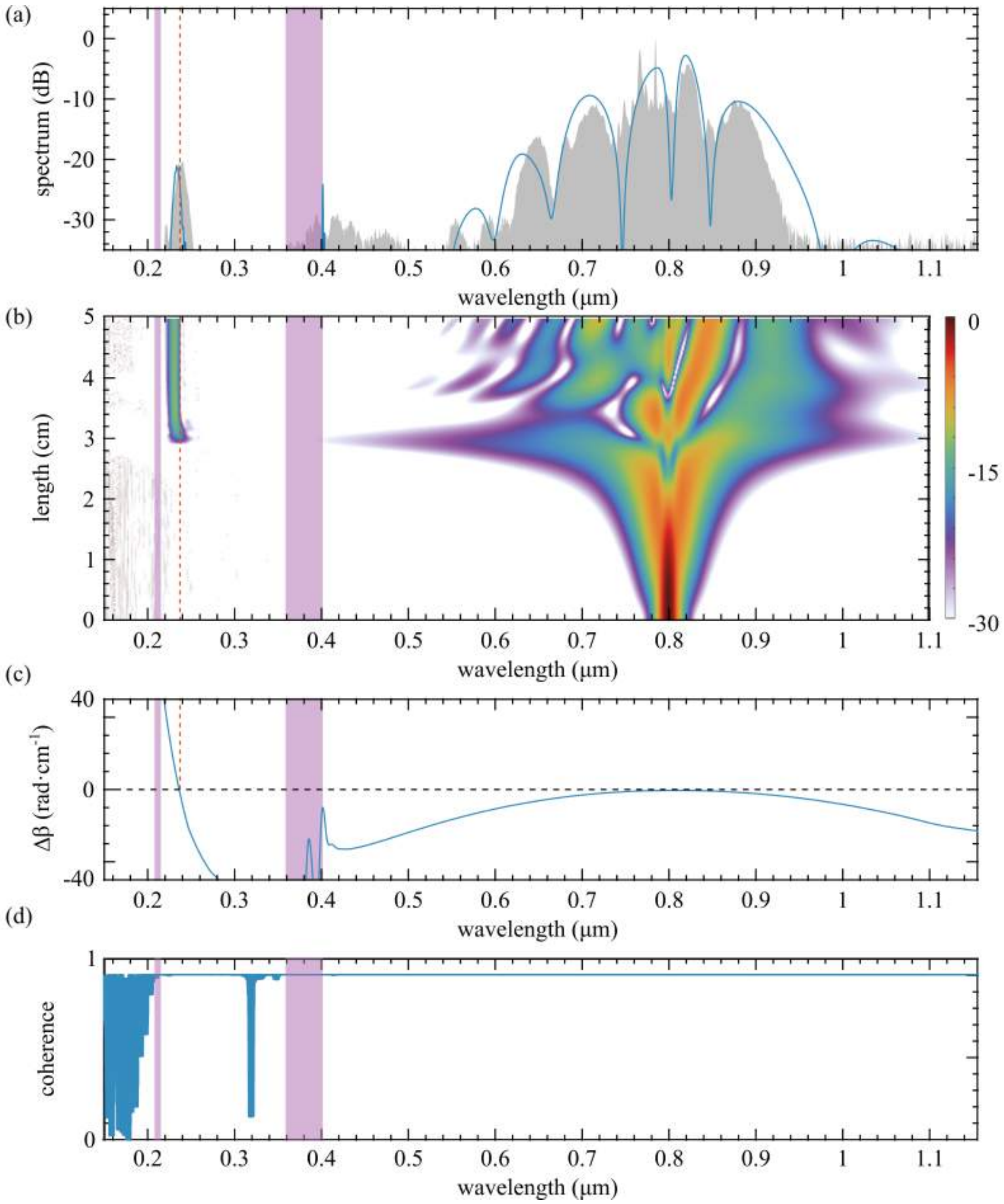

FIGURE 4.7: (a) Simulated spectral profile at the output of the 5 cm-long SMA-HCF for 150 muJ, 52 fs pump centered at 800 nm. The fiber is filled with argon at 40 bar. Measured spectrum for the identical condition is shown in gray shade. (b) Its spectral evolution along SMA-HCF. (c) Dispersive wave phase-matching diagram for 800 nm pump. The phase-matching point is indicated by a red vertical-dashed line. (d) The degree of first-order coherence of the output calculated based on 50 simulations with random shot-noise added in the pump. 1 denote complete preservation of shot-to-shot coherence and 0 otherwise. Purple shades are the high-loss regions of SMA-HCF.

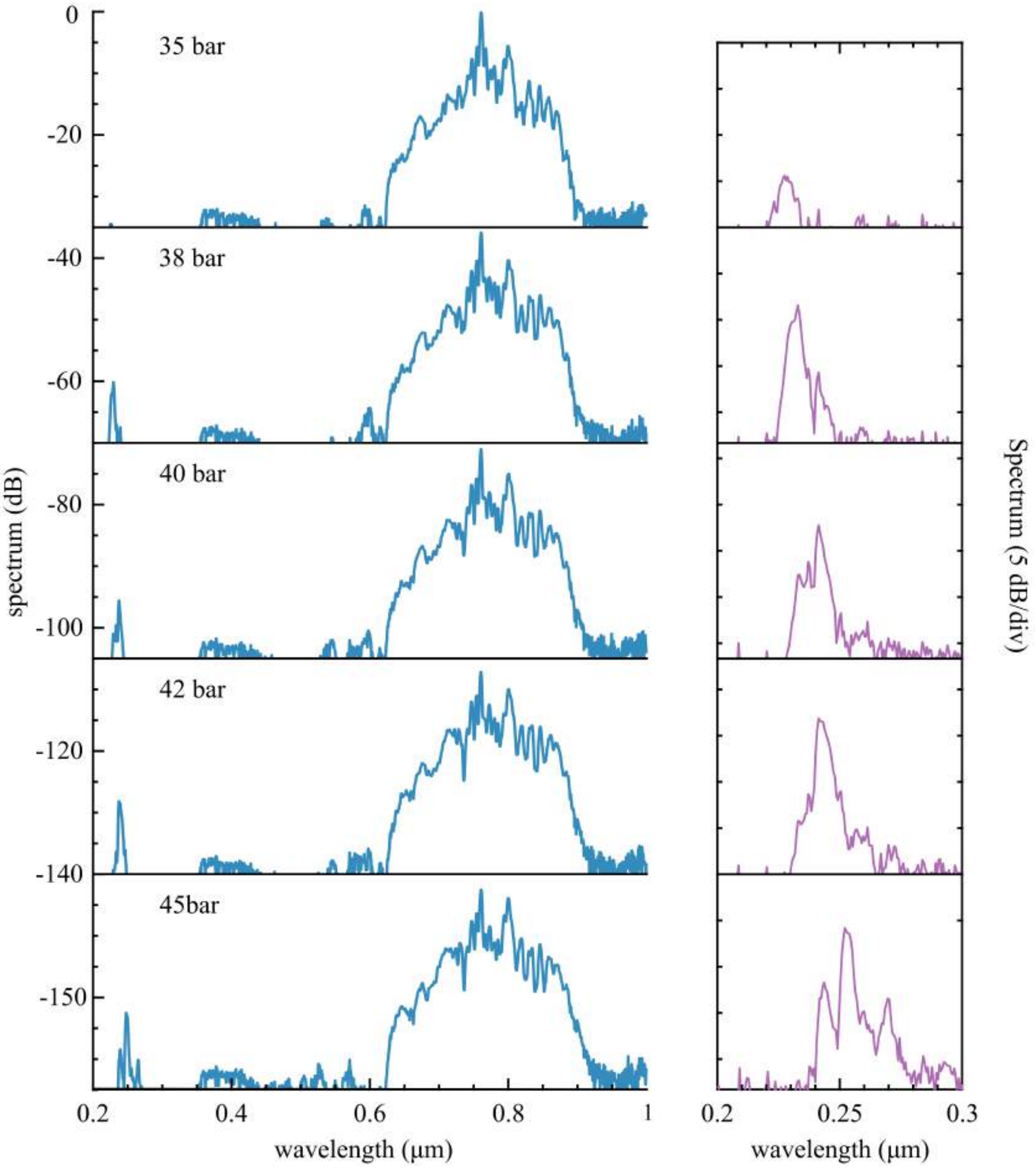

Figure 4.8: Spectra of the beam leaving the 5 cm-long SMA-HCF for different argon pressures when the observed output pulse energy is 100 nJ. This amounts to approximately 125 nJ pump. The entire spectra are presented in the left-hand-side panel and corresponding magnified UV parts are shown in the right-hand-side.

Chapter 5

Enhancement of Ultraviolet Generation in Gas-Filled HCF

In the low-pump-threshold UV generation experiment presented in Chapter 4, the achieved conversion efficiency to UV is only 2%. This chapter focuses on how to improve UV conversion efficiency in the gas-filled HCF system. Two factors are investigated here, self-steepening effect and resonant bands in the AR-HCF. For self-steepening effect, the first part outlines the soliton dynamics in the normalized nonlinear Schrödinger equation (NLSE) with different normalized self-steepening parameter, giving us the expectation of the frequency up-conversion efficiency on physic grounds. The numerical results illustrates the impact of self-steepening on UV conversion efficiency which can be both positive and negative. To implement the optimal self-steepening effect in UV generation experiment, the pump pulse of 50 fs in Chapter 4 should be compressed down to less than 20 fs, giving a conversion efficiency of 14%. Then, the influence of resonance bands of AR-HCFs on UV generation is discussed. The enhanced UV generation is shown experimentally by utilizing a wet-etched AR-HCF to decrease its core-wall thickness. This reduces the number of resonant bands in between pump and generated UV, providing more seeding energy to high-frequencies range. Moreover, the numerical results shows the generated UV quality is better maintained in the etched AR-HCF with high pumping energy.

5.1 Influence of Self-Steepening on UV Generation

5.1.1 Enhanced UV Conversion Efficiency by Optimizing Self-Steepening Effect

The influence of self-steepening (SS) effect can be best studied by isolating it in the normalized NSE according to Eq. 2.11

$$i\frac{\partial u}{\partial \xi}+\frac{1}{2}\frac{\partial^2 u}{\partial \tau^2}+|u|^2u=i\delta_3\frac{\partial^3 u}{\partial \tau^3}-is\frac{\partial}{\partial \tau}(|u|^2u) \tag{5.1}$$

where the Raman effect is neglected, the field amplitude $u(\xi,\tau)$ is normalized such that $u(0,\tau)=N\text{sech}(\tau)$, and other variables are defined as

$$\xi=\frac{z}{L_D},\ \tau=\frac{t-z/v_g}{T_0},\ \delta_3=\frac{\beta_3}{T_0},\ s=\frac{1}{w_0T_0}. \tag{5.2}$$

Here, T_0 is the pump pulse width, β_3 is the third-order dispersion (TOD), w_0 is the central pump frequency, δ_3 and s are the normalized TOD and s parameters respectively. It has been revealed that there is a minimum requirement of δ_3 for the onset of the detectable dispersive wave [108]. We assume that the detectable range is 40 dB lower than the peak of the output spectrum. In this section, we study numerically how the energy and conversion efficiency of the emitted DW vary with s parameter for a given δ_3, 0.12, which is slightly larger than the minimum value 0.11 for a second-order soliton. The case of second-order soliton is focused here, while higher-order solitons are discussed in the next section.

Figure. 5.1, 5.2, 5.3, and 5.4 presents the second-order soliton dynamics according to Eq. 5.1 with increasing normalized self-steepening parameter, s, from 0 to 0.55. Among these cases, the pulse initially gets broadened in spectral domain and compressed in temporal domain. After the pulse is completely compressed and fully broadened in spectrum, part of the energy is transferred from the main spectrum to the phase-matched frequency, emitting DW. The DW conversion efficiency plots, Fig. 5.1 (c), 5.2 (c), 5.3 (c), and 5.4 (c), present that the DW gains energy over a certain distance where the pulse remains enough broadening in spectrum.

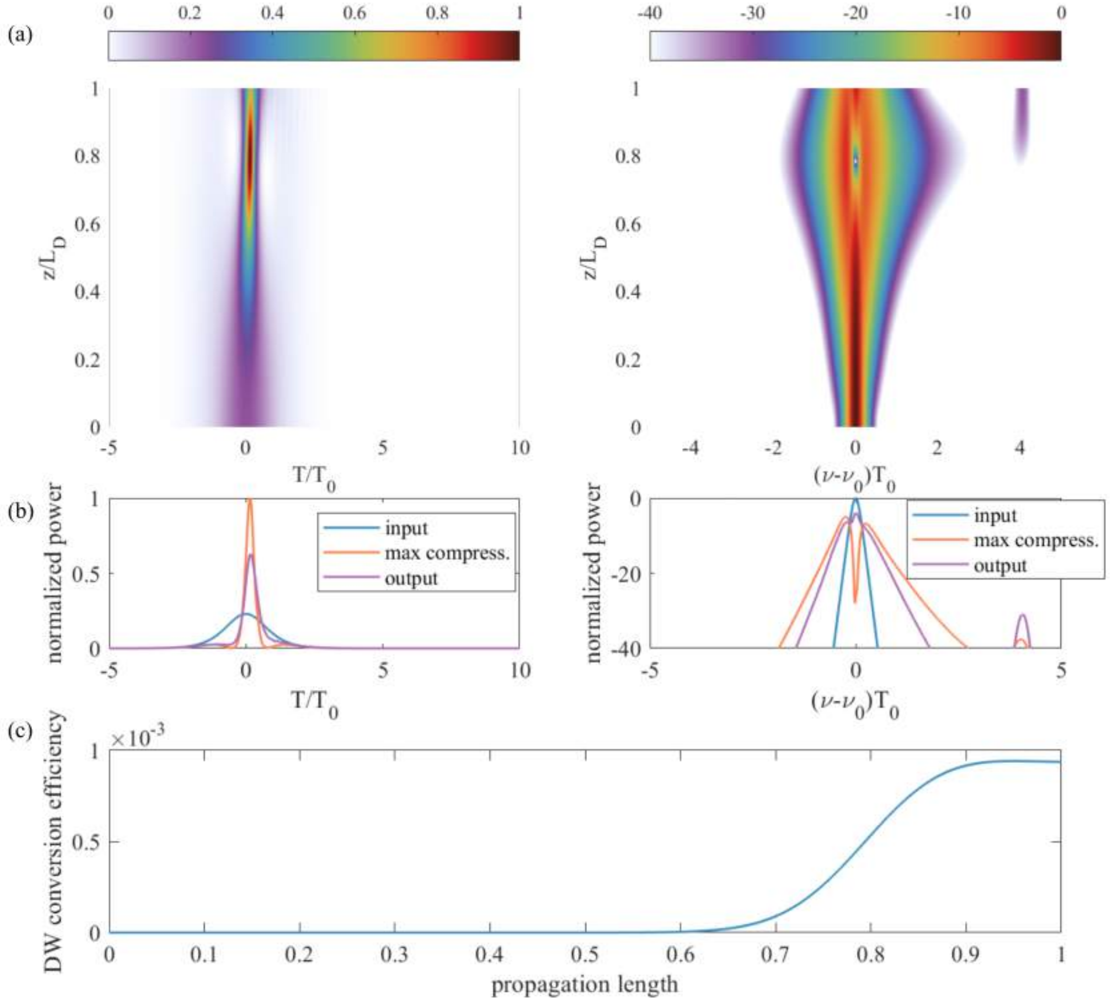

Figure 5.1: (a) The pulse evolution in temporal (left) and spectral (right) domain for a second-order soliton with δ_3 of 0.12 and s of 0. (b) The pulse shape in temporal (left) and pulse spectrum in spectral (right) domain at the input (blue), maximum compressed (red), and output (purple) position. (c) the DW conversion efficiency along the pulse propagation.

Then, the DW energy stays no change over the left distance (the loss is neglected here), which means the energy conversion process finishes. General speaking, the four DW generation processes with different s parameters all conform the above description. However, this DW emission process is somewhat different because of the asymmetric spectral broadening caused by self-steepening, and the resulting DW conversion efficiency is different.

As discussed in section 2.2.4.2, the self-steepening would cause the spectrum to broaden further into blue side. This is clearly observed in the spectrum at maximum compressed position, where the peak power in temporal domain is the highest along the propagation, in Fig. 5.2 (b), 5.3 (b), and 5.4 (b). It is worth noting that

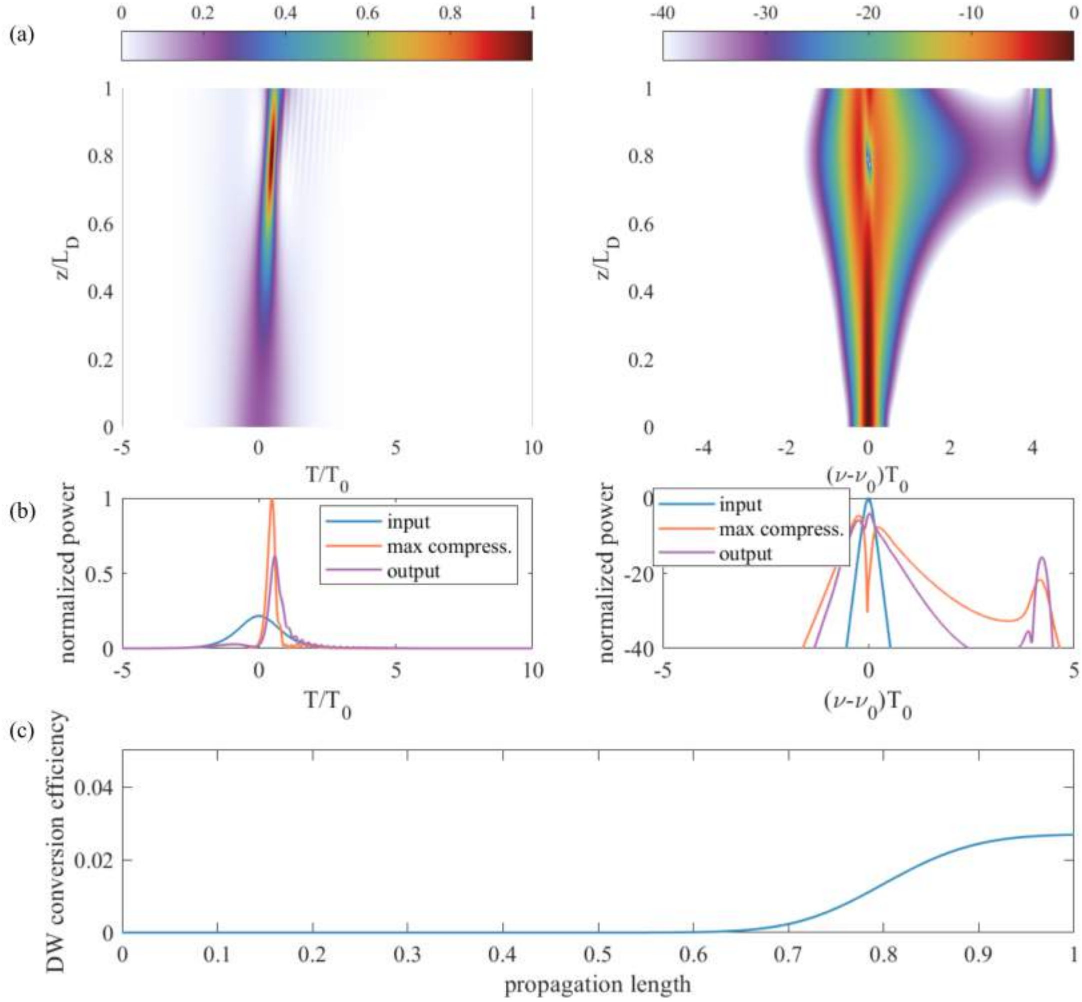

FIGURE 5.2: (a) The pulse evolution in temporal (left) and spectral (right) domain for a second-order soliton with δ_3 of 0.12 and s of 0.05. (b) The pulse shape in temporal (left) and pulse spectrum in spectral (right) domain at the input (blue), maximum compressed (red), and output (purple) position. (c) the DW conversion efficiency along the pulse propagation.

the broadening width and its power density into blue side increases first and then decreases with the increment of self-steepening. So as the DW conversion efficiency. Without the effect of self-steepening, the conversion efficiency into DW is less than 0.1%, which is enhanced to 2.7% and 21% when s parameter increases to 0.05 and 0.25, respectively. Then, a decrement of DW conversion efficiency can be observed, down to 10%, when s further increases to 0.55. It also can be seen that when the DW conversion efficiency is strongest, it is when the pulse broadening is most unbalanced, the most to blue side. That is to say, the spectral power density at the maximum compression stage is crucial to enhance the DW conversion efficiency. Along with the more to spectral power density of higher frequencies (blue

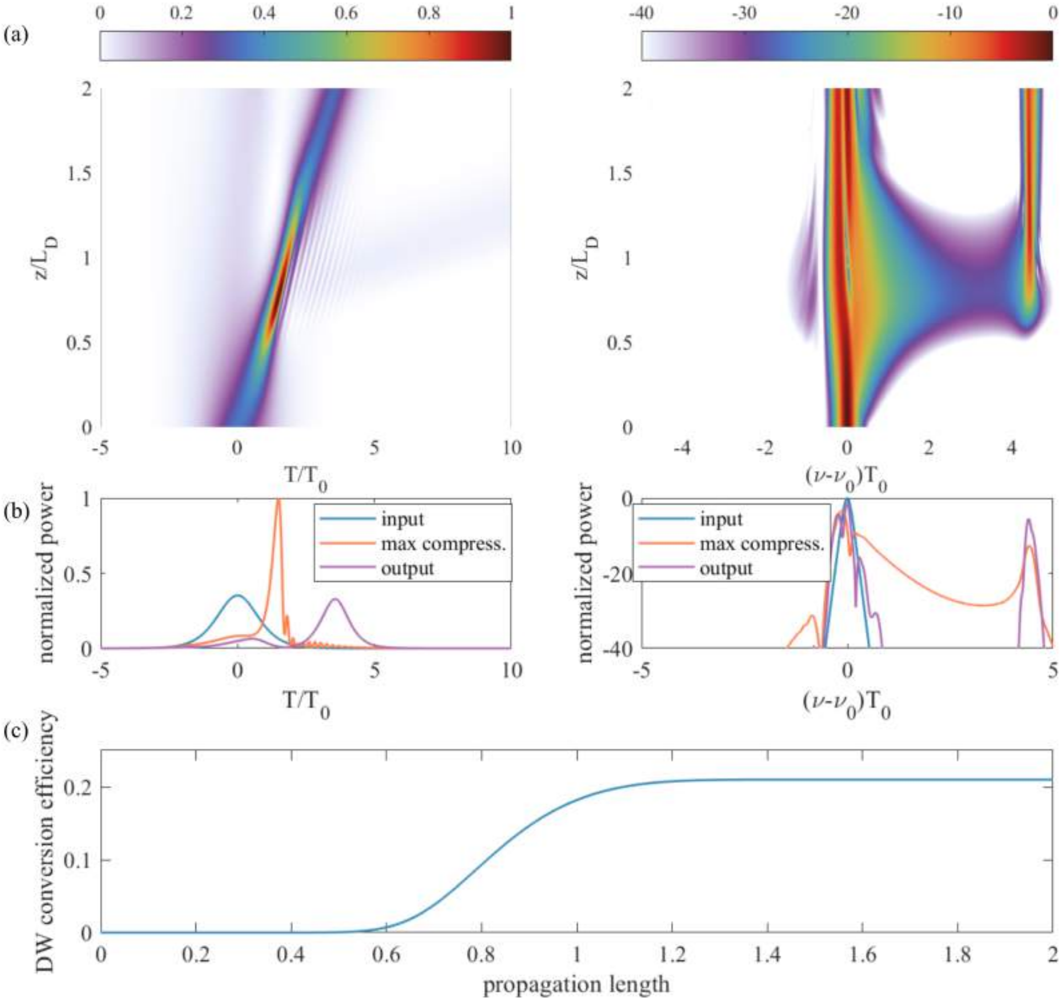

FIGURE 5.3: (a) The pulse evolution in temporal (left) and spectral (right) domain for a second-order soliton with δ_3 of 0.12 and s of 0.25. (b) The pulse shape in temporal (left) and pulse spectrum in spectral (right) domain at the input (blue), maximum compressed (red), and output (purple) position. (c) the DW conversion efficiency along the pulse propagation.

side), the interaction length at which the energy transfer takes place is longer. For the soliton dynamic without self-steepening, once the pulse reaches its maximum compression, it broadens soon in temporal domain, causing the length ξ of energy conversion from pump to DW is only 0.3, which can be identified from the DW conversion efficiency increasing process, as well as the pulse evolution, as shown in 5.2 (a) (c). However, with a increasing self-steepening effect, the pulse can keep it compressed narrow pulse width for a long distance, so does the energy conversion process, which is extended to over 1.5, when the s is increased to 0.55.

Figure 5.5 (a) shows the DW conversion efficiency versus s parameter. It shows that there is a optimal choice of s parameter to get a highest DW conversion efficiency,

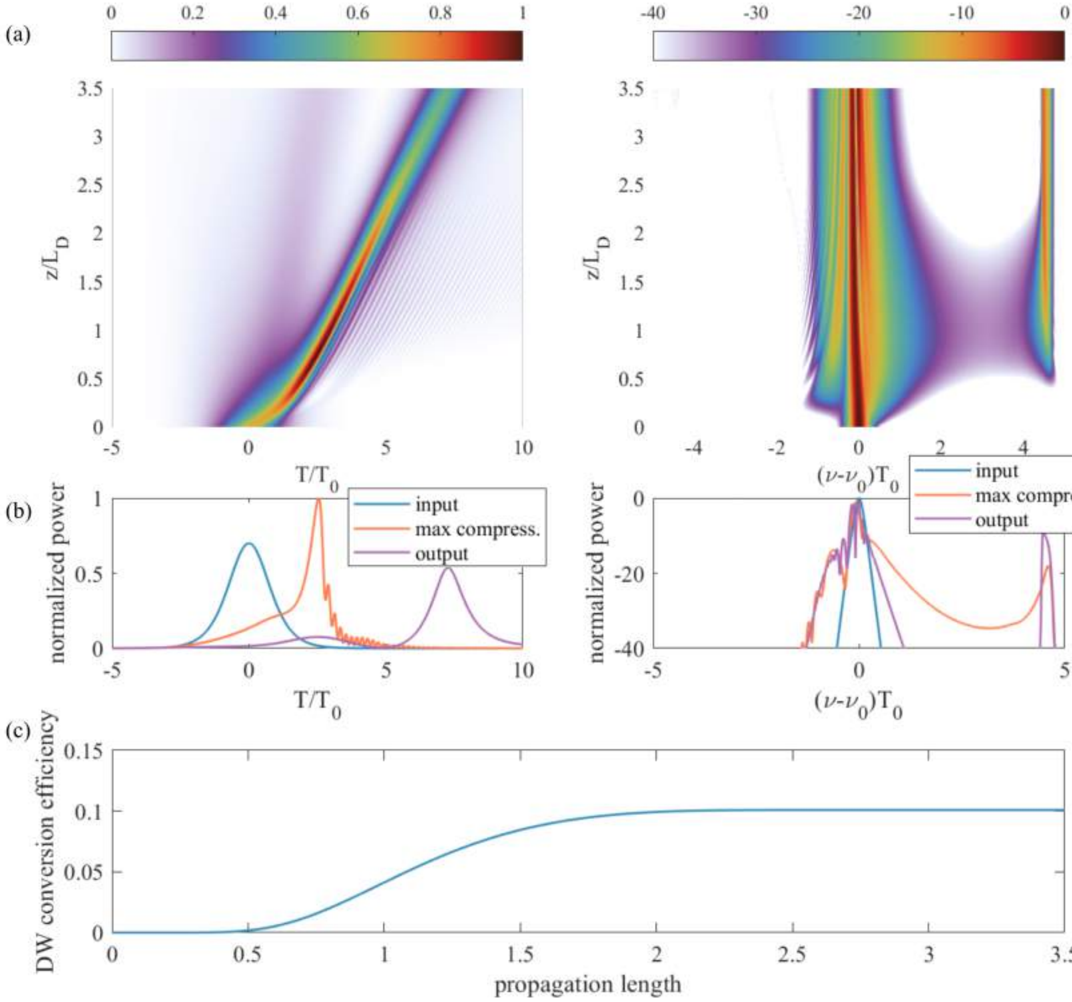

FIGURE 5.4: (a) The pulse evolution in temporal (left) and spectral (right) domain for a second-order soliton with δ_3 of 0.12 and s of 0.55. (b) The pulse shape in temporal (left) and pulse spectrum in spectral (right) domain at the input (blue), maximum compressed (red), and output (purple) position. (c) the DW conversion efficiency along the pulse propagation.

which can be enhanced drastically from less than 0.1% to over 20%. Whereas Fig. 5.5 (b) illustrates that the interaction length of energy conversion, which is defined as the distance at which DW conversion efficiency increases from its maximum value of $1/e$ to 1-$1/e$, generally keeps going up with increasing s.

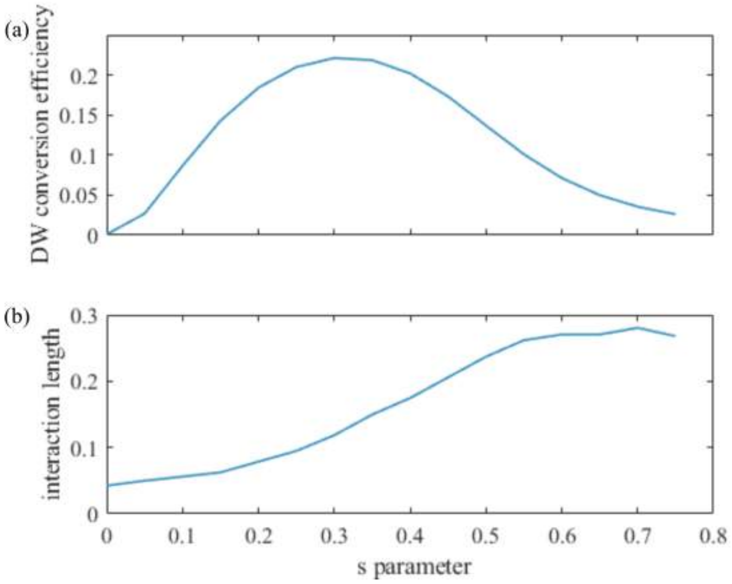

Figure 5.5: (a) The DW conversion efficiency and (b) interaction length where energy conversion happens with increasing s parameter.

5.1.2 Dependence of UV Generation on Self-Steepening for Different Soliton Orders

Now let's look at the higher-order soliton dynamics with different self-steepening parameters. For a fourth-order soliton, the δ_3 is set to be 0.05, the minimum requirement for a detectable DW emission in 40 dB spectral range, while this number is decreased 0.03 for a six-order soliton. The trend of DW conversion efficiency is similar to that of a second-order soliton, increasing first then decreasing as s parameter keeps rising. The achieved highest DW conversion efficiency is bigger with a higher-order soliton. For a second-order soliton, the highest DW efficiency is 20%, is raised to 25% and 28% for a fourth- and sixth-order soliton respectively.

5.1.3 Enhance UV Generation by Pump Pulse Compression

According to Eq. 5.2, the normalized s parameter is defined as $\frac{1}{w_0 T_0}$. To apply the normalized NSE into the denormalized gas-filled HCF system, one can pump with shorter pulse width to increase self-steepening effect in the UV generation. Now

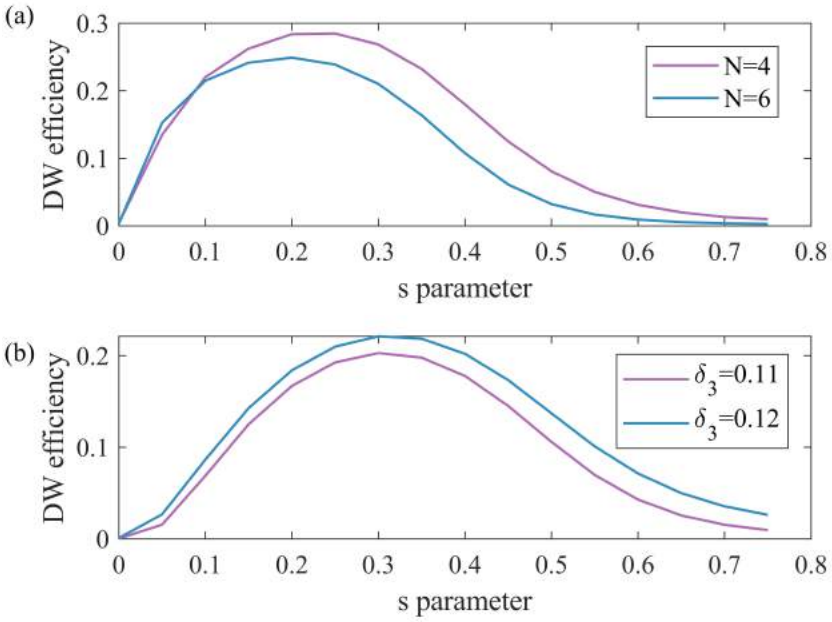

FIGURE 5.6: (a) The DW conversion efficiency versus s parameter for fourth-order and sixth-order soliton. (b)The DW conversion efficiency versus s parameter for a second-order soliton when δ_3 is 0.11 and 0.12.

we study numerically in this section how the UV emission would be enhanced with shorter pump pulse width in the gas-filled HCF system.

In the Section , a deep UV is generated via DW emission in the AR-HCF with a core diameter of 10.6 μm and pumped with 50 fs pulses. The conversion efficiency achieved to deep UV is only 2%. To increase this conversion efficiency by enhancing the self-steepening effect, the soliton dynamics with different pump pulse is studied here. By adjusting the pump energy, the soliton order is kept constant, and the argon pressure is also maintained so that the DW generated is at the same frequency. The propagation length is set to be 1.3 times the fission length, ensuring a full development in DW. The soliton dynamics of pump with different pulse widths in temporal and spectral domain, as well as its pulse shape and spectral components at maximum compression and output are shown in the fig. 5.7, 5.8, 5.9, 5.10. The corresponding s parameter when the pulse width is compressed from 50 to 20 fs, in a 10 fs-step, is increased from 0.09 to 0.025. As expected, the self-steepening effect makes the pulse sharper in the trailing edge with shorter pulse width, resulting in a wider broaden and a larger energy component of the spectrum towards higher frequencies, which can be seen from the pulse shape and spectrum at the pulse maximum compression. Moreover, the energy conversion happens over a longer interaction distance for shorter pump width, which is inline with the results in normalized NSE. The conversion efficiency achieved for the 50, 40, 30, 20 fs are 1%, 4.2%, 8.5%, and 10.5% respectively with outstanding DW quality. An intriguing observation is that mild photonionization happens in the case of 20 fs pump width, causing 10% of the energy is lost. Even then, the conversion efficiency improved substantially. If one further increases the s parameter, say 0.55, the corresponding pulse width is only 5 fs, which is hard to achieve experimentally. Besides, to maintain the same soliton-order, the pulse energy is increased a lot with shorter pulse width, leading to a complex soliton dynamics and DW is not distinguishable. It is worth noting that compressing pump pulse can also increase the normalized δ_3, which also has a positive impact on DW generation to a certain extent [108].

The energy scaling capability in different core size of AR-HCFs is discussed earlier in Chapter 4, Fig. 4.1 - for a given choice of zero-dispersion wavelength λ_0 and soliton order N and same pump pulse width, the energy of emitted UV via DW generation can be simply scaled up to tens of microjoules or down to several nanojoules by confining the light into a HCF with a big or small core size, whereas the conversion efficiency from pump to UV keeps the same regardless of the energy. We now focus on the soliton dynamics and DW conversion efficiency in the AR-HCF of different core size and pump pulse. Here the soliton order N, and ZDW are kept the same as before (N=5, ZDW=508 nm), but with different pump pulses. Prorogation length is still 1.2 times the fission length.

Figure 5.11 shows the soliton evolution in the AR-HCF with a core diameter of 30 μm and pumped with 30 fs pulses. The corresponding s parameter is 0.16. The generated DW energy is 0.13 μJ and conversion efficiency is 8.8%. These two are increased to 0.85 μJ and 13.6% in the AR-HCF with a core diameter of 50 μm and pumped with 20 fs pulses. An interesting observation is that when we compare Fig. 5.10 with the core diameter of 10.6 μm) and Fig. 5.12 with the core diameter of 50 μm), we find that their δ_3 and s are the same, 0.14 and 0.24 respectively, but the latter emitted the DW with a higher conversion efficiency, 14%, than the former, 10.5%. A possible explanation is that the self-steepening parameter s should be corrected with effective mode area [109], a bigger effective mode area resulting a higher self-steepening effect.

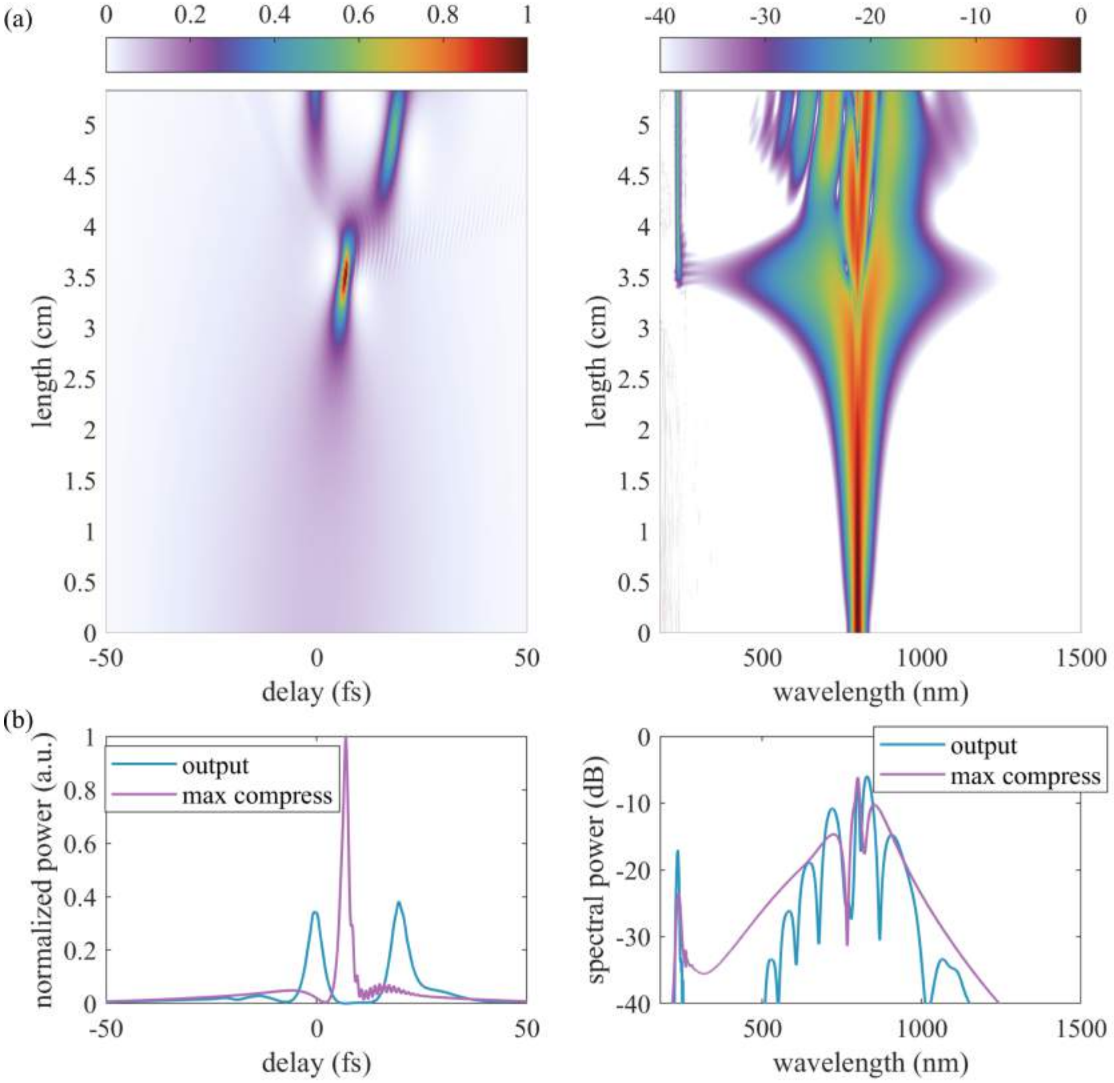

Figure 5.7: (a) The pulse evolution (N=5) in temporal (left) and spectral (right) domain in the AR-HCF with a core diameter of 10.6 μm and pumped with 50 fs pulses (s=0.09). (b) The pulse shape in temporal (left) and spectral (right) at the maximum compression and output of the AR-HCF.

5.2 Influence of Resonant Bands on UV Generation

One of the main drawbacks of using AR-HCF in the UV generation is the presence of antiresonant bands in the vicinity of the UV phase-matching point that often leads to a poor conversion efficiency [88]. An enhanced up-conversion can be achieved in a simple dielectric capillary that lacks the resonant bands or in

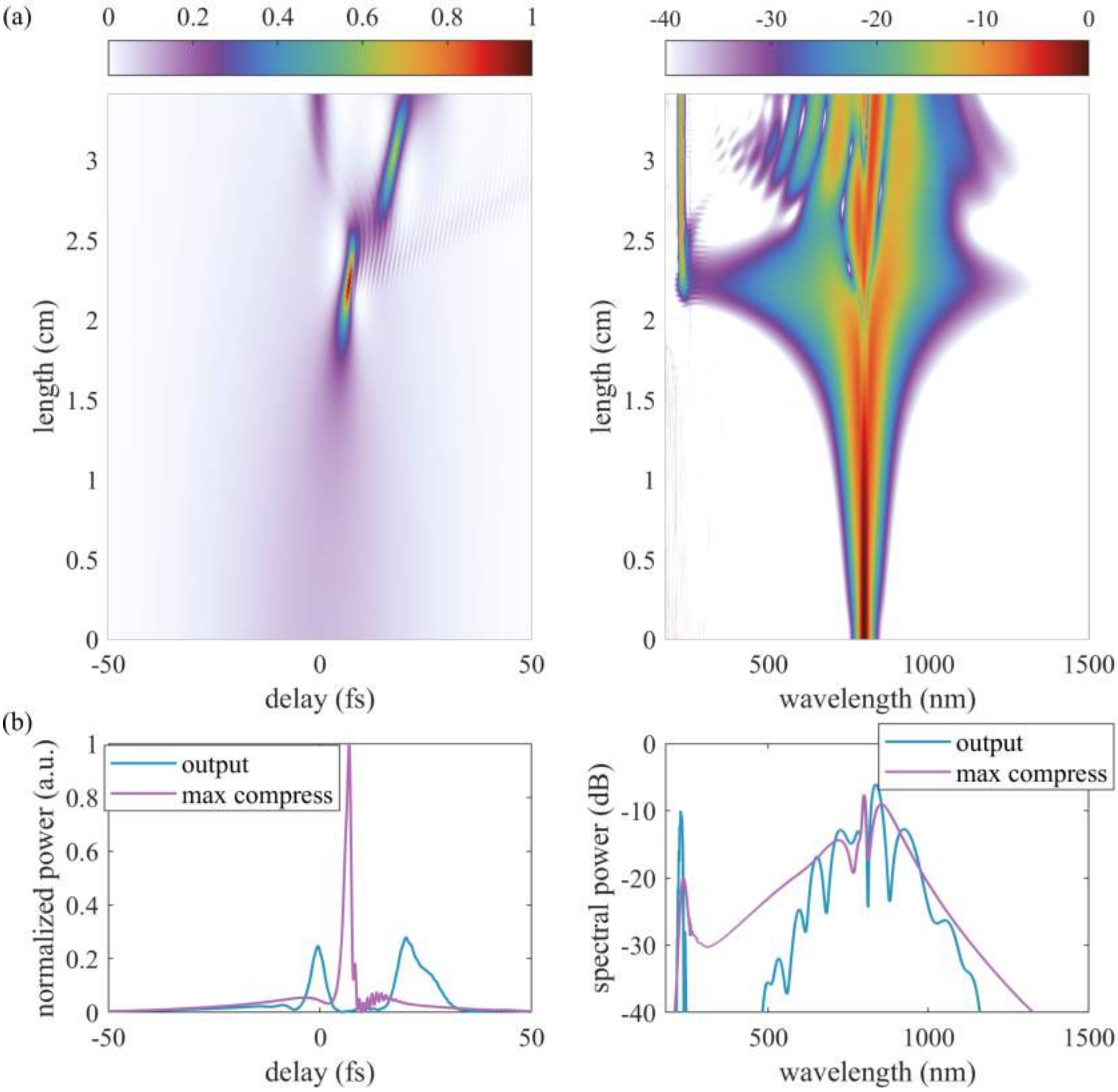

Figure 5.8: (a) The pulse evolution (N=5) in temporal (left) and spectral (right) domain in the AR-HCF with a core diameter of 10.6 μm and pumped with 40 fs pulses (s=0.12). (b) The pulse shape in temporal (left) and spectral (right) at the maximum compression and output of the AR-HCF.

a Kagome fiber with ultrathin core-wall thickness which can be as thin as several tens of manometers, but the former is at the cost of requiring a much-higher pump pulse energy [49] while the latter structure is complicated [110]. Therefore, gaining a comprehensive insight of how the resonant bands influence the nonlinear frequency up-conversion in gas-filled AR-HCF is vital for building a compact and efficient UV laser source.

In this section, we investigate the influence of resonant bands in ultraviolet generation in gas-filled antiresonant hollow-core fibers. For simplicity, the Marcatili DW

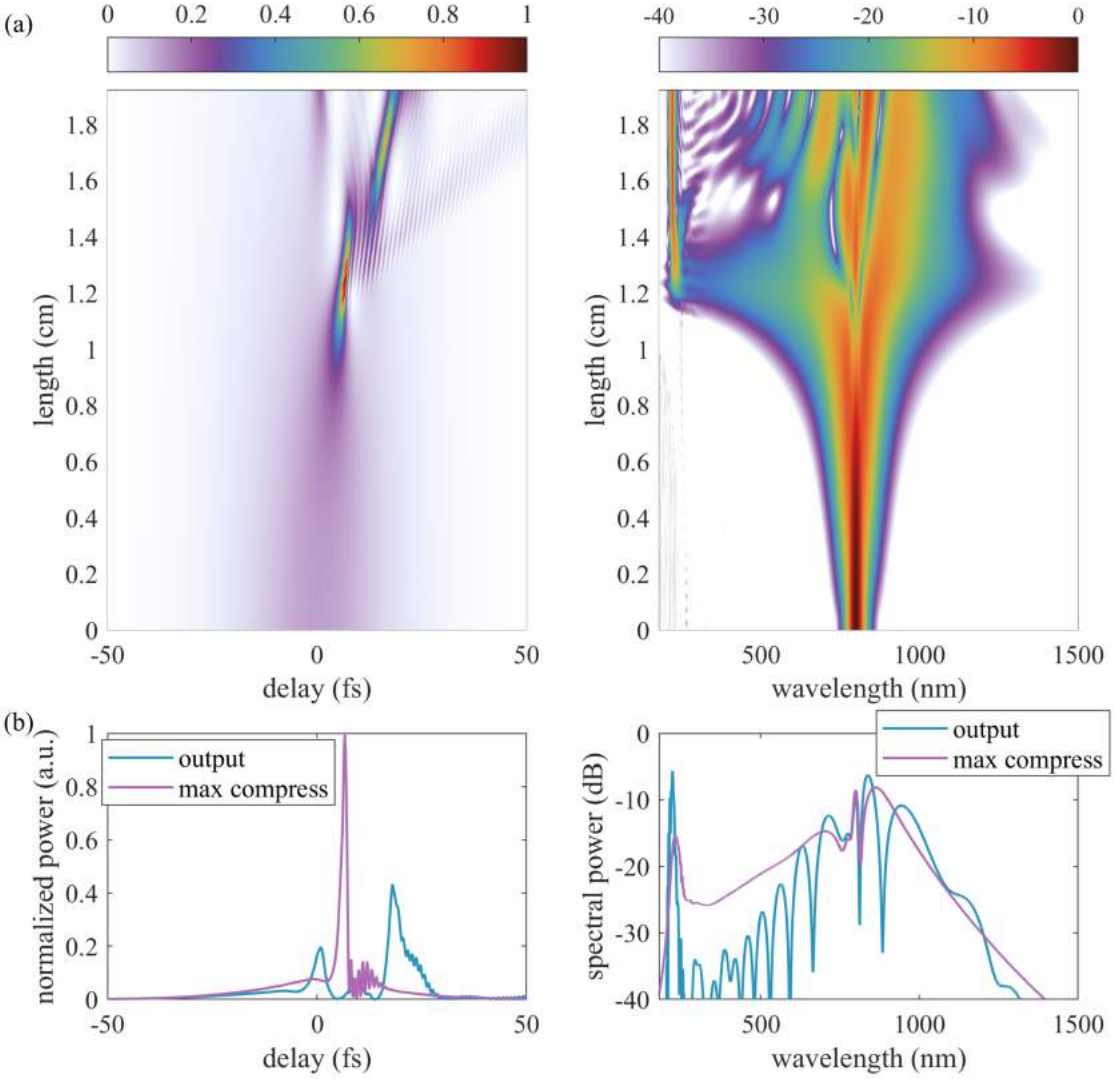

FIGURE 5.9: (a) The pulse evolution (N=5) in temporal (left) and spectral (right) domain in the AR-HCF with a core diameter of 10.6 μm and pumped with 30 fs pulses (s=0.17). (b) The pulse shape in temporal (left) and spectral (right) at the maximum compression and output of the AR-HCF.

in this section refers to the DW generated at phase-matching point in the Marcatili model while the band-edge DW refers to the phase-matched one emitted in the red-edge of resonance band thanks to the dramatically varied dispersion at the edge of resonance band. Moreover, wet etching technique is utilized to make the core-wall thickness thinner to reduce the effect of resonance bands in UV generation.

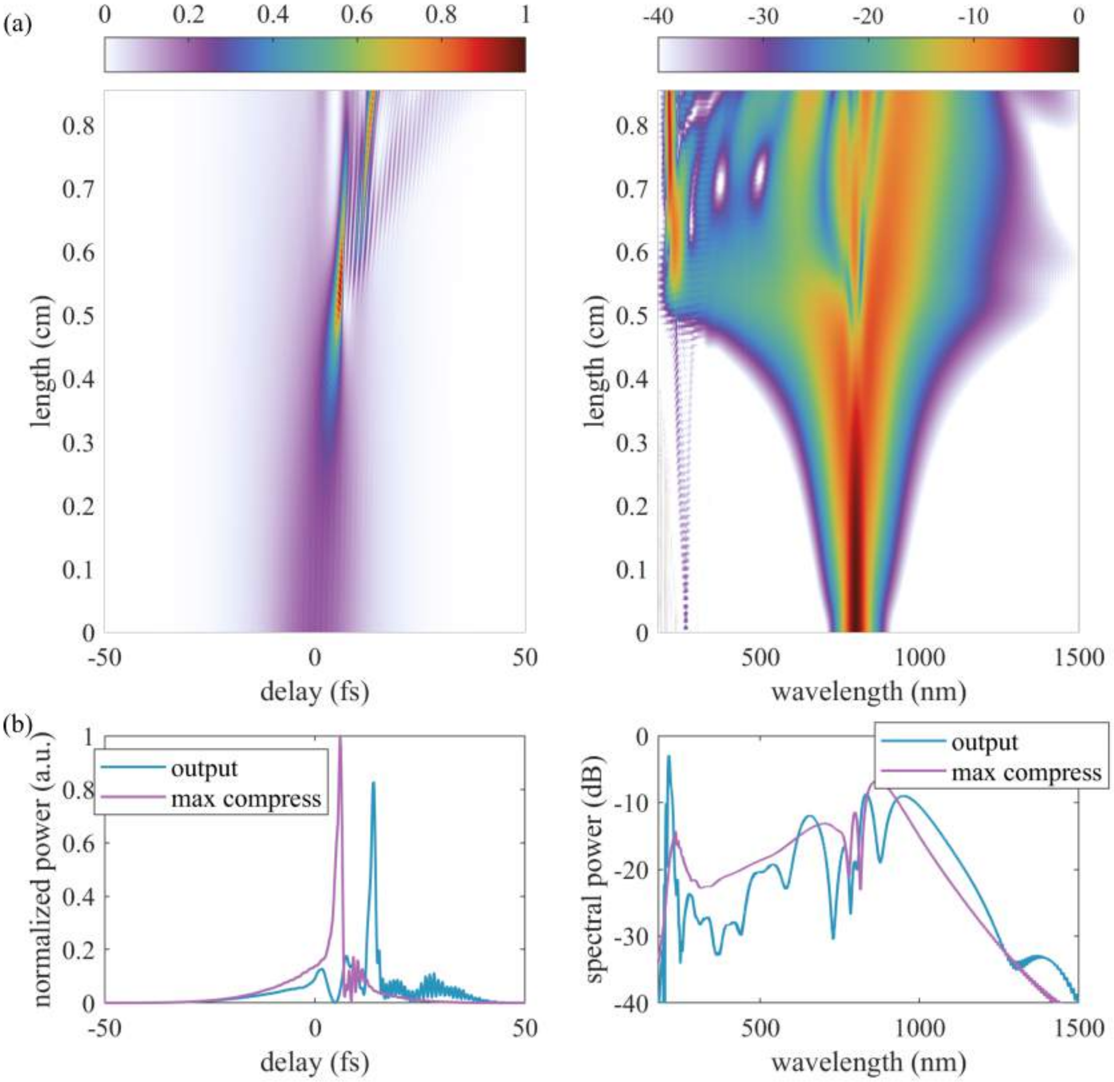

FIGURE 5.10: (a) The pulse evolution (N=5) in temporal (left) and spectral (right) domain in the AR-HCF with a core diameter of 10.6 μm and pumped with 20 fs pulses (s=0.25). (b) The pulse shape in temporal (left) and spectral (right) at the maximum compression and output of the AR-HCF.

5.2.1 Generating UV in the Vicinity of Resonant Bands

Figure. 5.13 represents the measured spectra at the output of a 15 cm-long AR-HCF, with a core diameter in 29 μm and cladding element wall thickness in 470 nm. The fiber exhibits the first three high-loss bands in the regions 370 THz (810 nm), 580-640 THz (470-520 nm), and 850-920 THz (325-350 nm), as shown in Fig. 5.13 (a) which is the transmission spectrum obtained by a xenon lamp. In the following experiments of generating UV, the argon pressure and the pump energies are tuned to put the UV phase-matching point between the third and fourth resonant bands.

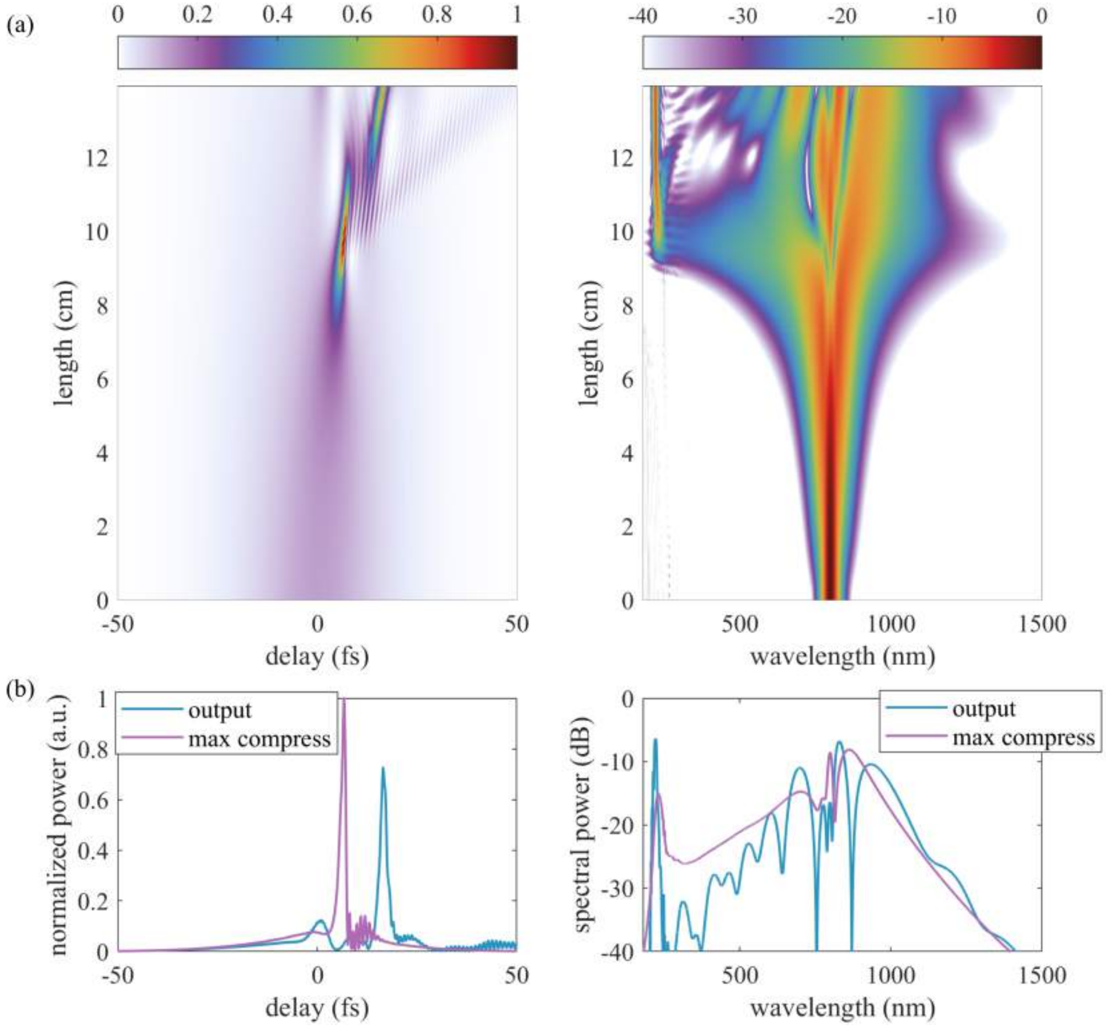

FIGURE 5.11: (a) The pulse evolution (N=5) in temporal (left) and spectral (right) domain in the AR-HCF with a core diameter of 30 μm and pumped with 30 fs pulses (s=0.16). N=5, ZDW=508 nm. (b) The pulse shape in temporal (left) and spectral (right) at the maximum compression and output of the AR-HCF.

Figure 5.13 (b) presents the measured spectra through an integrating sphere at the output of the AR-HCF filled with 10 bar argon pumped by a Ti:sapphire laser generating 45 fs pulses. The pump pulse energies launched into the gas chamber is increased from the top to bottom in Fig. 5.13. Please note that the launched energy into the gas chamber is not the energy pumped into AR-HCF.

At first, the energy launched into the gas chamber is 1.17 μJ while the output energy is 0.61 μJ, generating the Marcatili DW at 283 nm, along with two band-edge DW at 520 nm and 260 nm, locating at the red side of second and fourth resonance band respectively. After that, the launching energy is increased to 3.27 μJ, while the output energy shows only small amount of increment, to 0.8 μJ, corresponding

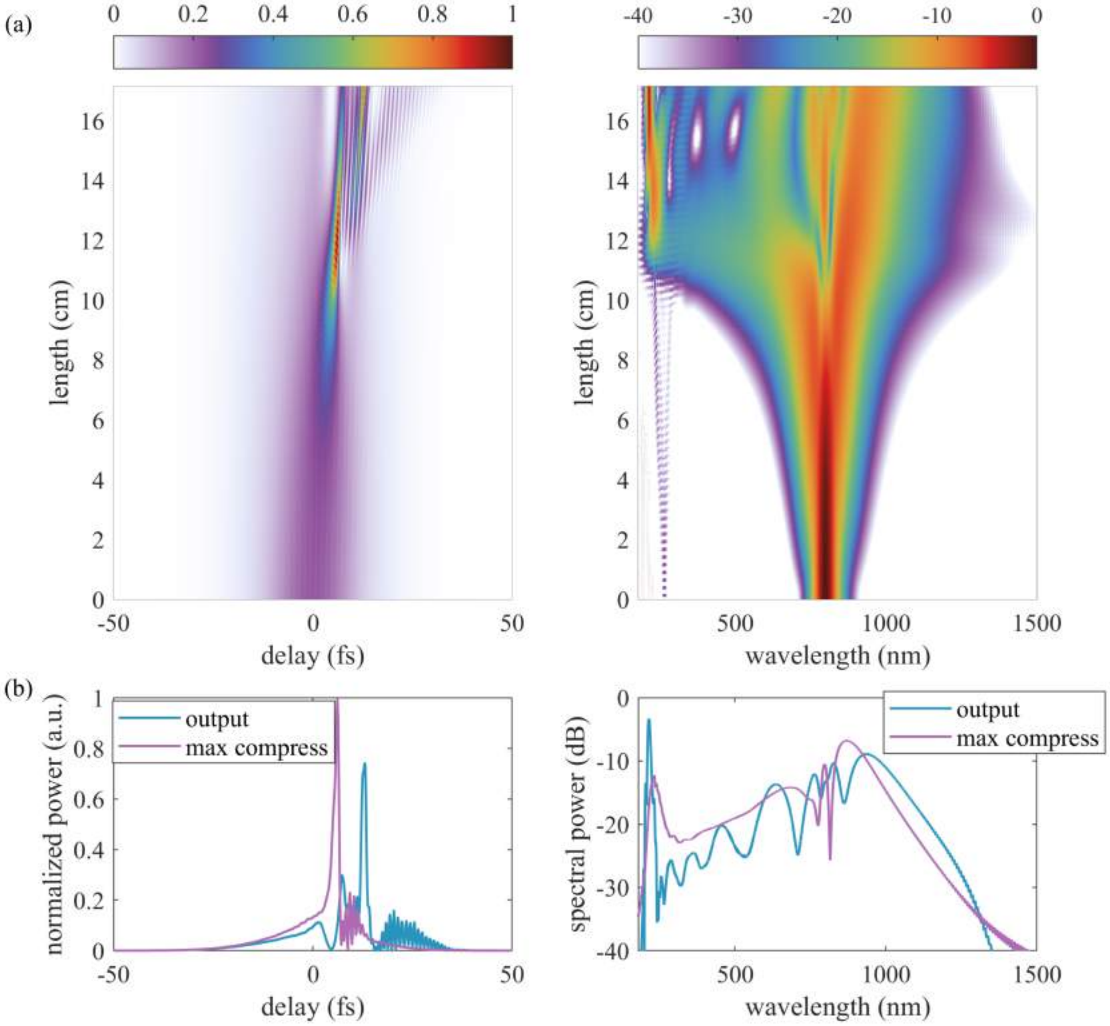

FIGURE 5.12: (a) The pulse evolution (N=5) in temporal (left) and spectral (right) domain in the AR-HCF with a core diameter of 50 μm and pumped with 20 fs pulses (s=0.24). N=5, ZDW=508 nm. (b) The pulse shape in temporal (left) and spectral (right) at the maximum compression and output of the AR-HCF.

to the coupling efficiency dropped from 52% to 24%. This is due to the ionized beam at the focused point is heavily deformed, further reduced the proportion of energy coupled into the fiber. The third resonance band induced band-edge DW at 360 nm is observed in this output spectrum. The reason that the fourth resonant band-edge DW, which is further away from pump, is emitted before the third resonant band-edge DW, is because the position of Marcatili DW is closer to the fourth one, giving it the seed in advance. Then, with the energy coupled into fiber is increased, an extra band-edge DW is emitted. Next, the launching energy is further increased to 3.9 μJ. In this output spectra, a stronger fourth resonant band-edge DW is observed, which can be attribute to the blue-shfted Marcatili

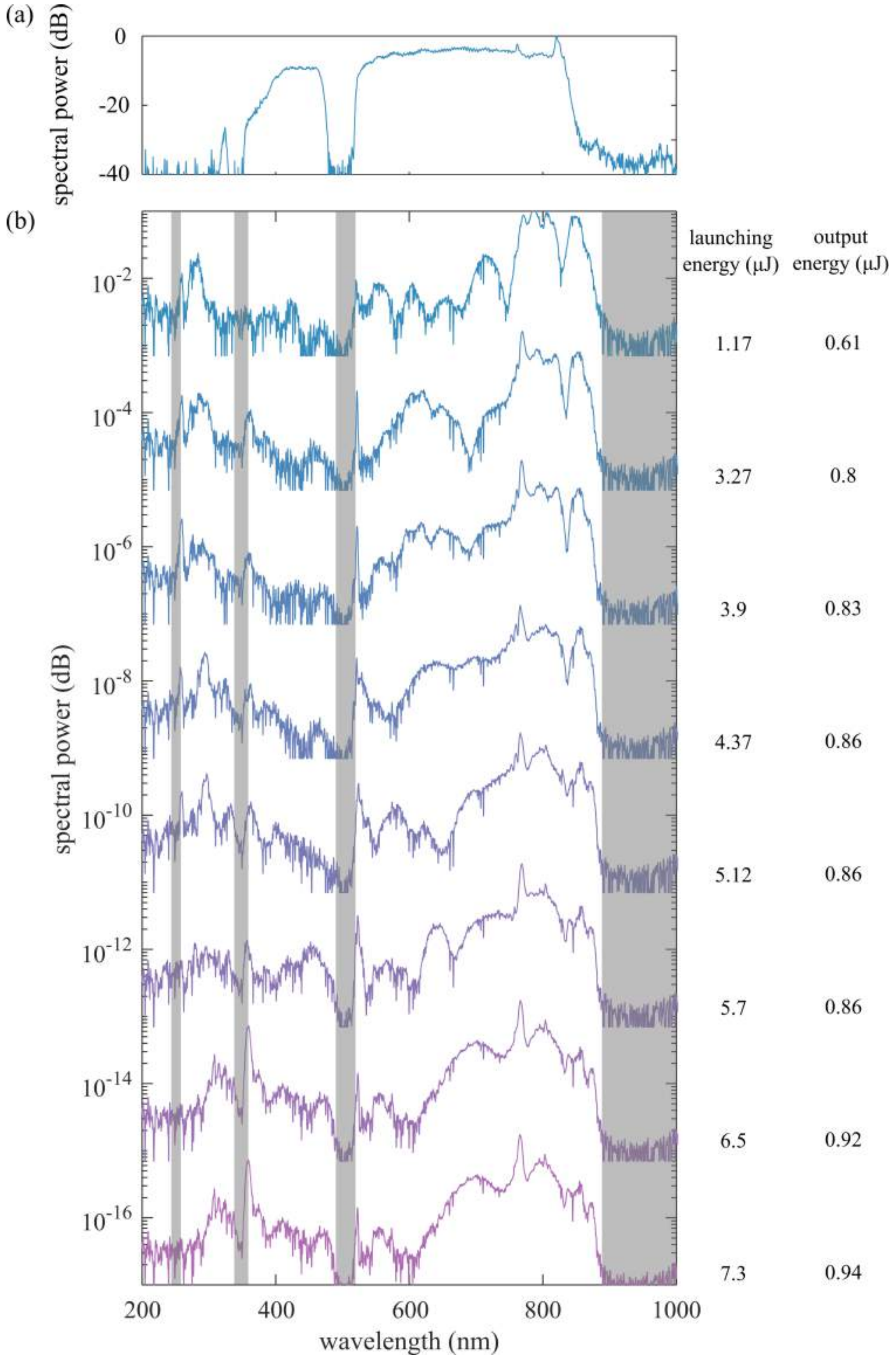

Figure 5.13: (a) The transmission spectrum of the AR-HCF recorded with a xenon lamp. (b) Measured spectra through an integrating sphere at the output of the 15 cm-long AR-HCF pressurized with 10 bar argon. The energy launched into the gas chamber is increased from the top, 1.17 μJ, to the bottom, 7.3 μJ while the output energy is measured at the output of the gas chamber. The shaded areas represent the high-loss resonance bands dictated from the cladding element thickness.

DW in stronger input energy, according to Eq. 2.14 and 2.15.

In the following experiments, the Marcatili DW shows a red-shift from 283 nm at beginning to 300 nm when the launching energy is increased to 4.37 μJ or even higher. That is because the second round of ionization happens at the maximum pulse compression position [111]. Put it simply, the pulse initially experienced temporal compression and spectral broadening due to the combined effects of SPM and anomalous dispersion, and it can ionize the gas inside the AR-HCF when the intensity of the compressed pulse is strong enough, causing a red-shift Marcatili DW [78].

As for the band-edge DWs, we can see the beating trend among two band-edge DWs from the experimental results. The fourth band-edge emits at first and gets stronger when the launching energy is higher. However, when the launching energy keeps increasing, the forth band-edge DW becomes weaker whereas the third band-edge DW is stronger and stronger. That is related to the position of shifting Marcatili DW effected by pump energy and photonionization. The band-edge DW closer to the Marcatili DW always gets more seeding and more energy converted from the pump. At the same time, it drags the energy away from the pump to desired Marcatili DW.

The conversion efficiency of the generated Marcatili and band-edge DWs, which is defined as the ratio of the energy of each DW to it in the total spectral band, is shown in Fig. 5.14. From which, we can observe that increasing pump energy does not help to increase the conversion efficiency to the desired Marcatili DW. Meanwhile, the spectral shape of the Marcatili DW is heavily deformed with increasing input energy, showing a broadening spectral shape and multiple peaks. However, that can be due to more than one round of temporal compression and Marcatili DW generating happens, offering multiple phase-matching positions.

5.2.2 Simulation Results about the Influence of Resonant Bands

In the experiment, the real amount energy coupled into the AR-HCF can not be precisely controlled, neither the rounds of pulse compression and Marcatili DW generation, which makes the comparison experiments meaningless. In order to

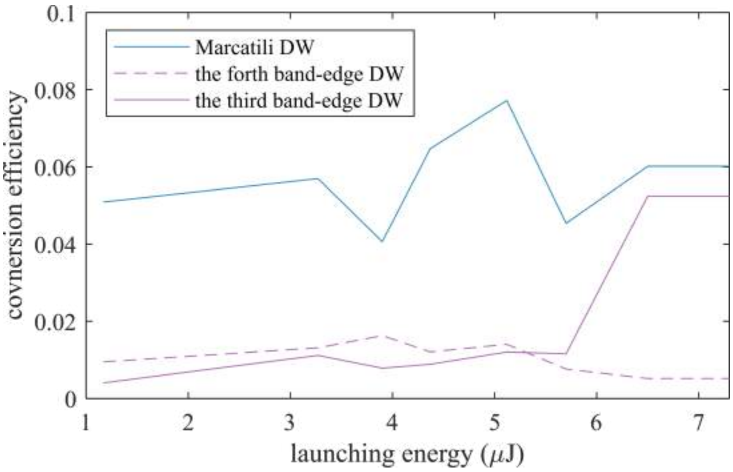

Figure 5.14: The conversion efficiency of the Marcatili and band-edge DWs in Fig. 5.13.

avoid the influence of all these factors, we carry out a numerical investigation to have a better understanding of the influence of nearby resonant bands on the frequency up-conversion process. We simulate the UV generation process in argon-filled AR-HCFs with the same fiber cross-sectional dimensions, the core diameter is 29 μm, but with two different cladding element wall thicknesses, i.e., 500 nm and 74 nm. The former places the second and third resonant bands in 560–600 and 820–860 THz, and we set the pump energy and argon pressure that situate the UV phase-matching in the transmission band between these two high-loss regions. On the other hand, the thin wall in the latter pushes the first resonance to 1500 THz, moving it completely out of the spectral range of our interest. For a meaningful comparison, we adjust the pump energy and gas pressure in the thinner wall fiber such that the soliton number and UV phase-matching wavelength are kept the same as in its counterpart [57]. The length of the fiber in the simulation is fixed at 1.2 times the fission length of the given soliton number to ensure the dispersive wave which onsets around the fission length is fully developed.

The loss and refractive index data calculated by FEM method and their fitting results for both 500 nm and 74 nm are presented in Figs.5.15 (a)(b), and 5.16 (a)(b) respectively. In Figs.5.15 (b) and 5.16 (b), the refractive indexes calculated for 500 and 74 nm by MS model also are presented. From which, we could see that the refractive index suffers certain degree of fluctuations in the resonance bands for the 500 nm-thickness case, which is not reflected in the MS model. In addition to this, the other parts of the two results are in good agreement. On the other hand, the thin 74 nm-wall pushes the resonances away outside the frequency range shown.

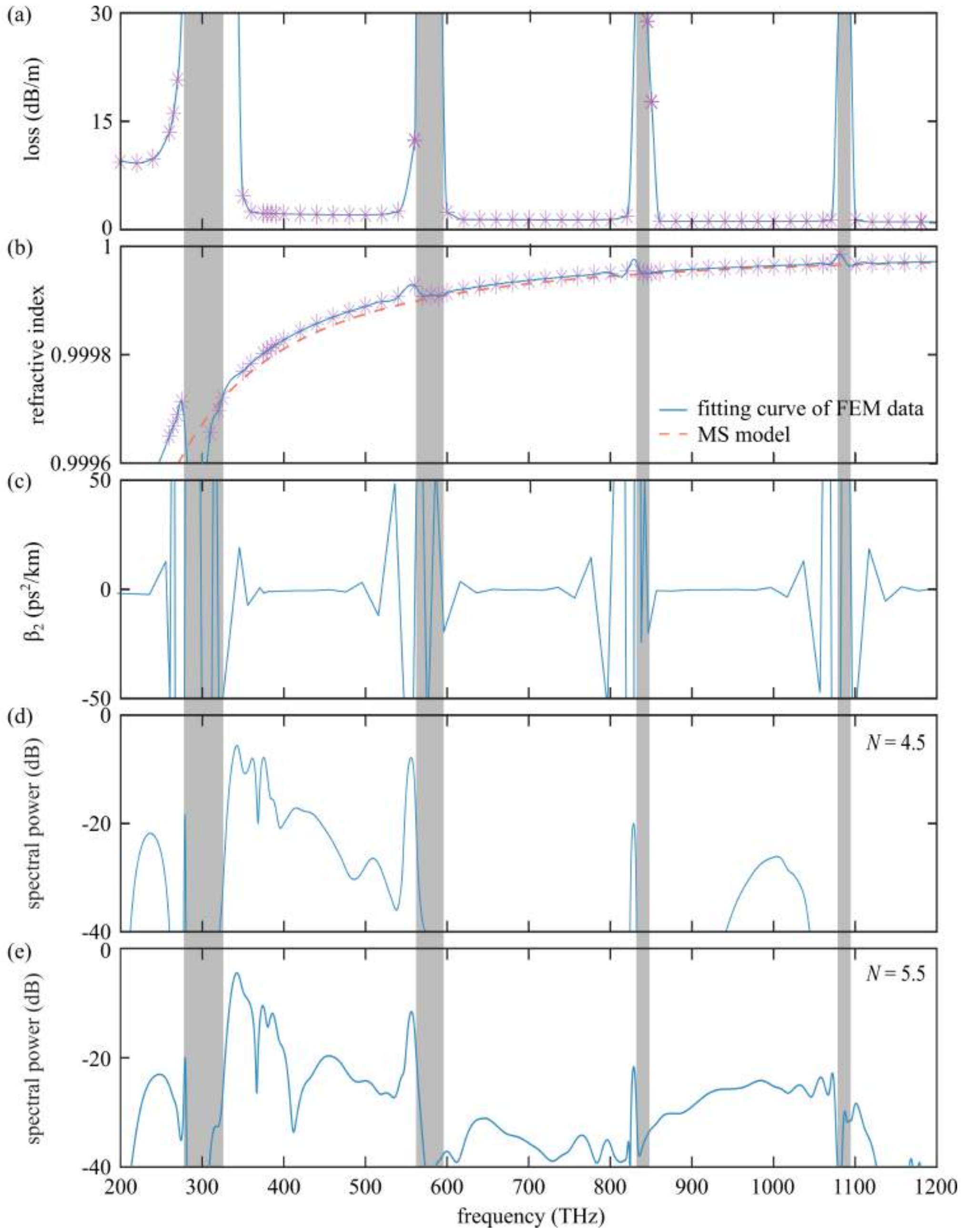

Figure 5.15: In the AR-HCF with a core of 29 μm diameter and cladding thickness of 500 nm, (a) the loss data calculated by FEM and its fitting result; (b) the refractive index data calculated by FEM and its fitting result (blue solid line), and calculated by the MS model (red dash line); (c) the second-order-dispersion calculated from the fitted refractive index result; (d) the output spectrum when the soliton number is 4.5 and (e) 5.5. The gray shades represent the resonant bands.

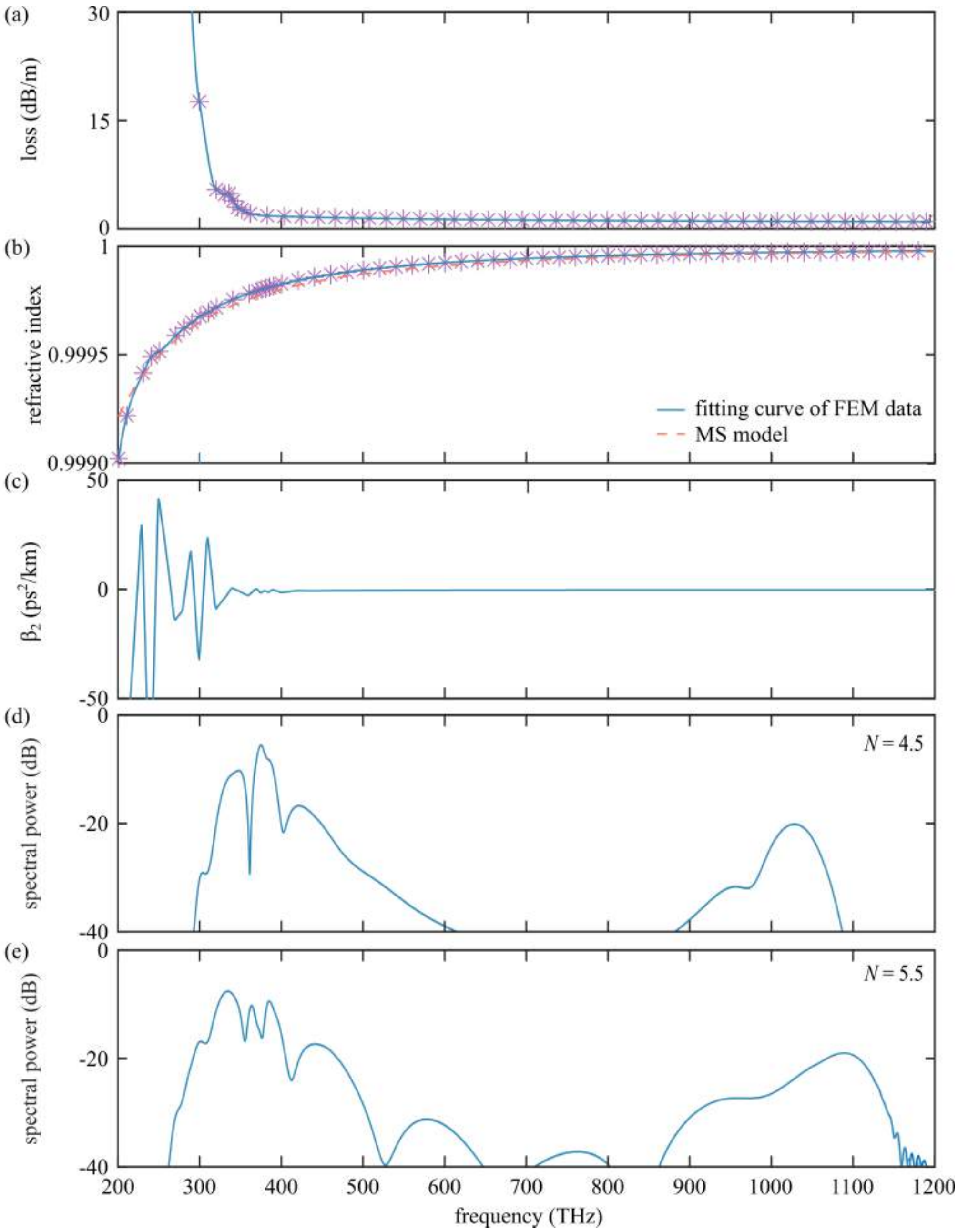

FIGURE 5.16: In the AR-HCF with a core of 29 μm diameter and cladding thickness of 74 nm, (a) the loss data calculated by FEM and its fitting result; (b) the refractive index data calculated by FEM and its fitting result (blue solid line), and calculated by the MS model (red dash line); (c) the second-order-dispersion calculated from the fitted refractive index result; (d) the output spectrum when the soliton number is 4.5 and (e) 5.5.

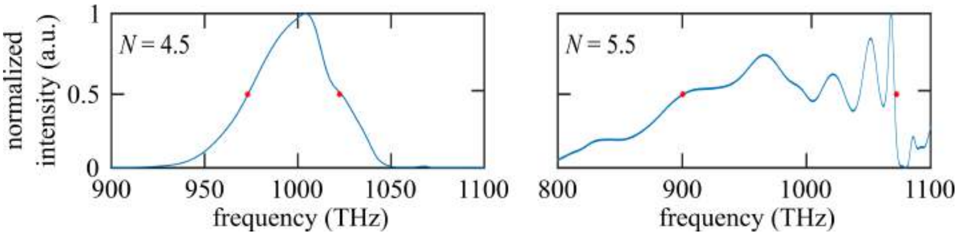

FIGURE 5.17: The magnified UV regions at the output of the AR-HCFs with the cladding element wall thickness 500 nm in linear scale with the red markers indicating the half-maximum positions of the spectral peak when the soliton number is 4.5 (left) and 5.5 (right).

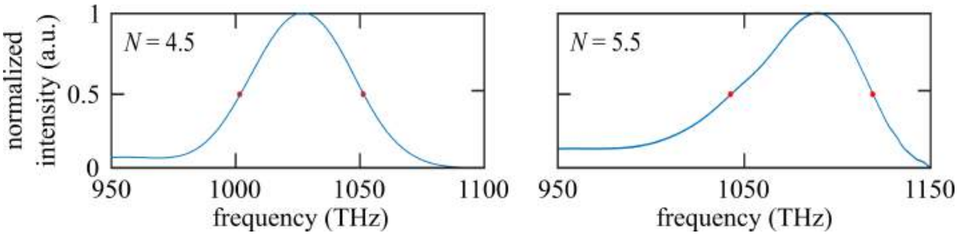

FIGURE 5.18: The magnified UV regions at the output of the AR-HCFs with the cladding element wall thickness 74 nm in linear scale with the red markers indicating the half-maximum positions of the spectral peak when the soliton number is 4.5 (left) and 5.5 (right).

The oscillation in the second-order-dispersion caused in the resonance bands by this fluctuation in refractive index is clearly illustrated in Fig.5.15 (c). With these oscillation, the phase matching condition can be satisfied, causing extra frequency-conversion point, which has been discussed in detail in Section 3.4.2. The spectra when the soliton number N is 4.5 and 5.5 at the output for both 500 nm and 74 nm are plotted in Figs. 5.15 (d)(e) and 5.16 (d)(e), respectively.

In the system free from the influence of resonances, the generated dispersive wave clearly blue-shifts from 1027 THz to 1093 THz when the soliton number is increased. This is accompanied by a rise in the conversion efficiency from 4.5% to 9.4 % and widening the UV spectrum from 48 to 74 THz at the full-width at half-maximum (FWHM). This is because the main spectrum becomes broader when N is higher, which leads to a wide range in the UV region where phase-matching is achieved. On the contrary, the resonances in the vicinity of the UV phase-matching point bring the center wavelength of the UV closer to the pump and reduce the conversion to 1.1%. A clean single-peak UV spectral band is still maintained in the case without the resonance in the neighborhood. For the AR-HCF with the wall thickness 500 nm, part of the blue-shifted UV spectral band goes into the

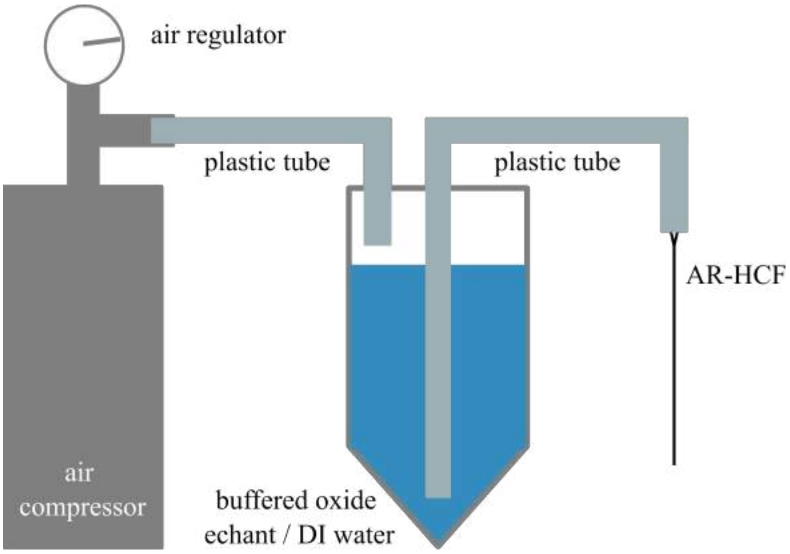

FIGURE 5.19: The setup for etching the AR-HCF.

high-loss region in the fourth resonant band. In fact, the spectral profile of the dispersive wave is relatively poor with the large intensity oscillations appearing in the band. This is due to the rapid variation in the edges of the transmission band that gives rise to a large set of phase-matched frequency conversions from the wide pump spectrum. It shows that the resonance not only deteriorates the efficiency of the UV conversion, but also impacts largely the quality of the spectral shape. One way to mitigate this issue is to use a thin cladding wall AR-HCF to push out the resonant bands to where they cannot affect the frequency conversion process. While tapering can achieve this to some extent, it is also shrink the core size simultaneously which is not desirable in many applications. Another way to reduce the wall thickness is wet etching.

5.2.3 Wet Etching Antiresonant HCF

Hydrofluoric acid solution has been used to chemical etch solid-core fiber to produce nanowires [112], form special structure like fiber Bragg gratings (FBG) [113], change the fiber end surface [114] and so on, mainly in sensing applications. Recently, etching hollow-core microstructure fibers are also reported [115] [116] for UV transmission enhancement. With this technique, the blue-shift of the resonance bands can be achieved, as the thickness of the silica core-surround is reduced, giving us the opportunity to investigate how the resonance bands effect the UV generation.

The experiment setup of wet etching is illustrated in Fig. 5.19. The buffered oxide etchant (BOE) is pushed to flow through the AR-HCF by the pressurized air from the air compressor. By tuning the air regulator, we can change the pressure of the compressed air in the etching container, which can further speed up or slow down the flow rate of BOE inside the AR-HCF. The flow rate plays an important role on the etching performance - if the HF is exhausted before it reaches the output of etched fiber, which happens when the flow rate is too slow, the nonnegligible nonuniformity of the cladding wall thickness along the fiber will be observed. To keep the variation of the thickness reduction small enough, the flow rate should be much faster than the decaying time of the HF concentration. However, if the flow rate is too fast, faster than the corrosion rate, it will require more solution and longer etching time to achieve the same corrosion thickness. Moreover, utilizing the buffered HF solution instead of directly using the hydrofluoric acid (HF) to etch the AR-HCF can further improve the uniformity of etching performance. This buffered HF can compensate the use of active etching components by the buffering reaction in the etching process [117].

$$\mathrm{NH_4F} + \mathrm{H_2O} \rightarrow \mathrm{NH_3} \cdot \mathrm{H_2O} + \mathrm{HF} \tag{5.3}$$

In this way, the decaying time of HF concentration in this solution can be extended to achieve more uniform corrosion performance along the AR-HCF. Generally speaking, the longer the fiber, the less consistent the etching performance is. In many experiments with AR-HCF, a long enough fiber length is an important factor in accumulating sufficient nonlinearity to observer the light-matter interaction phenomena. A longer uniformly etched AR-HCF can be obtained by having HF etch the first half the time in one direction and the rest of the time in the opposite direction. In order for the uniform thickness reduction throughout the fiber in the case of reverse etching direction, a low concentration of HF acid solution is required [118]. Besides, such low HF concentration makes the etched silica surface smoother, reducing the scatter loss which is particularly crucial in the UV band [115]. Moreover, the purity of the glass is an important factor on surface roughness especially for deep etching. As reported in [119], the surface roughness of etched fused silica with high purity is nearly unchanged with deeper and deeper etching while that of the D-263 substrate with 35% of impurity increased a lot.

After etching, the BOE is replaced by deionized (DI) water to clean the remained BOE solution inside the etched AR-HCF. Then, utilize the compressed air to blow dry the etched fiber, followed by heating up to 90 °C in a drying oven. Note that the fiber should be dry enough to form an undistorted fundamental mode.

In our etching experiment, a commercial BOE with volume rate of 10:1 is diluted with DI water in our experiments. The HF concentration of the etchant in the wet etching experiment is 0.02% in weight. This low concentration reduces its etching rate, making the uniformity is easier to be achieved, also results in a smoother etching surface.

Figure. 5.20 shows the transmission spectra of the original AR-HCF with the core-wall thickness of 470 nm, core diameter of 29 μm and the etched ones with or without pre-processing of sealing rings and different etching hours.

The transmission spectra of the AR-HCF without and with pre-sealing rings after 36 hr etching are shown in Fig. 5.20 (b) and (c) respectively. There are two resonance bands found in Fig. 5.20 (b), one is at 470 nm while another one is at 330 nm, which do not meet the relationship of the first and second resonance bands. I believe this is because during the etching process, there are two thicknesses formed, one is 220 nm and another one is 150 nm, due to the different etching process inside the different cladding rings. It is difficult to control the flow speed and duration of the BOE solution inside the cladding rings - with a diameter usually of a few micrometers - to be the same as a core with a diameter of dozens of microns for each etching. To get a reproducible and constant etching performance, the pre-processing of collapse rings is necessary. To close the cladding rings, one can use the arc or other splice methods to slightly heat the fiber end, or can use the UV glue to seal the rings surface. The sealing effect of these two methods are shown in Fig. 5.21. After sealing the rings (using the arc heating method), the transmission spectrum of the AR-HCF etched for the same time, 36 hr, is shown in Fig. 5.20 (c). There are two resonance bands observed, at 620 nm and 320 nm, corresponding to one thickness, 295 nm, which is thicker than that without sealing the ring. This also proves that even if the size of the ring is small, there will be BOE solution in it for etching. The etching rate is 4.8 nm/hr. Then, in Fig. 5.20 (d) shows the transmission spectrum after etching 54 hr with the pre-sealing process. The first resonance band is further blue-shifted to 470 nm, while the second band is out of our input supercontinuum source. From the transmission spectrum, the thicknesss

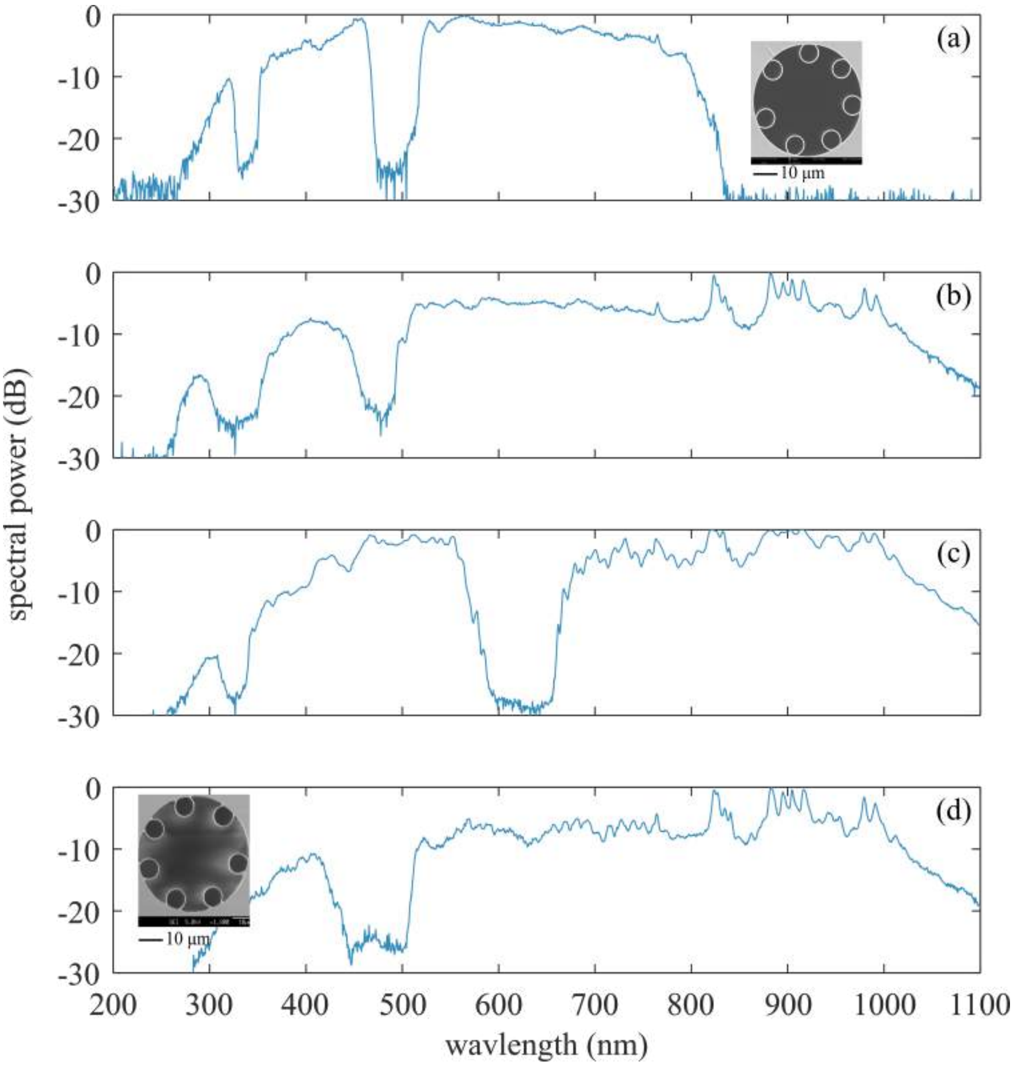

FIGURE 5.20: The transmission spectrum of (a) the original AR-HCF with a core diameter of 29 μm and core-wall thickness of 470 nm (b) after etching 36 hr without pre-processing of collapse rings (b) after etching 36 hr with pre-processing of collapse rings (d) after etching 54 hr with pre-processing of collapse rings. The inset panels are the SEM of the fibers before and after etching.

after etching 54 hr is 220 nm, corresponding to a etch rate of 4.6 nm/hr. This result is similar to the etching-36 hr result, which is an evidence that the corrosion process is controllable and predictable after sealing the rings since there will be only BOE solution in the fiber core for etching.

As shown in the scanning electronic micrograph, left of Fig. 5.21 (b), there is an additional outer jacket of this AR-HCF, making this fiber is not suitable for arc heating method to seal the rings, which would be heavily distorted under heat. The UV glue sealing method is utilized in this AR-HCF with a core diameter of 20 μm. Its original transmission spectrum is illustrated in Fig. 5.22 (a), showing

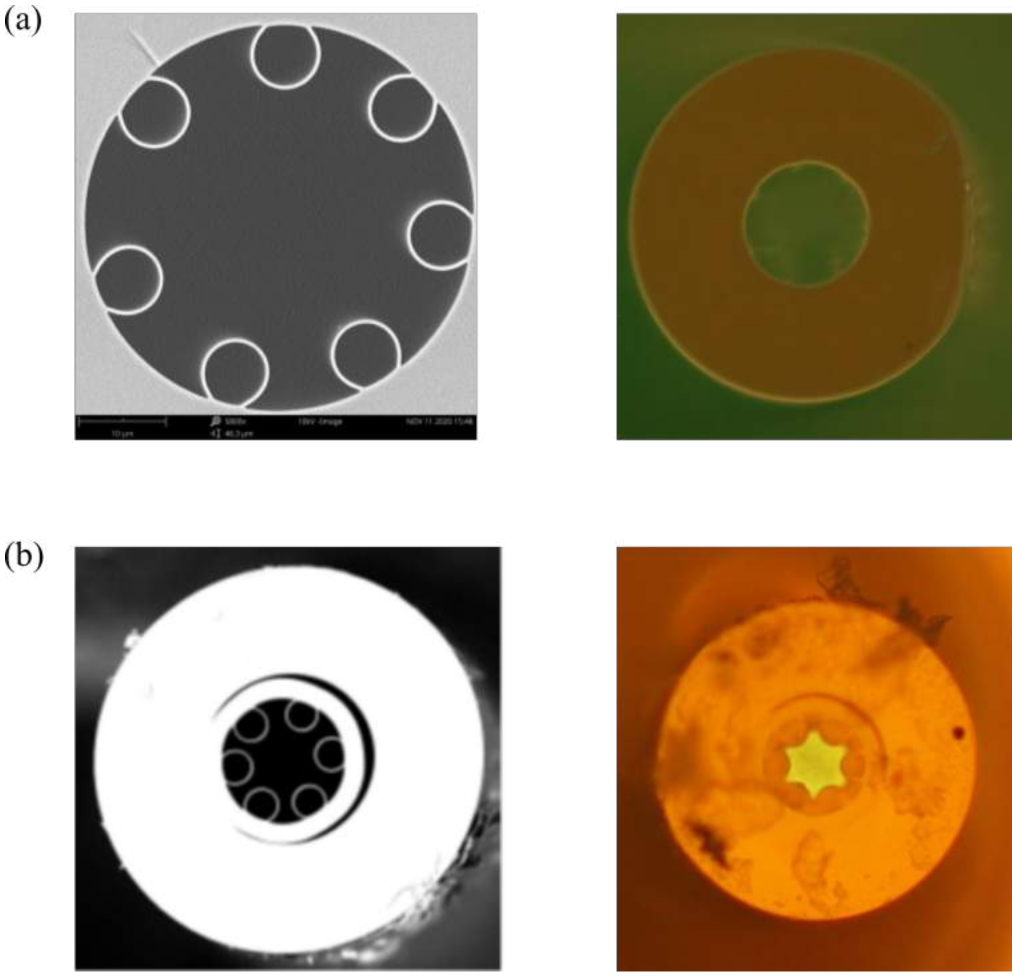

FIGURE 5.21: (a)Scanning electronic micrograph of the original AR-HCF (left) and microscopic photo after sealing the cladding rings by arc heat method (right). (b) Scanning electronic micrograph of the original AR-HCF (left) and microscopic photo after sealing the cladding rings by using UV glue (right).

the first and second resonance bands at 650 nm and 340 nm, corresponding to a core-wall thickness of 310 nm. After etching for 24 hr, its first resonance band is moved to 420 nm, which means the thickness is reduced to 200 nm. The thickness reduction here is 110 nm, and etch rate is 4.6 nm/hr, which is consistent with the result in the fiber with a core diameter of 29 μm.

5.2.4 UV Generation in Etched Antiresonant HCF

As shown in the Fig. 5.20 (a), the first resonance band of the AR-HCF is close to the pump, 800 nm, which would bring the drastic change in both loss and dispersion significant when pulse undergoes initial self-phase modulation. In the processing

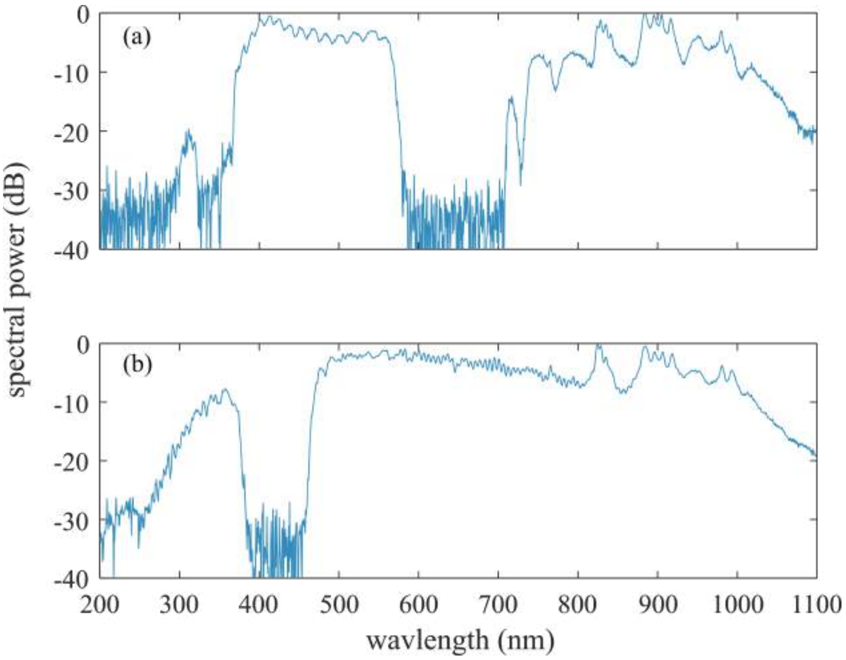

Figure 5.22: The transmission spectrum of (a) the original AR-HCF with a core diameter of 20 μm and core-wall thickness of 310 nm (b) after etching 24 hr with pre-processing of collapse rings by utilizing UV glue.

of pulse broadening in spectral domain and UV generation (Fig. 5.13), the pump goes through two resonance bands, which will cause energy loss and emit band-edge DWs. Moreover, there is one more band-edge DW generated on the blue side of the Marcatili DW that further drags the energy away from the pump. By utilizing the wet etching technique, we can achieve 250 nm reduction in core-wall thickness. Its transmission is shown in Fig. 5.20 (d). Not only does this keep the resonance band away from the pump, allowing the pump to spectral broaden enough, it also let the pump only needs to go through one resonance band when frequency up-conversion happens. The experiment of generating UV in this etched fiber with a core-wall thickness of 220 nm is shown in Fig. 5.23. The argon is filled 6 bar to produce Marcatili DW in the same location as previously produced in unetched fiber. The reason why it is different from the 9 bar of the previously nonetched fiber is that the resonance Band is removed away from pump in close proximity, which causing the dispersion of the pump change to reflect the phase matching conditions. The pump energy is increasing from top to bottom in Fig. 5.23.

In contrast to Fig. 5.13, there is only one band-edge DW generated at 480 nm, as expected at the red-side of the first resonance band. Overall, even though the energy inside the etched AR-HCF (obtained from the output energy) is higher than

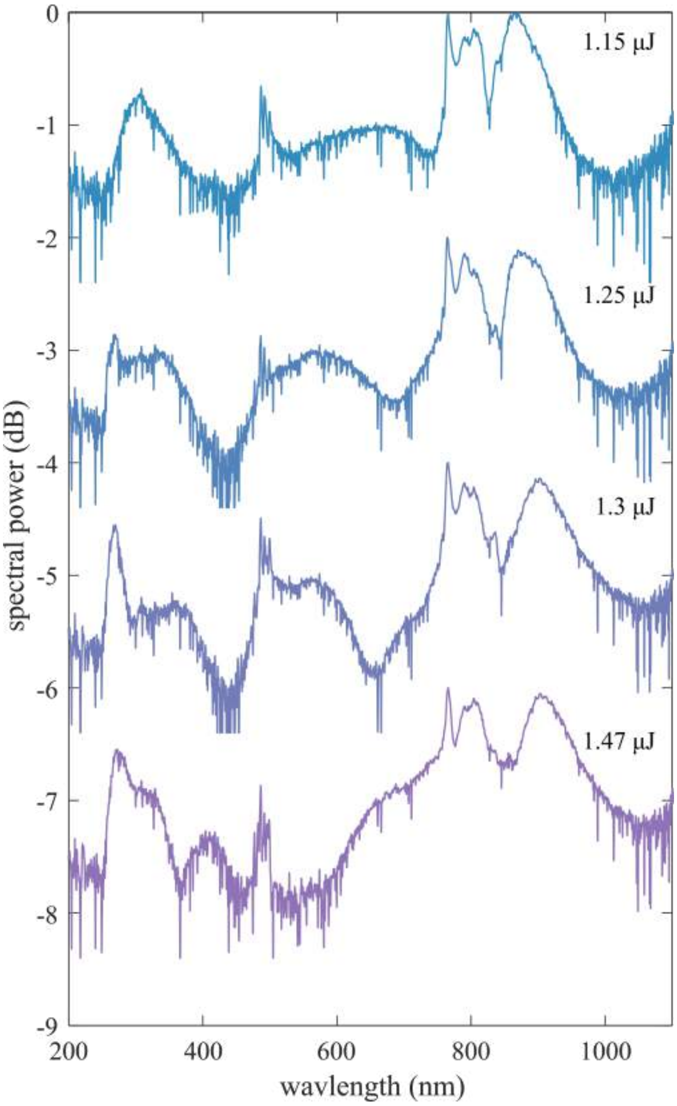

FIGURE 5.23: The output spectra of the AR-HCF with a core diameter of 29 μm after etching 54 hr with pre-processing of collapse rings, corresponding to the thickness of 220 nm. The filling gas is argon and pressure is 6 bar. Labeled next to each spectrum are the output energies, which increase from top to bottom.

that without etching, the spectral shape of Marcatili DW is better. Moreover, the conversion efficiency, defined as the ratio of Marcatili DW energy to the entire output spectrum, has increased to 10%.

The DW generation is repeated in another AR-HCF both before and after etching. The transmission spectrum after etching 24 hr is shown in Fig. 5.22. This AR-HCF is with a core diameter of 20 μm, and with a thickness reduced from 310 nm to 200 nm. Figure. 5.24 shows the spectra at the output of the AR-HCF. Both AR-HCFs are filled with 14 bar argon. Since the pump is fairly away from the resonance band, its dispersion is not effected, allowing the same phase-matching

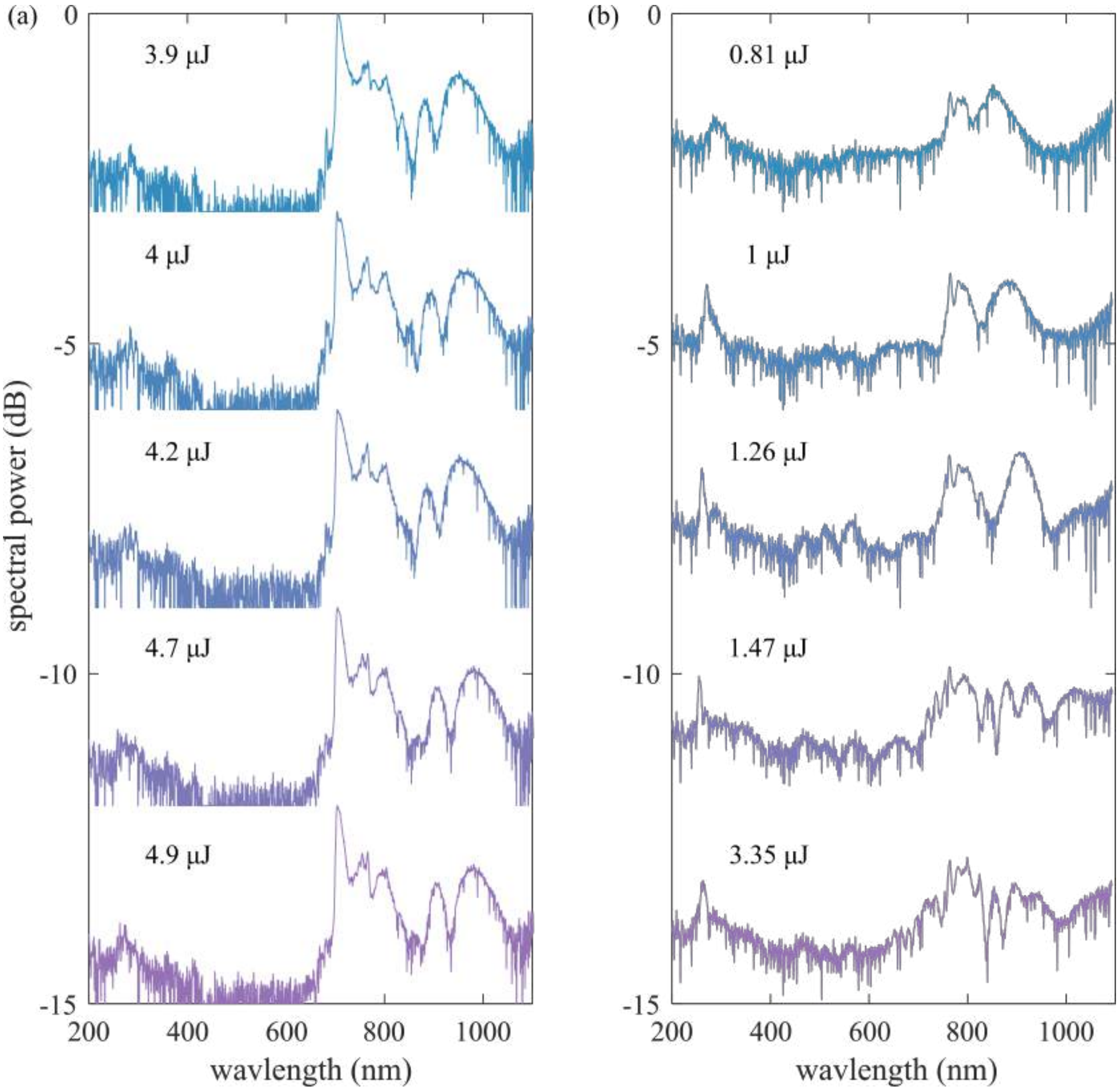

Figure 5.24: The output spectra of the 9 cm-long AR-HCF with a core diameter of 29 μm (a) before etching (core-wall thickness is 310 nm) and (b) after etching 24 hr with pre-processing of collapse rings (core-wall thickness is 200 nm). The labeled energies next to each spectrum are the launching energy into the gas chamber. The argon is filled 14 bar.

conditions. The energies labeled next to each spectrum are the launching energies, not the ones coupled into fibers. We learned that the photonionization happen of the focused beam when the launching energy is about 3 μJ from Fig. 5.13, causing the coupling efficiency drop dramatically. The same thing happens in the UV generation experiment in the non-etched fiber. Its short length (9 cm) and high loss of two resonance bands experienced when the spectrum is broadened, increased the pump energy threshold for UV emission, which makes the ionization issue important, also makes the soliton order larger. From the Fig. 5.24, it requires 3.9 μJ energy launching, which already exceeds the photonionization threshold of its focused beam. The emitted UV is still weak even with a fairly high launching energy. The conversion efficiency of these five experiments is only around 1%.

In contrary, the output spectra of the DW generation in the etched AR-HCF with a core diameter of 20 μm and thickness of 200 nm are shown in Fig. 5.24 (b). The resonance band is moved away from the broadened main spectrum. As shown in Fig. 5.22, the first resonance band is located at 400 - 450 nm. This thickness reduction reduces the energy threshold required for UV generation by a significant amount. From the experiment result, the launching energy for UV first emission is only 0.81 μJ, while the conversion efficiency obtained from the spectrum is 10%.

5.3 Summary

This chapter focuses on how the self-steepening effect and resonance band in the AR-HCF affect the UV conversion efficiency in the gas-filled HCF system. For the self-steepening effect, the soliton dynamics under the nonlinear Schrödinger equation with different normalized self-steepening parameters are summarized, and the approximate expected value of the frequency conversion efficiency is given. The numerical results show that the self-steepening effect can be positive or negative for the UV conversion efficiency. For realization in the UV generation experiments, the pump pulse needs to be compressed to less than 20 fs to provide the optimal self-steepening effect, which allows the conversion efficiency of 14%.

Next, the effect of AR-HCF resonance band on UV is studied.It was proved experimentally the conversion efficiency can be enhanced by using wet-etched AR-HCF to reduce the core-wall thickness.This reduces the number of resonant bands between the pump and the generated UV, so that more energy can be provided for seeding into the higher frequency range. Moreover, the numerical results show that the quality of UV produced in the etched fiber can be better maintained at high pump energy compared with the non-etched fiber.

Chapter 6

Conclusions and Future Work

6.1 Conclusions

In this thesis, a detailed study on post-processing of the antiresonant hollow-core fibers via tapering and wet-etching methods and their applications in gas-filled hollow-core fiber system have been presented. There are three main research works: 1) the transition part of the tapered AR-HCF is utilized to realize an in-fiber bandpass filter by manipulating its transmission properties; 2) the waist part of the tapered AR-HCF can serve as a small-mode-area HCF for the onset of low pump-energy-threshold UV; the enhanced UV generation in the gas-filled wet-etched hollow-core fiber pumped with compressed pulses. The important results in both numerical simulation and experiments are described below.

Chapter 3 proposes a novel in-fiber bandpass filter by utilizing the linear guidance properties of the antiresonant HCF. This is realized by tapering the AR-HCF to half its original size. In the transition part of the tapered fiber, one end is its original size and the other one is half its original size. The blue side of the transmission range of this bandpass filter is filtered out by exploiting the dielectric wall thickness-induced loss bands that sweep across the entire short wavelength region as the thickness varies along the length, while the long-wavelength cut-off is determined by the change in the core diameter to wavelength ratio. This device not only preserves all the benefits of hollow-core guidance, also can be customized and integrated seamlessly into a whole hollow-core fiber system. Moreover, a practical application, a mid IR femtosecond pulse source, is demonstrated numerically. The mid-IR pulse is emitted through the frequency conversion process in the gas-filled AR-HCF, namely bandedge induced dispersive wave generation. After that, the in-fiber bandpass filter is placed just by tapering that piece of fiber to filter out all the undesirable spectral components.

Chapter 4 focuses on the nanojoule-level pump-energy-threshold UV generation in gas-filled AR-HCF. The power scaling capability of the gas-filled HCF system is demonstrated first. By confining the light into an AR-HCF with a larger or smaller core, the energy of the soliton dynamics can be scaled up or down respectively. This gives us the opportunity to realize a low pump-energy-threshold onset of UV. The waist part of the tapered AR-HCF is served as a small-mode-area HCF which is difficult to achieve through direct stack-and-draw method. It also reduces fiber length requirements along with low pumping energy requirements. This not only alleviates the problem of high attenuation per unit length of SMA-HCF, but also facilitates the construction of a compact system.

Chapter 5 further investigates how to improve the conversion efficiency of UV and its quality. Two factors are discussed, self-steepening effect and resonance bands of AR-HCF. A series of numerical results based on normalized nonlinear Schrödinger equation present that the power spectral density at the maximum pulse compression position is crucial for enhancing UV generation. The more energy at high-frequencies range after spectral broadening, the higher conversion efficiency to UV. Besides, there is an optimal value of self-steepening effect in improving the UV conversion effect. With the increment of self-steepening, the UV conversion efficiency first increases and then decreases. To exploit this in the practical gas-filled hollow-core fiber system, the pump pulse can be compressed to increase the self-steepening effect. As shown in the numerical results, the conversion efficiency can be scaled up from less than 1% to about 14%.

Another discussed in **Chapter 5** is the effect of resonant bands of AR-HCF on UV generation. The experimental UV generation in the vicinity of resonance bands illustrates that when the UV is emitted between two resonant bands, the bandedge induced DW is enhanced by the proximity of UV, and further drags away the energy from pump. Subsequently, a series of numerically UV generation results with no band between pump and UV shows that not only did the lack of band significantly improve conversion efficiency, but it also better maintains the generated UV quality when pump energy increases. To take advantage of this in the experimental UV generation. Wet-etching technique is exploited. A 250 nm reduction of core-wall thickness in the AR-HCF in the experiment shifts the band to the blue side and reduces the number of bands between the pump and UV, which enhances the UV conversion efficiency substantially. The conversion efficiency is improved from only 1% in original AR-HCF to 10% in the etched AR-HCF.

In conclusion, this thesis has comprehensively demonstrated utilizing post-processing methods of antiresonant hollow-core fiber to exploit its linear loss characteristics and improve its nonlinear UV generation in different applications, through both extensive simulations and experiments.

6.2 Future Work

The post-processing method of antiresonant hollow-core fiber mentioned in this thesis and its application laid a foundation for our future expansion work.

1. The low-energy-threshold onset of UV in Chapter 4 opens a promising avenue for a compact wavelength-tunable UV frequency comb source driven directly by a femtosecond oscillator operating at a multi-megahertz repetition rate. The common method developed in generating UV comb is high-harmonic generation in a carefully designed amplifying cavity, which requires a very intense laser pulse focused into gas, and increases the sensitivity and complexity of the system [120]. However, the UV generation, or even the vacuum UV generation in the tapered AR-HCF can decrease the energy threshold down to sub-micro joule level, which is already achieved in a modern oscillator [121]. This low energy-threshold combines with the high-power handling capacity of HCFs, makes it possible to up-scale the power by increasing the repetition rate of the pump. By doing so, the generated UV can be power scaled up easily to match the power requirement for different applications. The work in Chapter 3 can be extended to a compact robust tunable UV comb by combing the modern oscillator technology and UV generation in the SMA-HCF.

2. In Chapter 5, the enhancement of UV generation with compressed pump pulse is investigated in numerical simulation, which gives us the theoretical basis of realizing it experimentally. Compressing the pump pulses can be done through soliton-effect compression and post-compression [60]. The pulse compressed down

to few cycles even attosecond regime is reported [49], which satisfies the pulse width corresponding to the self-steepening range we want to explore. Implementing it experimentally gives us another chance to get a better understanding of the mechanism by which the conversion efficiency is first increased and then decreased.

3. The UV is generated in gas-filled hollow-core fiber because of the phase matching mechanism and its wavelength can be tuned by changing the phase-matched frequency, which can simply by adjusting the filling gas pressure. This allows us to generate a UV continuum via pressure gradient [122]. The difficulty of experimental implementation of this is that resonant bands that appear more and more frequently in the high-frequencies region will break the generated UV continuum and affect its energy and conversion efficiency. In Chapter 5, wet-etching method is exploited to clean the transmission band between pump and generated UV. When the thickness is decreased to 180 nm, it gives a clean band in deep UV region from 210 nm to 390 nm, nearly an octave, to generate UV continuum.

List of Author’s Patents and Publications

Patents

[1] Xu Wu, Daiqi Xiong, and Wonkeun Chang, ”A Hollow-Core In-Fiber Optical Filter”, *Singapore Provisional Patent No.: 10202105132S.*

Journal Articles

[1] Daiqi Xiong, Xu Wu, Muhammad Rosdi Abu Hassan, Trivikramarao Gavara, and Wonkeun Chang, ”In-line hollow-core fiber-optic bandpass filter,” Opt. Lett. 46, 5918-5921 (2021)

[2] Daiqi Xiong, Jiaqi Luo, Muhammad Rosdi Abu Hassan, Xu Wu, and Wonkeun Chang, ”Low-energy-threshold deep-ultraviolet generation in a small-mode-area hollow-core fiber,” Photon. Res. 9, 590-595 (2021)

Conference Proceedings

[1] Daiqi Xiong, Xu Wu, Muhammad Rosdi Abu Hassan, and Wonkeun Chang, ”An Antiresonant Hollow-Core Fiber In-Line Bandpass Optical Filter,”2021 IEEE Photonics Conference (IPC), 2021, pp. 1-2.

[2] Daiqi Xiong, Jiaqi Luo, Muhammad Rosdi Abu Hassan, and Wonkeun Chang, ”Low-Energy-Threshold Deep-Ultraviolet Generation in a Gas-Filled Single-Ring Hollow-Core Fiber,” Nonlinear Photonics, Optical Society of America, 2020, paper NpM2D.1.

Bibliography

[1] R. Cregan, B. Mangan, J. Knight, T. Birks, P. S. J. Russell, P. Roberts, and D. Allan, "Single-mode photonic band gap guidance of light in air," *science*, vol. 285, no. 5433, pp. 1537–1539, 1999. xv, 1, 7, 8, 9

[2] F. Benabid, J. C. Knight, G. Antonopoulos, and P. S. J. Russell, "Stimulated raman scattering in hydrogen-filled hollow-core photonic crystal fiber," *Science*, vol. 298, no. 5592, pp. 399–402, 2002. xv, 2, 9, 10

[3] Y. Wang, N. V. Wheeler, F. Couny, P. Roberts, and F. Benabid, "Low loss broadband transmission in hypocycloid-core kagome hollow-core photonic crystal fiber," *Optics letters*, vol. 36, no. 5, pp. 669–671, 2011. xv, 9, 10

[4] F. Yu, W. J. Wadsworth, and J. C. Knight, "Low loss silica hollow core fibers for 3–4 μm spectral region," *Optics express*, vol. 20, no. 10, pp. 11 153–11 158, 2012. xv, 1, 10

[5] A. N. Kolyadin, A. F. Kosolapov, A. D. Pryamikov, A. S. Biriukov, V. G. Plotnichenko, and E. M. Dianov, "Light transmission in negative curvature hollow core fiber in extremely high material loss region," *Optics express*, vol. 21, no. 8, pp. 9514–9519, 2013. xv, 1, 10, 30

[6] F. Poletti, "Nested antiresonant nodeless hollow core fiber," *Optics express*, vol. 22, no. 20, pp. 23 807–23 828, 2014. xv, 10

[7] G. T. Jasion, H. Sakr, J. R. Hayes, S. R. Sandoghchi, L. Hooper, E. N. Fokoua, A. Saljoghei, H. C. Mulvad, M. Alonso, A. Taranta *et al.*, "0.174 db/km hollow core double nested antiresonant nodeless fiber (dnanf)," in *2022 Optical Fiber Communications Conference and Exhibition (OFC)*. IEEE, 2022, pp. 1–3. xv, 2, 10, 22, 26

[8] N. Litchinitser, A. Abeeluck, C. Headley, and B. Eggleton, "Antiresonant reflecting photonic crystal optical waveguides," *Optics letters*, vol. 27, no. 18, pp. 1592–1594, 2002. xv, 11

[9] K. C. Kao and G. A. Hockham, "Dielectric-fibre surface waveguides for optical frequencies," in *Proceedings of the Institution of Electrical Engineers*, vol. 113, no. 7. IET, 1966, pp. 1151–1158. 1

[10] G. Keiser, *Optical fiber communications.* McGraw-Hill New York, 2000, vol. 2. 1

[11] E. Agrell, M. Karlsson, A. Chraplyvy, D. J. Richardson, P. M. Krummrich, P. Winzer, K. Roberts, J. K. Fischer, S. J. Savory, B. J. Eggleton *et al.*, "Roadmap of optical communications," *Journal of Optics*, vol. 18, no. 6, p. 063002, 2016. 1

[12] B. Culshaw, "Optical fiber sensor technologies: opportunities and-perhaps-pitfalls," *Journal of lightwave technology*, vol. 22, no. 1, p. 39, 2004. 1

[13] B. Culshaw and A. Kersey, "Fiber-optic sensing: A historical perspective," *Journal of lightwave technology*, vol. 26, no. 9, pp. 1064–1078, 2008. 1

[14] D. J. Richardson, J. Nilsson, and W. A. Clarkson, "High power fiber lasers: current status and future perspectives," *JOSA B*, vol. 27, no. 11, pp. B63–B92, 2010. 1

[15] Y. Tamura, H. Sakuma, K. Morita, M. Suzuki, Y. Yamamoto, K. Shimada, Y. Honma, K. Sohma, T. Fujii, and T. Hasegawa, "The first 0.14-db/km loss optical fiber and its impact on submarine transmission," *Journal of Lightwave Technology*, vol. 36, no. 1, pp. 44–49, 2018. 1

[16] P. Russell, "Photonic crystal fibers," *science*, vol. 299, no. 5605, pp. 358–362, 2003. 1, 8

[17] M. R. A. Hassan, F. Yu, W. J. Wadsworth, and J. C. Knight, "Cavity-based mid-ir fiber gas laser pumped by a diode laser," *Optica*, vol. 3, no. 3, pp. 218–221, 2016. 1

[18] S.-F. Gao, Y.-Y. Wang, W. Ding, and P. Wang, "Hollow-core negative-curvature fiber for uv guidance," *Optics letters*, vol. 43, no. 6, pp. 1347–1350, 2018. 1, 42

[19] F. Yu, M. Cann, A. Brunton, W. Wadsworth, and J. Knight, "Single-mode solarization-free hollow-core fiber for ultraviolet pulse delivery," *Optics express*, vol. 26, no. 8, pp. 10 879–10 887, 2018. 1, 30

[20] M. Michieletto, J. K. Lyngsø, C. Jakobsen, J. Lægsgaard, O. Bang, and T. T. Alkeskjold, "Hollow-core fibers for high power pulse delivery," *Optics express*, vol. 24, no. 7, pp. 7103–7119, 2016. 1

[21] X. Zhu, D. Wu, Y. Wang, F. Yu, Q. Li, Y. Qi, J. Knight, S. Chen, and L. Hu, "Delivery of cw laser power up to 300 watts at 1080 nm by an uncooled low-loss anti-resonant hollow-core fiber," *Optics Express*, vol. 29, no. 2, pp. 1492–1501, 2021. 1

[22] J. R. Hayes, S. R. Sandoghchi, T. D. Bradley, Z. Liu, R. Slavík, M. A. Gouveia, N. V. Wheeler, G. Jasion, Y. Chen, E. N. Fokoua *et al.*, "Antiresonant

hollow core fiber with an octave spanning bandwidth for short haul data communications," *Journal of Lightwave Technology*, vol. 35, no. 3, pp. 437–442, 2017. 1

[23] F. Poletti, N. Wheeler, M. Petrovich, N. Baddela, E. Numkam Fokoua, J. Hayes, D. Gray, Z. Li, R. Slavík, and D. Richardson, "Towards high-capacity fibre-optic communications at the speed of light in vacuum," *Nature Photonics*, vol. 7, no. 4, pp. 279–284, 2013. 1, 22

[24] B. Mangan, L. Farr, A. Langford, P. J. Roberts, D. P. Williams, F. Couny, M. Lawman, M. Mason, S. Coupland, R. Flea *et al.*, "Low loss (1.7 db/km) hollow core photonic bandgap fiber," in *Optical Fiber Communication Conference*. Optical Society of America, 2004, p. PD24. 2

[25] N. V. Wheeler, M. N. Petrovich, R. Slavik, N. Baddela, E. Numkam, J. R. Hayes, D. Gray, F. Poletti, and D. Richardson, "Wide-bandwidth, low-loss, 19-cell hollow core photonic band gap fiber and its potential for low latency data transmission," in *National Fiber Optic Engineers Conference*. Optica Publishing Group, 2012, pp. PDP5A–2. 2

[26] A. D. Pryamikov, A. S. Biriukov, A. F. Kosolapov, V. G. Plotnichenko, S. L. Semjonov, and E. M. Dianov, "Demonstration of a waveguide regime for a silica hollow-core microstructured optical fiber with a negative curvature of the core boundary in the spectral region¿ 3.5 μm," *Optics express*, vol. 19, no. 2, pp. 1441–1448, 2011. 2

[27] B. Debord, A. Amsanpally, M. Chafer, A. Baz, M. Maurel, J.-M. Blondy, E. Hugonnot, F. Scol, L. Vincetti, F. Gérôme *et al.*, "Ultralow transmission loss in inhibited-coupling guiding hollow fibers," *Optica*, vol. 4, no. 2, pp. 209–217, 2017. 2, 11

[28] J. Reintjes, *Nonlinear optical parametric processes in liquids and gases*. Elsevier, 2012. 2

[29] N. Bloembergen, "The influence of electron plasma formation on superbroadening in light filaments," *Optics Communications*, vol. 8, no. 4, pp. 285–288, 1973.

[30] E. Yablonovitch, "Self-phase modulation and short-pulse generation from laser-breakdown plasmas," *Physical review A*, vol. 10, no. 5, p. 1888, 1974. 2

[31] A. Abdolvand, A. Nazarkin, A. Chugreev, C. Kaminski, and P. S. J. Russell, "Solitary pulse generation by backward raman scattering in h 2-filled photonic crystal fibers," *Physical review letters*, vol. 103, no. 18, p. 183902, 2009. 3

[32] J. Nold, P. Hölzer, N. Joly, G. Wong, A. Nazarkin, A. Podlipensky, M. Scharrer, and P. S. J. Russell, "Pressure-controlled phase matching to third harmonic in ar-filled hollow-core photonic crystal fiber," *Optics letters*, vol. 35, no. 17, pp. 2922–2924, 2010. 3

[33] A. Nazarkin, A. Abdolvand, A. Chugreev, and P. S. J. Russell, "Direct observation of self-similarity in evolution of transient stimulated raman scattering in gas-filled photonic crystal fibers," *Physical review letters*, vol. 105, no. 17, p. 173902, 2010. 3

[34] C. G. Durfee, S. Backus, H. C. Kapteyn, and M. M. Murnane, "Intense 8-fs pulse generation in the deep ultraviolet," *Optics Letters*, vol. 24, no. 10, pp. 697–699, 1999. 3

[35] N. Y. Joly, J. Nold, W. Chang, P. Hölzer, A. Nazarkin, G. Wong, F. Biancalana, and P. S. J. Russell, "Bright spatially coherent wavelength-tunable deep-uv laser source using an ar-filled photonic crystal fiber," *Physical Review Letters*, vol. 106, no. 20, p. 203901, 2011. 39

[36] K. F. Mak, J. C. Travers, P. Hölzer, N. Y. Joly, and P. S. J. Russell, "Tunable vacuum-uv to visible ultrafast pulse source based on gas-filled kagome-pcf," *Optics express*, vol. 21, no. 9, pp. 10 942–10 953, 2013. 3

[37] S.-J. Im, A. Husakou, and J. Herrmann, "High-power soliton-induced supercontinuum generation and tunable sub-10-fs vuv pulses from kagome-lattice hc-pcfs," *Optics express*, vol. 18, no. 6, pp. 5367–5374, 2010. 3

[38] F. Belli, A. Abdolvand, W. Chang, J. C. Travers, and P. S. J. Russell, "Vacuum-ultraviolet to infrared supercontinuum in hydrogen-filled photonic crystal fiber," *Optica*, vol. 2, no. 4, pp. 292–300, 2015. 9

[39] A. Deng, T. Gavara, M. R. A. Hassan, Y. Jin, Q. J. Wang, and W. Chang, "Four-octave-spanning mid-infrared supercontinuum generation in a gas-filled hollow-core fiber," in *CLEO: Science and Innovations*. Optica Publishing Group, 2021, pp. STh5A–1. 3

[40] R. J. Jones, K. D. Moll, M. J. Thorpe, and J. Ye, "Phase-coherent frequency combs in the vacuum ultraviolet via high-harmonic generation inside a femtosecond enhancement cavity," *Physical Review Letters*, vol. 94, no. 19, p. 193201, 2005. 3

[41] E. A. Marcatili and R. Schmeltzer, "Hollow metallic and dielectric waveguides for long distance optical transmission and lasers," *Bell System Technical Journal*, vol. 43, no. 4, pp. 1783–1809, 1964. 7

[42] R. Miles, G. Laufer, and G. Bjorklund, "Coherent anti-stokes raman scattering in a hollow dielectric waveguide," *Applied Physics Letters*, vol. 30, no. 8, pp. 417–419, 1977. 7

[43] E. Ippen, "Low-power quasi-cw raman oscillator," *Applied Physics Letters*, vol. 16, no. 8, pp. 303–305, 1970. 7

[44] B. A. López-Zubieta, E. C. Jarque, Í. J. Sola, and J. San Roman, "Theoretical analysis of single-cycle self-compression of near infrared pulses using high-spatial modes in capillary fibers," *Optics express*, vol. 26, no. 5, pp. 6345–6350, 2018. 7

[45] ——, "Spatiotemporal-dressed optical solitons in hollow-core capillaries," *OSA Continuum*, vol. 1, no. 3, pp. 930–938, 2018. 7

[46] A. Voronin and A. Zheltikov, "Subcycle solitonic breathers," *Physical Review A*, vol. 90, no. 4, p. 043807, 2014. 7

[47] R.-R. Zhao, D. Wang, Y. Zhao, Y.-X. Leng, and R.-X. Li, "Self-compression of 1.8-μm pulses in gas-filled hollow-core fibers," *Chinese Physics B*, vol. 26, no. 10, p. 104206, 2017.

[48] C. Brahms, F. Belli, and J. C. Travers, "Infrared attosecond field transients and UV to IR few-femtosecond pulses generated by high-energy soliton self-compression," *Phys. Rev. Research*, vol. 2, p. 043037, Oct 2020. [Online]. Available: https://link.aps.org/doi/10.1103/PhysRevResearch.2.043037 7

[49] J. C. Travers, T. F. Grigorova, C. Brahms, and F. Belli, "High-energy pulse self-compression and ultraviolet generation through soliton dynamics in hollow capillary fibres," *Nature Photonics*, vol. 13, no. 8, pp. 547–554, 2019. 7, 9, 41, 63, 86

[50] C. Brahms, T. Grigorova, F. Belli, and J. C. Travers, "High-energy ultraviolet dispersive-wave emission in compact hollow capillary systems," *Optics letters*, vol. 44, no. 12, pp. 2990–2993, 2019. 7

[51] T. Birks, P. Roberts, P. S. J. Russell, D. Atkin, and T. Shepherd, "Full 2-d photonic bandgaps in silica/air structures," *Electronics letters*, vol. 31, no. 22, pp. 1941–1943, 1995. 8

[52] R. Kashyap, *Fiber bragg gratings.* Academic press, 2009. 8

[53] P. Roberts, F. Couny, H. Sabert, B. Mangan, D. Williams, L. Farr, M. Mason, A. Tomlinson, T. Birks, J. Knight *et al.*, "Ultimate low loss of hollow-core photonic crystal fibres," *Optics express*, vol. 13, no. 1, pp. 236–244, 2005. 8

[54] T. A. Birks, J. C. Knight, and P. S. J. Russell, "Endlessly single-mode photonic crystal fiber," *Optics letters*, vol. 22, no. 13, pp. 961–963, 1997.

[55] J. Knight, J. Arriaga, T. Birks, A. Ortigosa-Blanch, W. Wadsworth, and P. S. J. Russell, "Anomalous dispersion in photonic crystal fiber," *IEEE photonics technology letters*, vol. 12, no. 7, pp. 807–809, 2000. 8

[56] A. Ortigosa-Blanch, J. Knight, W. Wadsworth, J. Arriaga, B. Mangan, T. Birks, and P. S. J. Russell, "Highly birefringent photonic crystal fibers," *Optics letters*, vol. 25, no. 18, pp. 1325–1327, 2000. 8

[57] J. C. Travers, W. Chang, J. Nold, N. Y. Joly, and P. S. J. Russell, "Ultrafast nonlinear optics in gas-filled hollow-core photonic crystal fibers," *JOSA B*, vol. 28, no. 12, pp. A11–A26, 2011. 8, 41, 70

[58] M. Duguay, Y. Kokubun, T. L. Koch, and L. Pfeiffer, “Antiresonant reflecting optical waveguides in sio2-si multilayer structures,” *Applied Physics Letters*, vol. 49, no. 1, pp. 13–15, 1986. 9

[59] G. Pearce, G. Wiederhecker, C. G. Poulton, S. Burger, and P. S. J. Russell, “Models for guidance in kagome-structured hollow-core photonic crystal fibres,” *Optics express*, vol. 15, no. 20, pp. 12 680–12 685, 2007. 9

[60] K. Mak, J. Travers, N. Y. Joly, A. Abdolvand, and P. S. J. Russell, “Two techniques for temporal pulse compression in gas-filled hollow-core kagomé photonic crystal fiber,” *Optics letters*, vol. 38, no. 18, pp. 3592–3595, 2013. 9, 85

[61] G. T. Jasion, T. D. Bradley, K. Harrington, H. Sakr, Y. Chen, E. N. Fokoua, I. A. Davidson, A. Taranta, J. R. Hayes, D. J. Richardson *et al.*, “Hollow core nanf with 0.28 db/km attenuation in the c and l bands,” in *Optical Fiber Communication Conference*. Optical Society of America, 2020, pp. Th4B–4. 10

[62] J.-L. Archambault, R. J. Black, S. Lacroix, and J. Bures, “Loss calculations for antiresonant waveguides,” *Journal of Lightwave Technology*, vol. 11, no. 3, pp. 416–423, 1993. 11

[63] A. Deng and W. Chang, “Geometrical scaling of antiresonant hollow-core fibers for mid-infrared beam delivery,” *Crystals*, vol. 11, no. 4, p. 420, 2021. 12, 26

[64] M. Zeisberger and M. A. Schmidt, “Analytic model for the complex effective index of the leaky modes of tube-type anti-resonant hollow core fibers,” *Scientific reports*, vol. 7, no. 1, pp. 1–13, 2017. 12, 31

[65] L. Vincetti and L. Rosa, “A simple analytical model for confinement loss estimation in hollow-core tube lattice fibers,” *Optics Express*, vol. 27, no. 4, pp. 5230–5237, 2019. 12, 31

[66] N. N. Akhmediev, A. Ankiewicz *et al.*, *Nonlinear pulses and beams*. Springer, 1997. 12

[67] G. P. Agrawal, “Nonlinear fiber optics,” in *Nonlinear Science at the Dawn of the 21st Century*. Springer, 2000, pp. 195–211. 12, 13, 16, 20

[68] R. H. Stolen and C. Lin, “Self-phase-modulation in silica optical fibers,” *Physical Review A*, vol. 17, no. 4, p. 1448, 1978. 13

[69] A. Hasegawa and F. Tappert, “Transmission of stationary nonlinear optical pulses in dispersive dielectric fibers. i. anomalous dispersion,” *Applied Physics Letters*, vol. 23, no. 3, pp. 142–144, 1973. 14

[70] P. K. A. Wai, H. Chen, and Y. Lee, “Radiations by “solitons”at the zero group-dispersion wavelength of single-mode optical fibers,” *Physical Review A*, vol. 41, no. 1, p. 426, 1990. 18

[71] J. P. Gordon, “Dispersive perturbations of solitons of the nonlinear schrödinger equation,” *JOSA B*, vol. 9, no. 1, pp. 91–97, 1992.

[72] J. Elgin, “Perturbations of optical solitons,” *Physical Review A*, vol. 47, no. 5, p. 4331, 1993.

[73] V. Karpman, “Radiation by solitons due to higher-order dispersion,” *Physical Review E*, vol. 47, no. 3, p. 2073, 1993.

[74] Y. Kodama, M. Romagnoli, S. Wabnitz, and M. Midrio, “Role of third-order dispersion on soliton instabilities and interactions in optical fibers,” *Optics letters*, vol. 19, no. 3, pp. 165–167, 1994.

[75] D. Skryabin, F. Luan, J. Knight, and P. S. J. Russell, “Soliton self-frequency shift cancellation in photonic crystal fibers,” *Science*, vol. 301, no. 5640, pp. 1705–1708, 2003. 18

[76] N. Akhmediev and M. Karlsson, “Cherenkov radiation emitted by solitons in optical fibers,” *Physical Review A*, vol. 51, no. 3, p. 2602, 1995. 18

[77] M. Wollenhaupt, A. Assion, and T. Baumert, “Femtosecond laser pulses: linear properties, manipulation, generation and measurement,” *Springer Handbook of Lasers and Optics*, p. 937, 2007. 21

[78] W. Chang, A. Nazarkin, J. Travers, J. Nold, P. Hölzer, N. Joly, and P. S. J. Russell, “Influence of ionization on ultrafast gas-based nonlinear fiber optics,” *Optics express*, vol. 19, no. 21, pp. 21 018–21 027, 2011. 21, 69

[79] A. Börzsönyi, Z. Heiner, M. Kalashnikov, A. Kovács, and K. Osvay, “Dispersion measurement of inert gases and gas mixtures at 800 nm,” *Applied optics*, vol. 47, no. 27, pp. 4856–4863, 2008. 21, 48

[80] H. Lehmeier, W. Leupacher, and A. Penzkofer, “Nonresonant third order hyperpolarizability of rare gases and n2 determined by third harmonic generation,” *Optics communications*, vol. 56, no. 1, pp. 67–72, 1985. 21, 40

[81] M. V. Ammosov, N. B. Delone, and V. P. Krainov, “Tunnel ionization of complex atoms and atomic ions in electromagnetic field,” in *High intensity laser processes*, vol. 664. SPIE, 1986, pp. 138–141. 21

[82] W. Ding, Y.-Y. Wang, S.-F. Gao, M.-L. Wang, and P. Wang, “Recent progress in low-loss hollow-core anti-resonant fibers and their applications,” *IEEE Journal of Selected Topics in Quantum Electronics*, vol. 26, no. 4, pp. 1–12, 2019. 22

[83] C. Peucheret, B. Zsigri, T. P. Hansen, and P. Jeppesen, “10 gbit/s transmission over air-guiding photonic bandgap fibre at 1550 nm,” *Electronics Letters*, vol. 41, no. 1, pp. 27–29, 2005. 22

[84] R. Pennetta, M. T. Enders, M. H. Frosz, F. Tani, and P. S. J. Russell, "Fabrication and non-destructive characterization of tapered single-ring hollow-core photonic crystal fiber," *APL Photonics*, vol. 4, no. 5, p. 056105, 2019. 24, 26, 42

[85] J. Love, W. Henry, W. Stewart, R. Black, S. Lacroix, and F. Gonthier, "Tapered single-mode fibres and devices. part 1: Adiabaticity criteria," *IEE Proceedings J (Optoelectronics)*, vol. 138, no. 5, pp. 343–354, 1991. 24

[86] Z. Liu, B. Karanov, L. Galdino, J. R. Hayes, D. Lavery, K. Clark, K. Shi, D. J. Elson, B. C. Thomsen, M. N. Petrovich *et al.*, "Nonlinearity-free coherent transmission in hollow-core antiresonant fiber," *Journal of Lightwave Technology*, vol. 37, no. 3, pp. 909–916, 2019. 30

[87] R. Sollapur, D. Kartashov, M. Zürch, A. Hoffmann, T. Grigorova, G. Sauer, A. Hartung, A. Schwuchow, J. Bierlich, J. Kobelke *et al.*, "Resonance-enhanced multi-octave supercontinuum generation in antiresonant hollow-core fibers," *Light: Science & Applications*, vol. 6, no. 12, pp. e17 124–e17 124, 2017. 30

[88] F. Tani, F. Köttig, D. Novoa, R. Keding, and P. S. J. Russell, "Effect of anti-crossings with cladding resonances on ultrafast nonlinear dynamics in gas-filled photonic crystal fibers," *Photonics Research*, vol. 6, no. 2, pp. 84–88, 2018. 30, 49, 62

[89] T. Gavara, M. I. Hasan, M. R. A. Hassan, A. Deng, and W. Chang, "Band-edge mediated frequency down-conversion in a gas-filled anti-resonant hollow-core fiber," *Optics Letters*, vol. 45, no. 24, pp. 6815–6818, 2020. 30

[90] A. Deng, T. Gavara, M. R. A. Hassan, M. I. Hasan, and W. Chang, "Microjoule-level mid-infrared femtosecond pulse generation in hollow-core fibres," *arXiv preprint arXiv:2204.02665*, 2022. 30

[91] M. Bache, M. S. Habib, C. Markos, and J. Lægsgaard, "Poor-man's model of hollow-core anti-resonant fibers," *JOSA B*, vol. 36, no. 1, pp. 69–80, 2019. 31, 33

[92] G. Batignani, E. Pontecorvo, G. Giovannetti, C. Ferrante, G. Fumero, and T. Scopigno, "Electronic resonances in broadband stimulated raman spectroscopy," *Scientific reports*, vol. 6, no. 1, pp. 1–8, 2016. 39

[93] P. Herman, R. Marjoribanks, A. Oettl, K. Chen, I. Konovalov, and S. Ness, "Laser shaping of photonic materials: deep-ultraviolet and ultrafast lasers," *Applied Surface Science*, vol. 154, pp. 577–586, 2000.

[94] M. Garcia-Lechuga, O. Utéza, N. Sanner, and D. Grojo, "Evidencing the nonlinearity independence of resolution in femtosecond laser ablation," *Optics Letters*, vol. 45, no. 4, pp. 952–955, 2020. 39

[95] B. Willenberg, F. Brunner, C. R. Phillips, and U. Keller, "High-power picosecond deep-uv source via group velocity matched frequency conversion," *Optica*, vol. 7, no. 5, pp. 485–491, 2020. 39

[96] P. Trabs, F. Noack, A. S. Aleksandrovsky, A. I. Zaitsev, and V. Petrov, "Generation of coherent radiation in the vacuum ultraviolet using randomly quasi-phase-matched strontium tetraborate," *Optics Letters*, vol. 41, no. 3, pp. 618–621, 2016.

[97] C. Chen, G. Wang, X. Wang, and Z. Xu, "Deep-uv nonlinear optical crystal kbe2bo3f2—discovery, growth, optical properties and applications," *Applied Physics B*, vol. 97, no. 1, pp. 9–25, 2009. 39

[98] P. S. J. Russell, P. Hölzer, W. Chang, A. Abdolvand, and J. Travers, "Hollow-core photonic crystal fibres for gas-based nonlinear optics," *Nature Photonics*, vol. 8, no. 4, pp. 278–286, 2014. 40

[99] C. M. Heyl, H. Coudert-Alteirac, M. Miranda, M. Louisy, K. Kovács, V. Tosa, E. Balogh, K. Varjú, A. L'Huillier, A. Couairon *et al.*, "Scale-invariant nonlinear optics in gases," *Optica*, vol. 3, no. 1, pp. 75–81, 2016. 41

[100] P. Hosseini, A. Ermolov, F. Tani, D. Novoa, and P. S. J. Russell, "Uv soliton dynamics and raman-enhanced supercontinuum generation in photonic crystal fiber," *ACS Photonics*, vol. 5, no. 6, pp. 2426–2430, 2018. 41

[101] T. Südmeyer, S. Marchese, S. Hashimoto, C. Baer, G. Gingras, B. Witzel, and U. Keller, "Femtosecond laser oscillators for high-field science," *Nature photonics*, vol. 2, no. 10, pp. 599–604, 2008. 42

[102] G. Jasion, J. Shrimpton, Y. Chen, T. Bradley, D. Richardson, and F. Poletti, "Microstructure element method (msem): viscous flow model for the virtual draw of microstructured optical fibers," *Optics Express*, vol. 23, no. 1, pp. 312–329, 2015. 42

[103] P. Rugeland, C. Sterner, and W. Margulis, "Visible light guidance in silica capillaries by antiresonant reflection," *Optics Express*, vol. 21, no. 24, pp. 29 217–29 222, 2013. 43

[104] A. Deng, I. Hasan, Y. Wang, and W. Chang, "Analyzing mode index mismatch and field overlap for light guidance in negative-curvature fibers," *Optics Express*, vol. 28, no. 19, pp. 27 974–27 988, 2020. 43

[105] F. Yu and J. C. Knight, "Negative curvature hollow-core optical fiber," *IEEE J. Sel. Top. Quantum Electron*, vol. 22, no. 2, pp. 146–155, 2016. 44

[106] K. DeLong, R. Trebino, J. Hunter, and W. White, "Frequency-resolved optical gating with the use of second-harmonic generation," *JOSA B*, vol. 11, no. 11, pp. 2206–2215, 1994. 45

[107] J. M. Dudley and S. Coen, "Coherence properties of supercontinuum spectra generated in photonic crystal and tapered optical fibers," *Optics letters*, vol. 27, no. 13, pp. 1180–1182, 2002. 49

[108] S. Roy, S. K. Bhadra, and G. P. Agrawal, "Dispersive waves emitted by solitons perturbed by third-order dispersion inside optical fibers," *Physical Review A*, vol. 79, no. 2, p. 023824, 2009. 54, 61

[109] B. Kibler, J. Dudley, and S. Coen, "Supercontinuum generation and nonlinear pulse propagation in photonic crystal fiber: influence of the frequency-dependent effective mode area," *Applied Physics B*, vol. 81, no. 2, pp. 337–342, 2005. 61

[110] J. Luan, P. S. J. Russell, and D. Novoa, "High-quality 8-fold self-compression of ultrashort near-uv pulses in ar-filled ultrathin-walled photonic crystal fiber," *arXiv preprint arXiv:2205.15705*, 2022. 63

[111] M. F. Saleh, W. Chang, P. Hölzer, A. Nazarkin, J. C. Travers, N. Y. Joly, P. S. J. Russell, and F. Biancalana, "Theory of photoionization-induced blueshift of ultrashort solitons in gas-filled hollow-core photonic crystal fibers," *Physical Review Letters*, vol. 107, no. 20, p. 203902, 2011. 69

[112] H. J. Kbashi, "Fabrication of submicron-diameter and taper fibers using chemical etching," *Journal of Materials Science & Technology*, vol. 28, no. 4, pp. 308–312, 2012. 74

[113] B. Yun, N. Chen, and Y. Cui, "Highly sensitive liquid-level sensor based on etched fiber bragg grating," *IEEE photonics technology letters*, vol. 19, no. 21, pp. 1747–1749, 2007. 74

[114] P. Lambelet, A. Sayah, M. Pfeffer, C. Philipona, and F. Marquis-Weible, "Chemically etched fiber tips for near-field optical microscopy: a process for smoother tips," *Applied optics*, vol. 37, no. 31, pp. 7289–7292, 1998. 74

[115] Y. Wang, P. Light, and F. Benabid, "Core-surround shaping of hollow-core photonic crystal fiber via hf etching," *IEEE Photonics Technology Letters*, vol. 20, no. 12, pp. 1018–1020, 2008. 74, 75

[116] V. T. Hoang, G. Stepniewski, R. Kasztelanic, D. Pysz, K. X. Dinh, M. Klimczak, R. Buczyński *et al.*, "Enhancement of UV-visible transmission characteristics in wet-etched hollow core anti-resonant fibers," *Optics Express*, vol. 29, no. 12, pp. 18 243–18 262, 2021. 74

[117] H. Kikyuama, N. Miki, K. Saka, J. Takano, I. Kawanabe, M. Miyashita, and T. Ohmi, "Principles of wet chemical processing in ulsi microfabrication," *IEEE Transactions on Semiconductor Manufacturing*, vol. 4, no. 1, pp. 26–35, 1991. 75

[118] E. C. Group, “Boe premixed etchants, a complete range of useful thermal oxide etching rates,” *Technical Data: Boe Buffered Oxide Etchants, General Chemical*, pp. 1–8, 2000. 75

[119] H. Zhu, M. Holl, T. Ray, S. Bhushan, and D. R. Meldrum, “Characterization of deep wet etching of fused silica glass for single cell and optical sensor deposition,” *Journal of Micromechanics and Microengineering*, vol. 19, no. 6, p. 065013, 2009. 75

[120] C. Gohle, T. Udem, M. Herrmann, J. Rauschenberger, R. Holzwarth, H. A. Schuessler, F. Krausz, and T. W. Hänsch, “A frequency comb in the extreme ultraviolet,” *Nature*, vol. 436, no. 7048, pp. 234–237, 2005. 85

[121] W. Liu, R. Liao, J. Zhao, J. Cui, Y. Song, C. Wang, and M. Hu, “Femtosecond mamyshev oscillator with 10-mw-level peak power,” *Optica*, vol. 6, no. 2, pp. 194–197, 2019. 85

[122] W. Chang, P. Hölzer, J. C. Travers, J. Nold, N. Y. Joly, and P. S. J. Russell, “Uv continuum generation in ar-filled hollow-core pcf,” in *CLEO: Science and Innovations*. Optica Publishing Group, 2012, pp. JW4A–62. 86